CarbonTracker Documentation

CT2017 release

CarbonTracker Team

June 5, 2018

Contents

1 Introduction

The goal of the CarbonTracker program is to produce quantitative estimates of atmospheric carbon uptake and release for North America and the rest of the world that are consistent with observed patterns of CO_2 in the atmosphere.

1.1 A tool for science, and policy

CarbonTracker and the associated long-term monitoring of atmospheric CO_2 helps improve our understanding of how carbon uptake and release from land ecosystems and oceans are responding to a changing climate, increasing levels of atmospheric CO_2 (higher CO_2 may enhance plant growth) and other environmental changes, including human management of land and oceans. The open access to all CarbonTracker results means that anyone can scrutinize our work, suggest improvements, and profit from our efforts. This will accelerate the development of a tool that can monitor, diagnose, and possibly predict the behavior of the global carbon cycle, and the climate that is so intricately connected to it.

CarbonTracker can become a policy support tool too. Its ability to accurately quantify natural and anthropogenic emissions and uptake at regional scales is currently limited by a sparse observational network. With enough observations, it will become possible to keep track of regional emissions, including those from fossil fuel use, over long periods of time. This will provide an independent check on emissions accounting, estimates of fossil fuel use based on economic inventories. It can thus provide feedback to policies aimed at limiting greenhouse gas emissions. This independent measure of effectiveness of any policy, provided by the atmosphere itself (where CO_2 levels matter most), is the bottom line in any mitigation strategy.

1.2 A community effort

CarbonTracker is intended to be a tool for the community and we welcome feedback and collaboration from anyone interested. Our ability to accurately track carbon with more spatial and temporal detail is dependent on our collective ability to make enough measurements and to obtain enough air samples to characterize variability present in the atmosphere. For example, estimates suggest that observations from tall communication towers (taller than 200m) can tell us about carbon uptake and emission over a radius of only several hundred kilometers. The map of observation sites shows how sparse the current network is. One way to join this effort is by contributing measurements. Regular air samples collected from the surface, towers or aircraft are needed. It would also be very fruitful to expand use of continuous measurements like the ones now being made on very tall (more than 200m) communications towers. Another way to join this effort is by volunteering flux estimates from your own work, to be run through CarbonTracker and assessed against atmospheric CO_2. Please contact us if you would like to get involved and collaborate with us.

1.3 Updates

CarbonTracker is updated about once per year to include new data and model improvements. The updated calculations are produced for the year 2000 through the most recent complete year of observations. Previous versions are available at the CarbonTracker website, and the effect of significant changes to any of the system components is noted.

Important revisions of our methods for CT2017 include the following:

- Use of "adaptive" model-data mismatch scheme.
- Use of hourly data at continuous measurement sites.
- New land and wildfire priors

1.4 The role of other atmospheric species in constraining the atmospheric carbon budget

Many laboratories making high accuracy CO_2 observations also make many other measurements of the same air, typically other greenhouse gases such as methane CH_4, nitrous oxide N_2O, sulfur hexafluoride SF_6, as well as carbon monoxide (CO) and isotopic ratios of CO_2 and CH_4. These measurements are usually made as mole fractions, for reasons explained here.

These trace gases are relevant for climate change and interesting in their own right, but the additional measurements can also help in source identification or process understanding. For this reason a series of halocompounds and hydrocarbons have recently been added to the analysis of a subset of air samples. Several of these species can be useful for monitoring air quality, but they can also help with better source apportionment of the greenhouse gases. In addition, the estimation of the source strengths of a number of pollutants could be greatly improved if we were able to quantify fossil fuel CO_2 emissions from air measurements for specified regions.

The best tracer for quantifying the component of atmospheric CO_2 that has been recently added to an air mass through the burning of fossil fuels is the decrease of the carbon-14 content of CO_2. Cosmic rays produce carbon-14, a radioactive form of carbon, in the higher regions of the atmosphere. It is present in the atmosphere and oceans and in all living organisms and their remains, but coal, oil, and natural gas contain no carbon-14 because it has long decayed away. Currently, carbon-14 measurements are made on only a small subset of the air samples because of higher analysis costs. None of these other data and their relationships have been used in this release of CarbonTracker. We expect them to be incorporated gradually at later stages.

CarbonTracker is a NOAA contribution to the North American Carbon Program.

2 Terrestrial biosphere module

The biospheric component of the terrestrial carbon cycle consists of all the carbon stored in 'biomass' around us. This includes trees, shrubs, grasses, carbon within soils, dead wood, and leaf litter. Such reservoirs of carbon can exchange CO_2 with the atmosphere. Exchange starts when plants take up CO_2 during their growing season through the process called photosynthesis (uptake). Most of this carbon is released back to the atmosphere throughout the year through a process called respiration (release). This includes both the decay of dead wood and litter and the metabolic respiration of living plants. Of course, plants can also return carbon to the atmosphere when they burn, as described in Section 3. Even though the yearly sum of uptake and release of carbon amounts to a relatively small number (a few petagrams (one Pg=10^{15} g)) of carbon per year, the flow of carbon each way is as large as 120 PgC each year. This is why the net result of these flows needs to be monitored in a system such as ours. It is also the reason we need a good physical description (model) of these flows of carbon. After all, from the atmospheric measurements we can only see the small net sum of the large two-way streams (gross fluxes). Information on what the biospheric fluxes are doing in

each season, and in every location on Earth is derived from a specialized biosphere model, and fed into our system as a first guess, to be refined by our assimilation procedure.

2.1 CASA model

Two biosphere models currently provide first-guess terrestrial fluxes for CT2017. Both models are versions of the Carnegie-Ames Stanford Approach (CASA) biogeochemical model introduced by Potter *et al.*(1993). CASA calculates global carbon fluxes using input from weather models to drive biophysical processes, and satellite observed Normalized Difference Vegetation Index (NDVI) to track plant phenology. The models are driven by year-specific weather and satellite observations, and include the effects of fires on photosynthesis and respiration (see van der Werf *et al.*, 2006, and Giglio *et al.*, 2006). Both simulations provide $0.5^\circ \times 0.5^\circ$ global fluxes with a monthly time resolution.

CASA models provide monthly-mean Net Primary Production (NPP) and heteotrophic respiration (R_H) for each terrestrial grid cell being simulated. NPP is the difference in photosynthetic carbon uptake (Gross Primary Production, GPP) and the carbon release by the same plants due to "maintenance respiration", which is also called autotrophic respiration, R_A. The carbon uptake represented by NPP and carbon release represented by R_H can be differenced to provide Net Ecosystem Exchange (NEE) of CO_2. Throughout this discussion, we use the convention that fluxes carry algebraic signs and we adopt the "atmospheric perspective" for those signs. Thus carbon uptake by the terrestrial biosphere is a negative flux to the atmosphere, and release of CO_2 back to the atmosphere is a positive flux. This means that we represent all respiration fluxes as positive and GPP as negative, so NEE $=$ NPP $+ R_H$. This stands in contrast to convention in the terrestrial carbon community, where all fluxes are generally non-negative.

2.2 Temporal downscaling

Use of monthly-mean terrestrial fluxes to simulate atmospheric CO_2 is not sufficient to resolve the variability observed at measurement sites. Instead, higher-frequency variations, including the diurnal cycle and effects of passing weather systems must be imposed on the CASA monthly fluxes. Following the logic laid out by Olsen and Randerson (2004), we transform the CASA-supplied monthly-mean NPP and R_H fluxes into GPP and total ecosystem respiration, $R_E = R_A + R_H$.

To estimate sub-monthly variations, including diurnal and synoptic variability, the Olsen and Randerson

(2004) strategy is to model GPP as a linear function of incoming surface solar radiation and total ecosystem respiration as a function of near-surface temperature.

The fundamental assumption needed to apply this scheme is that we can resolve CASA-simulated NPP into GPP and R_A. We apply the assumption that GPP is twice NPP, which further implies that R_A is the same size as NPP (but of opposite sign):

$$\text{GPP} = 2 * \text{NPP}, \tag{1}$$

$$\text{NPP} = \text{GPP} + R_A, \tag{2}$$

and

$$R_A = -1 * \text{NPP}. \tag{3}$$

We use meteorological fields from the European Centre for Medium-Range Weather Forecasts (ECMWF) ERA-interim reanalysis to supply temperature and shortwave radiation. Fluxes are generated with 90-minute variability using a simple temperature Q_{10} relationship for respiration, assuming a global Q_{10} value of 1.5, and a linear scaling of photosynthesis with solar radiation. The procedure is very similar, but **NOT** identical to the procedure in Olsen and Randerson (2004). Note that the introduction of 90-minute variability conserves the monthly mean NEE from the CASA model. Instantaneous NEE for each 90-minute interval is created as:

$$\text{NEE}(t) = \text{GPP}(t) + R_E(t), \tag{4}$$

where

$$\text{GPP}(t) = \text{GPP}_{\text{mean}}(I(t)/I_{\text{mean}}) \tag{5}$$

$$R_E(t) = R_{E,\text{mean}}(Q_{10}(t)/Q_{10,\text{mean}}), \tag{6}$$

and Q_{10} is computed as

$$Q_{10}(t) = 1.5^{(T_{2m}(t)-273.15)/10.0}, \tag{7}$$

where T_{2m} is 2 meter temperature in Kelvin, I is surface solar radiation, t is time in 90-minute intervals, and x_{mean} represents the monthly mean of quantity x, including monthly-mean fluxes derived from the CASA model.

2.2.1 Smooth month-to-month variations

While the scheme outlined above imposes realistic diurnal- and synoptic-scale variations on monthly-mean GPP and R_E, it still allows for abrupt changes from one month to the next. For CT2017, we add a further processing step designed to remove such unrealistic step changes. We fit smooth curves to the monthly GPP and R_E using the piecewise integral quadratic splines (PIQS) of Rasmussen (1991). These PIQS fits are continuous in the first and second derivatives, and have the property of preserving monthly mean flux. We use a similar scheme to smooth over year-to-year step changes in fossil fuel emissions. The final smoothed GPP is

$$\text{GPP}_F(t) = \text{GPP}(t) - \text{GPP}_{\text{mean}} + \text{GPP}_{\text{PIQS}}(t), \tag{8}$$

and the final smoothed ecosystem respiration is

$$R_{E,F}(t) = R_E(t) - R_{E,\text{mean}} + R_{E,\text{PIQS}}(t). \tag{9}$$

Together, these form the terrestrial NEE imposed as a first-guess flux in CT2017:

$$\text{NEE}_F(t) = \text{GPP}_F(t) + R_{E,F}(t). \tag{10}$$

2.3 GFED4.1s and GFED_CMS

CarbonTracker uses fluxes from CASA runs from two models associated with the GFED project as its first guess for terrestrial biosphere fluxes. We have found a significantly better match to observations when using this output compared to the fluxes from a neutral biosphere simulation. Both of the CASA simulations used in CT2017 (GFED 4.1s and GFED_CMS) are driven by AVHRR NDVI. This satellite driver tends to

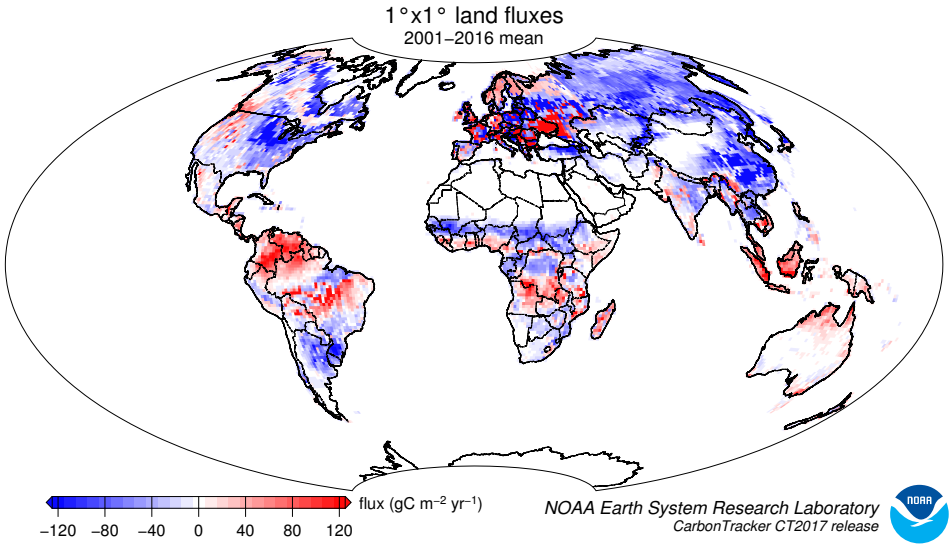

Figure 1: Map of optimized global biosphere fluxes. The pattern of net ecosystem exchange (NEE) of CO_2 of the land biosphere averaged over the time period indicated, as estimated by CarbonTracker. This NEE represents land-to-atmosphere carbon exchange from photosynthesis and respiration in terrestrial ecosystems, and a contribution from fires. It does not include fossil fuel emissions. Negative fluxes (blue colors) represent CO_2 uptake by the land biosphere, whereas positive fluxes (red colors) indicate regions in which the land biosphere is a net source of CO_2 to the atmosphere. Units are $\mathrm{gC\,m^{-2}\,yr^{-1}}$.

produce a larger-amplitude annual cycle of NEE compared to the alternative driver, MODIS fPAR. As one of the robust results of atmospheric invrsions is a deeper annual cycle of terrestrial NEE, inversions using NDVI-driven first-guess fluxes perform slightly better than those with a MODIS fPAR driver.

The record of atmospheric CO_2 calls for a deeper terrestrial biosphere sink than that generally simulated by forward models like CASA. This is manifested by a larger annual cycle of terrestrial biosphere fluxes, and in particular a deeper boreal summer uptake of carbon dioxide, in the posterior optimized fluxes compared to the prior models (See Fig. 2). We call upon the atmospheric CO_2 observations to make this change, and in order to handle these prior model differences the ensemble Kalman filter's prior covariance model has been re-tuned. In short, this prior uncertainty needs to comfortably span differences among the terrestrial biosphere priors, the fossil fuel emissions priors, and adjustments to fluxes required to bring model predictions into agreement with observations. As a result, the land biosphere prior uncertainty is larger in CT2017 in comparison to previous releases. Details can be found in Section 8.

CarbonTracker CT2017 is a full reanalysis of the 2000-2016 period using new fossil fuel emissions, CASA-GFED v4.1s and GFED_CMS fire emissions, and first-guess biosphere model fluxes derived from CASA-GFED v4.1s for 4 of our inversions, and from CASA GFED_CMS for the remaining 4 inversions.

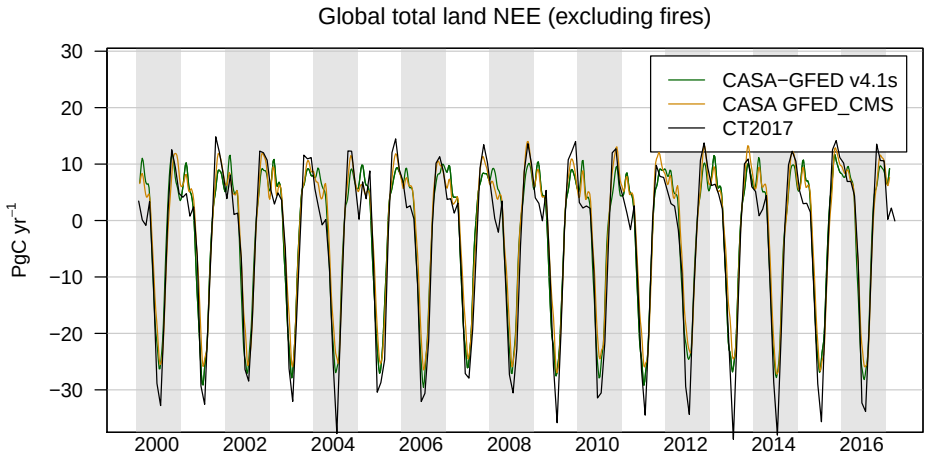

Figure 2: Time series of global-total terrestrial biosphere flux between the two priors and the CT2017 posterior. Global CO_2 uptake by the land biosphere, expressed in PgC yr^{-1}, excluding emissions by wildfire. Positive flux represents emission of CO_2 to the atmosphere, and the negative fluxes indicate times when the land biosphere is a sink of CO_2. Optimization against atmospheric CO_2 data requires a larger land sink than in either prior, which effectively requires a deeper annual cycle. This is shown by the CT2017 posterior (black).

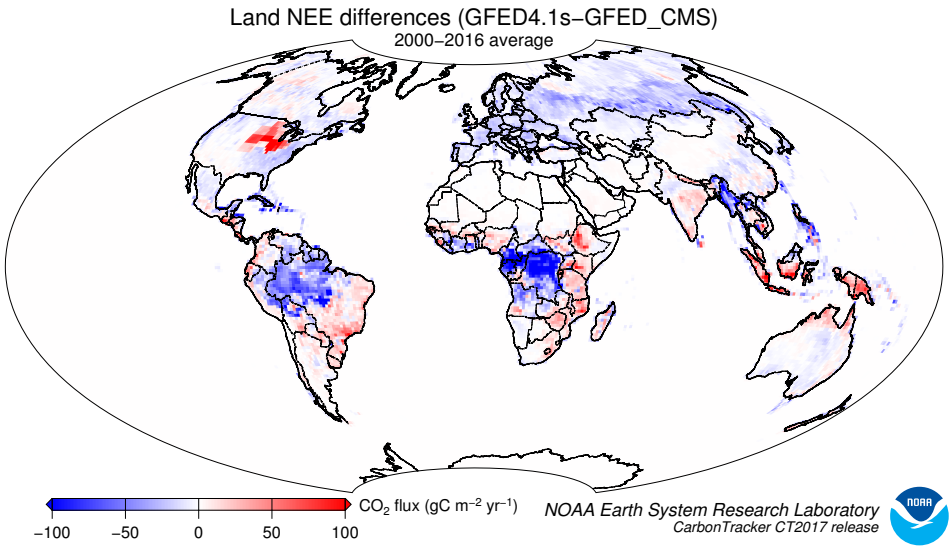

Figure 3: Differences in long-term mean terrestrial biosphere fluxes between the two priors. Red indicates areas where the GFED4.1s prior has less terrestrial uptake (or more outgassing to the atmosphere) than the GFED_CMS prior, and blue represents the opposite. Units are gC m^{-2} yr^{-1}.

Due to the inclusion of fires, inter-annual variability in weather and NDVI, the fluxes for North America start with a small net flux even when no assimilation is done. This first-guess flux ranges from neutral exchange to about 0.5 PgC yr^{-1} of uptake.

2.4 References

- Potter, C. S., J. T. Randerson, C. B. Field, P. A. Matson, P. M. Vitousek, H. A. Mooney, and S. A. Klooster (1993), Terrestrial ecosystem production: A process model based on global satellite and surface data, Global Biogeochem. Cycles, 7(4), 811841, doi:10.1029/93GB02725.
- van der Werf, G. R., Randerson, J. T., Collatz, G. J. and Giglio, L. (2003), Carbon emissions from fires in tropical and subtropical ecosystems. Global Change Biology, 9: 547562. doi:10.1046/j.1365-2486.2003.00604.x
- Jim Randerson research group
- Global Fire Emissions Database (GFED) web page
- Olsen, S. C., and J. T. Randerson (2004), Differences between surface and column atmospheric CO2 and implications for carbon cycle research, J. Geophys. Res., 109, D02301, doi:10.1029/2003JD003968.
- Giglio, L., van der Werf, G. R., Randerson, J. T., Collatz, G. J., and Kasibhatla, P.: Global estimation of burned area using MODIS active fire observations, Atmos. Chem. Phys., 6, 957-974, doi:10.5194/acp-6-957-2006, 2006.
- van der Werf, G. R., Randerson, J. T., Giglio, L., Collatz, G. J., Kasibhatla, P. S., and Arellano Jr., A. F.: Interannual variability in global biomass burning emissions from 1997 to 2004, Atmos. Chem. Phys., 6, 3423-3441, doi:10.5194/acp-6-3423-2006, 2006.
- L.A Rasmussen, Piecewise integral splines of low degree, Computers & Geosciences, Volume 17, Issue 9, 1991, Pages 1255-1263, ISSN 0098-3004, http://dx.doi.org/10.1016/0098-3004(91)90027-B.
- NASA GFED_CMS CASA project

3 Fire module

Vegetation fires are an important part of the carbon cycle and have been so for many millennia. Even before human civilization began to use fires to clear land for agricultural purposes, most ecosystems were subject to natural wildfires that would rejuvenate old forests and bring important minerals to the soils. When fires

consume part of the landscape in either controlled or natural burning, carbon dioxide (amongst many other gases and aerosols) is released in large quantities. Each year, vegetation fires emit around 2 PgC as CO_2 into the atmosphere, mostly in the tropics. Currently, a large fraction of wildfire is started by humans. This is mostly intentional to clear land for agriculture, or to re-fertilize soils before a new growing season. This important component of the carbon cycle is monitored mostly from space, while sophisticated 'biomass burning' models are used to estimate the amount of CO_2 emitted by each fire. Such estimates are then used in CarbonTracker to prescribe the emissions. These emissions are not modified in the optimization (inverse modeling) process.

In CT2017 we use two fire emissions datasets, each with at least daily temporal resolution. The GFED4.1s emissions are modeled at 3-hourly intervals, and GFED_CMS emissions are available at daily resolution.

3.1 Global Fire Emissions Database (GFED)

CT2017 uses GFED4.1s as one of the fire modules to estimate biomass burning. GFED4.1s is a variant of the CASA biogeochemical model as described in the terrestrial biosphere model documentation to estimate the carbon fuel in various biomass pools. The dataset consists of $1^\circ \times 1^\circ$ gridded monthly burned area, fuel loads, combustion completeness, and fire emissions (Carbon, CO_2, CO, CH_4, NMHC, H_2, NO_x, N_2O, PM2.5, Total Particulate Matter, Total Carbon, Organic Carbon, Black Carbon) for the time period spanning January 1997 - December 2016, of which we currently only use CO_2.

The GFED burned area is based on MODIS satellite observations of fire counts. These, together with detailed vegetation cover information and a set of vegetation specific scaling factors, allow predictions of burned area over the time span that active fire counts from MODIS are available. The relationship between fire counts and burned area is derived, for the specific vegetation types, from a 'calibration' subset of 500m resolution burned area from MODIS in the period 2001-2004.

Once burned area has been estimated globally, emissions of trace gases are calculated using the CASA biosphere model. The seasonally changing vegetation and soil biomass stocks in the CASA model are combusted based on the burned area estimate, and converted to atmospheric trace gases using estimates of fuel loads, combustion completeness, and burning efficiency.

For CT2017, we also apply temporal scaling factors updated from Mu *et al*. (2011) to downscale the GFED4.1s CO_2 emissions from monthly averages to emissions with 3-hourly resolution.

3.2 GFED_CMS: Fluxes from the NASA Carbon Monitoring System

The NASA GFED_CMS team uses a variant of the GFED4 system to produce alternative fire emissions. This model uses GIMSS NDVI, the GFEDv3 fire model and GFEDv4 burned area. Fire emissions are available on a daily basis from 2003-2015. For 2000-2002, we apply the climatology of GFED_CMS fire emissions, computed from its 2003-2015 mean.

Note that the GFED_CMS team produces temporally-downscaled GPP, heterotrophic respiration, and fires with 3-hourly resolution. This is done using MERRA meteorology using a scheme similar to Olsen and Randerson (2004). We do not use this downscaled product, in part because the MERRA meteorology is different from the ECMWF meteorology, and in part because the spatial resolution of the MERRA meteorology is different from our $1^\circ \times 1^\circ$ flux grid. This means that we are limited to daily resolution of GFED_CMS fire emissions: unlike the GFED4.1s fire emissions, these have no diurnal cycle.

3.3 References

- Giglio, L., J. T. Randerson, and G. R. van der Werf, (2013), Analysis of daily, monthly, and annual burned area using the fourth-generation global fire emissions database (GFED4) J. Geophys. Res. Biogeosci., 118, 317328, doi:10.1002/jgrg.20042.
- van der Werf, G. R., Randerson, J. T., Collatz, G. J. and Giglio, L. (2003), Carbon emissions from fires in tropical and subtropical ecosystems. Global Change Biology, 9: 547562. doi:10.1046/j.1365-2486.2003.00604.x
- van der Werf, G. R., Randerson, J. T., Giglio, L., Collatz, G. J., Mu, M., Kasibhatla, P. S., Morton, D. C., DeFries, R. S., Jin, Y., and van Leeuwen, T. T.: Global fire emissions and the contribution of deforestation, savanna, forest, agricultural, and peat fires (19972009), Atmos. Chem. Phys., 10, 11707-11735, doi:10.5194/acp-10-11707-2010, 2010.
- Akagi, S. K., Yokelson, R. J., Wiedinmyer, C., Alvarado, M. J., Reid, J. S., Karl, T., Crounse, J. D., and Wennberg, P. O.: Emission factors for open and domestic biomass burning for use in atmospheric models, Atmos. Chem. Phys., 11, 4039-4072, doi:10.5194/acp-11-4039-2011, 2011.
- Mu, M., Randerson, J. T., van der Werf, G. R., Giglio, L., Kasibhatla, P., Morton, D., Collatz G. J., DeFries, R. S., Hyer, E. J., Prins, E. M., Griffith, D. W. T., Wunch, D., Toon, G. C., Sherlock, V., and Wennberg, P. O. (2011), Daily and 3-hourly variability in global fire emissions and conse-

quences for atmospheric model predictions of carbon monoxide, J. Geophys. Res., 116, D24303, doi:10.1029/2011JD016245.

- Andreae, M. O., and P. Merlet (2001), Emission of trace gases and aerosols from biomass burning, Global Biogeochem. Cycles, 15(4), 955966, doi:10.1029/2000GB001382.
- Giglio, L., van der Werf, G. R., Randerson, J. T., Collatz, G. J., and Kasibhatla, P.: Global estimation of burned area using MODIS active fire observations, Atmos. Chem. Phys., 6, 957-974, doi:10.5194/acp-6-957-2006, 2006.
- van der Werf, G. R., Randerson, J. T., Giglio, L., Collatz, G. J., Kasibhatla, P. S., and Arellano Jr., A. F.: Interannual variability in global biomass burning emissions from 1997 to 2004, Atmos. Chem. Phys., 6, 3423-3441, doi:10.5194/acp-6-3423-2006, 2006.
- Jim Randerson research group
- Global Fire Emissions Database (GFED) web page
- GFED_CMS web page at NACP

4 Fossil fuel module

Human beings first influenced the carbon cycle through land-use change. Early humans used fire to control animals and later cleared forests for agriculture. Over the last two centuries, following the industrial and technical revolutions and continuing global population increase, fossil fuel combustion has become the largest anthropogenic source of CO_2. In 2013, fossil fuel combustion was responsible for nearly 10 billion metric tons of carbon emitted to the atmosphere. Coal, oil and natural gas combustion are the most common energy sources in both developed and developing countries. Important sectors of the economy–power generation, transportation, residential & commercial building heating, and industrial processes–rely on fossil fuel combustion. According to the Carbon Dioxide Information and Analysis Center (CDIAC), world emissions of CO_2 from fossil fuel burning, cement manufacturing, and flaring reached 9.8 PgC yr^{-1} (one PgC=10^{15} grams of carbon) in 2013 (Boden *et al*., 2016). Estimates extrapolated by the CarbonTracker team indicate that global total emissions remained nearly steady between 2013 and 2015.. Despite this apparent stabilization, 2014 & 2015 emissions are 59% larger than those in 1990. U.S. input of CO_2 to the atmosphere from fossil fuel burning in 2015 was 1.4 PgC, representing 14% of the global total. North American emissions have remained nearly constant since 2000, with a slight decrease in recent years. On the other hand, emis-

sions from developing economies such as the People's Republic of China have been increasing. Emissions from China in 2015 were 2.6 PgC yr^{-1}, representing 27% of the global total.

After the economic slowdown which affected many countries starting in 2008, fossil fuel emissions have rebounded, and in many parts of the world continue to increase. The U.S. Department of Energy's International Energy Outlook 2013 projects that the global total source will reach 12.4 PgC yr^{-1} in 2040. This may be an underestimate, however, as that same report projects 2020 emissions of 9.9 PgC yr^{-1}, a figure that was nearly reached in 2014.

In nearly all global and regional carbon flux estimation systems, including CarbonTracker, fossil fuel CO_2 emissions are not optimized. Instead, these emissions are imposed and are not subject to revision by the estimation framework. Global mass balance requires that any errors in fossil fuel emissions be compensated by opposing errors in land and ocean CO_2 exchange. Thus it is vital that fossil fuel CO_2 emissions are prescribed accurately, so that flux estimates for the land biosphere and oceans are robust. The fossil fuel emissions source data we use are available on an annually-integrated global and national basis. This aggregate information needs to be gridded before being incorporated into CarbonTracker. The major uncertainty in this process is distributing the national-annual emissions spatially across a nation and temporally into monthly contributions. In CT2017, two different fossil fuel CO_2 emissions datasets were used to help assess the uncertainty in this mapping process. These two emissions products are called the "Miller" and "ODIAC" emissions datasets. These two datasets have very similar global and national emissions for each year, but differ in how those emissions are distributed spatially and temporally.

Whereas previous CarbonTracker releases used monthly-constant fossil fuel emissions, in CT2015 we introduced the use of temporal scaling factors to simulate day-of-week and diurnal variability for those emissions. These "Temporal Improvements for Modeling Emissions by Scaling" (TIMES) scaling factors, introduced by Nassar *et al.* (2013), are again applied to both the Miller and ODIAC emissions modules for CT2017. The scaling factors consist of seven day-of-week global scaling factor maps, and 24 hourly global scaling factor maps to represent the diurnal cycle. For use in TM5, the hourly scaling factors were aggregated to three-hourly factors to accommodate the time step of the model.

4.1 The "Miller" emissions dataset

- **Global Totals** The Miller fossil fuel emission inventory is derived from independent global total and spatially-resolved inventories. Annual global total fossil fuel CO_2 emissions are from the Carbon

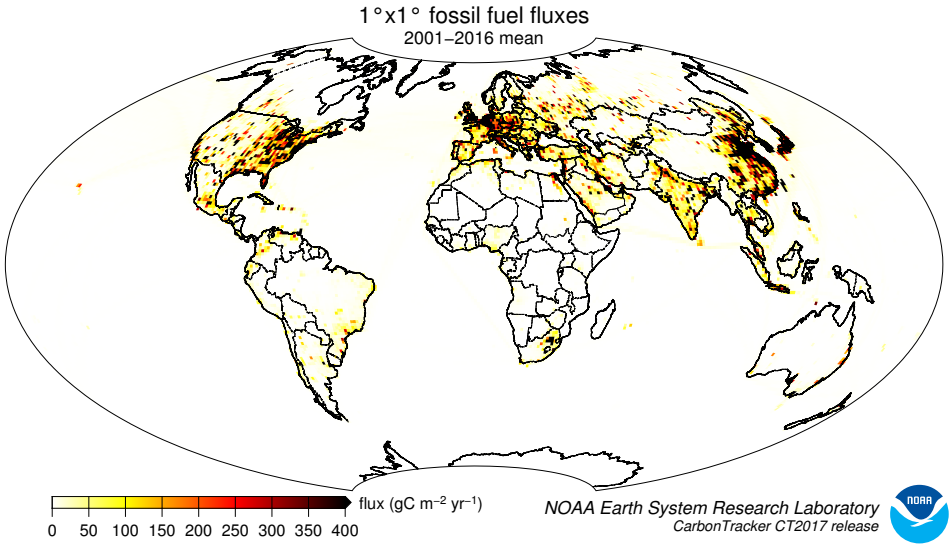

Figure 4: Spatial distribution of fossil fuel emissions. This is a spatial average of the Miller and ODIAC emissions inventories.

Dioxide Information and Analysis Center (CDIAC, Boden *et al.*2013) which extend through 2010. In order to estimate these fluxes through 2016, we extrapolate using the percentage increase or decrease for each fuel type (solid, liquid, and gas) in each country from the 2016 BP Statistical Review of World Energy for 2011-2016. To estimate emissions for the first few months of 2017 (required by CarbonTracker's 12-week assimilation window), no increase is applied to 2016 values.

- **Spatial Distribution** Miller fossil-fuel CO_2 fluxes are spatially distributed in two steps: First, the coarse-scale country totals through 2010 (from Boden *et al*. 2013) are mapped onto a $1^\circ \times 1^\circ$ grid according to the spatial patterns from the EDGAR v4.2 inventories (European Commission, 2009). The spatial pattern varies by year up until the end of the EDGAR v4.2 product in 2008. After this, the trends estimated in each pixel are linearly extrapolated. Note that while EDGAR provides annual emissions estimates at $1^\circ \times 1^\circ$ resolution, their totals do not agree with those from CDIAC. Thus, only the spatial patterns in EDGAR are used. The CDIAC country-by-country totals sum to about 95% of the global total emissions; the remaining 5% is mapped to global shipping routes according to EDGAR, which we treat as a proxy for bunker fuel emissions.
- **Temporal Distribution** For North America between 30 and 60°N, the Miller system imposes a seasonal cycle derived from the first and second harmonics (Thoning *et al*., 1989) of the Blasing *et al*. (2005) analysis for the United States. The Blasing analysis has ˜10% higher emissions in winter than in summer. This scheme defines a fixed fraction of emissions for each month, so while the shape of

the annual cycle is invariant, the amplitude of that cycle scales with the annual total emissions. For Eurasia, a set of seasonal emissions factors from EDGAR distributed by emissions sector is used to define fossil fuel seasonality. As in North America, this seasonality is imposed only from 30-60°N. The Eurasian seasonal amplitude is about 25%, significantly larger than that in North America, owing to the absence of a secondary summertime maximum due to air conditioning. See Figure 5 for the resulting time series of fossil fuel emissions. In order to avoid discontinuities in the fossil fuel emissions between consecutive years, a spline curve that conserves annual totals (Rasmussen 1991) is fit to seasonal emissions in each $1^\circ \times 1^\circ$ grid cell.

4.2 The "ODIAC" emissions dataset (ODIAC2016)

- **Global Totals** The ODIAC fossil fuel emission inventory (Oda and Maksyutov, 2011) is also derived from independent global and country emission estimates from CDIAC, but national emission estimates used were taken from the year 2016 edition of CDIAC estimates (Boden *et al*.2016). Annual country total fossil fuel CO_2 emissions from CDIAC which extend through 2013, were extrapolated through 2015 using the BP Statistical Review of World Energy. Difference between the CDIAC global total and country-by-country totals were ascribed to the entire emissions field. The same adjustment was done for the year extrapolated using using the CDIAC global total (2000-2015).
- **Spatial Distribution** ODIAC emissions are spatially distributed using many available "proxy data" that explain spatial extent of emissions according to emission types (emissions over land, gas flaring, aviation and marine bunker). Emissions over land were distributed in two steps: First, emissions attributable to power plants were mapped using geographical locations (latitude and longitude) provided by the global power plant dataset CARbon Monitoring and Action, CARMA. Next, the remaining land emissions (*i.e*. land total minus power plant emissions) were distributed using nightlight imagery collected by U.S. Air Force Defense Meteorological Satellite Project (DMSP) satellites. Emissions from gas flaring were also mapped using nightlight imagery. Emissions from aviation were mapped using flight tracks adopted from UK AERO2k air emission inventory. It should be noted that currently, air traffic emissions are emitted at ground level within CarbonTracker. Emissions from marine bunker fuels are placed entirely in the ocean basins along shipping routes according to patterns from the EDGAR database.

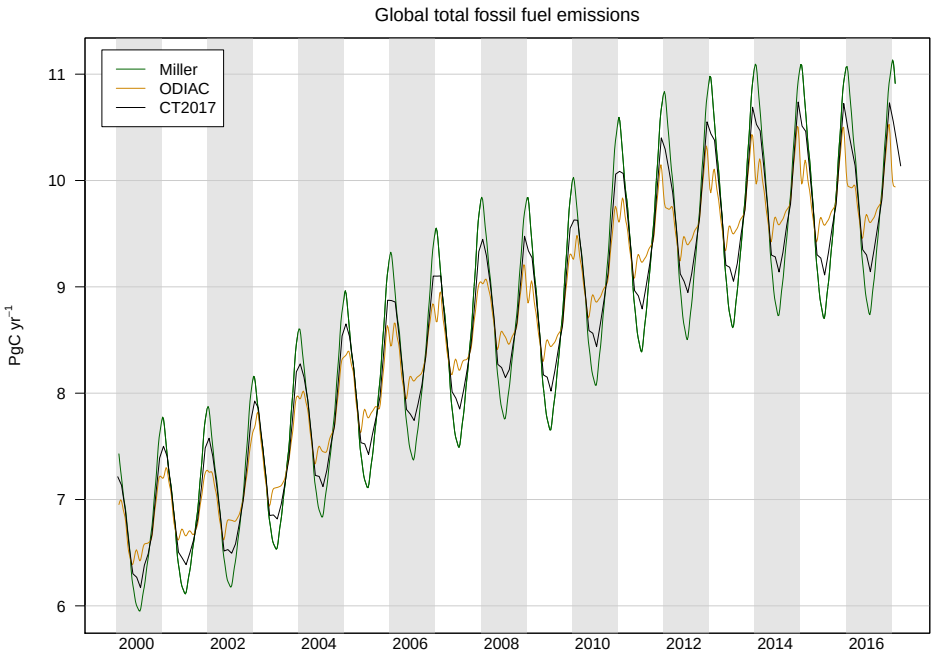

Figure 5: Time series of global fossil fuel emissions. The Miller (green) and ODIAC (tan) estimates are each used by half of the sixteen inversions in the CT2017 suite, so the CT2017 (black) inventory is effectively an average of Miller and ODIAC. Note that fossil fuel emissions are not optimized in CarbonTracker.

- **Temporal Distribution** The CDIAC estimates used for mapping emissions in ODIAC only describe how much CO_2 was emitted in a given year. To present seasonal changes in emissions, we used the CDIAC $1^\circ \times 1^\circ$ monthly fossil fuel emission inventory (Andres *et al*. 2011). The CDIAC monthly data utilizes the top 20 emitting countries' fuel (coal, oil and gas) consumption statistics available to estimate seasonal change in emissions. Monthly emission numbers at each pixel were divided by annual total and then a fraction to annual total was obtained. Monthly emissions in the ODIAC inventory were derived by multiplying this fraction by the emission in each grid cell.

4.3 Uncertainties

Marland (2008) attached an uncertainty of about 5% (95% confidence interval; approximately 2-σ) to the global total fossil fuel source. Recent estimates by Andres *et al*. (2014) put a larger uncertainty of 8.4% (2-σ) on the CDIAC global total. Uncertainties for individual regions of the world, and for sub-annual time periods are likely to be larger. Additional uncertainties are introduced when the emissions are distributed in space and time. In the Miller dataset, the overall Eurasian seasonality is based on scaling factors derived

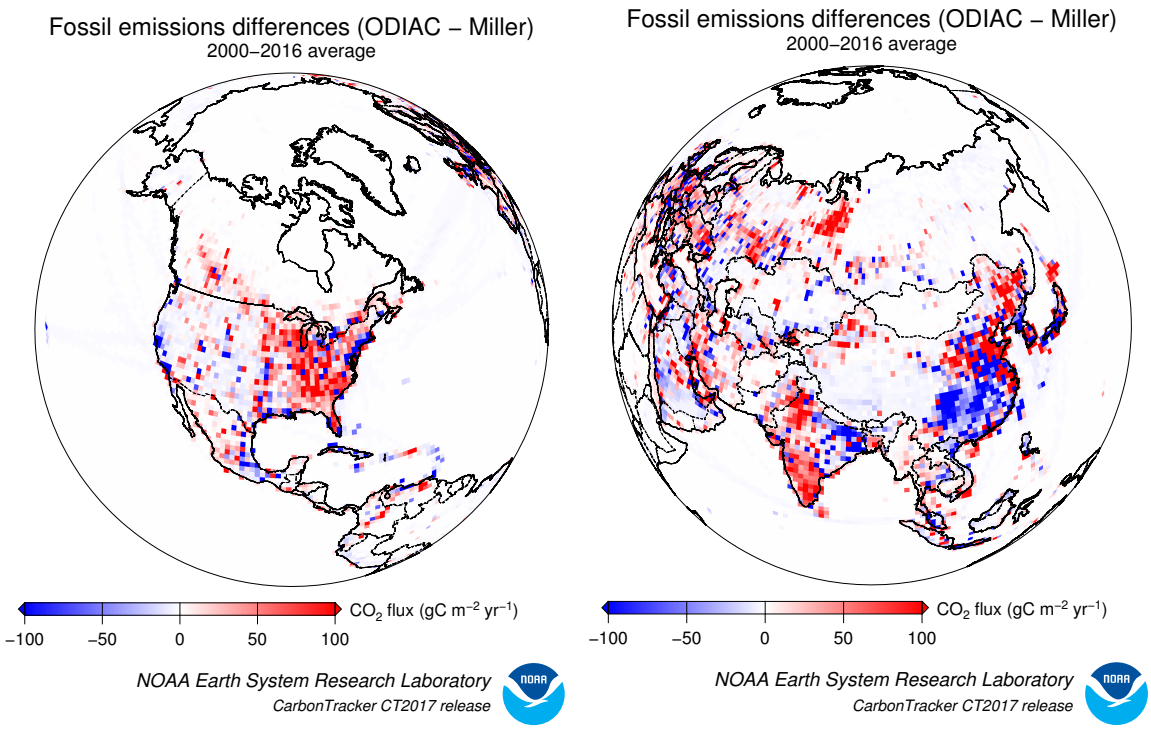

Figure 6: Spatial differences in long-term mean fossil fuel emissions between the two priors. Note that both the Miller and ODIAC emissions inventories use the same country totals, but have different models for spatial distribution of that flux within countries.

only from Western Europe and thus highly uncertain, but most likely a better representation than assuming no emission seasonality at all. Similarly, the use of the CDIAC monthly emission dataset for modeling seasonality introduces additional uncertainty in ODIAC. The additional uncertainty for the global total in the monthly CDIAC emission, which is solely due to the method for estimating seasonality, is reported as 6.4% (Andres *et al*. 2011). As mentioned earlier, fossil fuel emissions are not optimized in the current CarbonTracker system, similar to nearly all carbon data analysis systems. Spatial and temporal atmospheric CO_2 gradients arise from terrestrial biosphere and fossil-fuel sources. These gradients, which are interpreted by CarbonTracker, are difficult to attribute to one or the other cause. This is because atmospheric sampling sites have historically been established in locations remote from biospheric and anthropogenic sources, especially in the temperate Northern Hemisphere. Given that surface CO_2 flux due to biospheric activity and oceanic exchange is much more uncertain compared to fossil fuel emissions, CarbonTracker, like most current carbon dioxide data assimilation systems, does not attempt to optimize fossil fuel emissions. That is, the contribution of CO_2 from fossil fuel burning to observed CO_2 mole fractions is considered known. As detailed above, however, in CarbonTracker an effort is made to account for some aspects of fossil fuel

uncertainty by using two different fossil fuel estimates. From a technical point of view, extra land biosphere prior flux uncertainty is included in the system to represent the random errors in fossil fuel emissions. Eventually, fossil fuel emissions could be optimized within CarbonTracker, especially with the addition of $^{14}CO_2$ observations as constraints (Basu *et al*. 2016).

4.4 References

- Nassar, R., L. Napier-Linton, K. R. Gurney, R. J. Andres, T. Oda, F. R. Vogel, and F. Deng (2013), Improving the temporal and spatial distribution of CO_2 emissions from global fossil fuel emission data sets, J. Geophys. Res. Atmos., 118, 917933, doi:10.1029/2012JD018196.
- CDIAC Annual Global and National fluxes
- DOE Energy Information Administration (EIA)
- BP Statistical Review of World Energy
- EDGAR Database
- CDIAC (Blasing *et al*.) Monthly USA fluxes
- L.A Rasmussen, Piecewise integral splines of low degree, Computers & Geosciences, Volume 17, Issue 9, 1991, Pages 1255-1263, ISSN 0098-3004, http://dx.doi.org/10.1016/0098-3004(91)90027-B.
- Thoning, K. W., P. P. Tans, and W. D. Komhyr (1989), Atmospheric carbon dioxide at Mauna Loa Observatory: 2. Analysis of the NOAA GMCC data, 19741985, J. Geophys. Res., 94(D6), 85498565, doi:10.1029/JD094iD06p08549.
- Marland, G. (2008), Uncertainties in Accounting for CO_2 from Fossil Fuels, *Journal of Industrial Ecology*, 12(2), 136-139.
- Boden, T.A., G. Marland, and R.J. Andres. 2016. Global, Regional, and National Fossil-Fuel CO_2 Emissions. Carbon Dioxide Information Analysis Center, Oak Ridge National Laboratory, U.S. Department of Energy, Oak Ridge, Tenn., U.S.A. DOI: 10.3334/CDIAC/00001_V2016
- CDIAC Preliminary 2011 and 2012 Global and National Estimates)
- The Center for Global Development, CARbon Monitoring Action (CARMA) power plant database
- DMSP satellite nightlight data
- Centre for Air Transport and the Environment (CATE), AERO2k aviation emissions inventory

- Andres, R. J., J. S. Gregg, L. Losey, G. Marland, T. A. Boden (2011) Monthly, global emissions of carbon dioxide from fossil fuel consumption. *Tellus B*, 63:309-327. doi: 10.1111/j.1600-0889.2011.00530.x.
- Andres R.J., T.A. Boden, G. Marland, Monthly Fossil-Fuel CO_2 Emissions: Mass of Emissions Gridded by One Degree Latitude by One Degree Longitude, doi:10.3334/CDIAC/ffe.MonthlyMass.2015
- Oda, T. and Maksyutov, S.: A very high-resolution (1 km $\times$ 1 km) global fossil fuel CO_2 emission inventory derived using a point source database and satellite observations of nighttime lights, Atmos. Chem. Phys., 11, 543-556, doi:10.5194/acp-11-543-2011, 2011.
- European Commission, Joint Research Centre (JRC)/Netherlands Environmental Assessment Agency (PBL). (2009) Emission Database for Global Atmospheric Research (EDGAR), release version 4.0
- Andres, Robert J.; Boden, Thomas A.; Higdon, David (2014). A new evaluation of the uncertainty associated with CDIAC estimates of fossil fuel carbon dioxide emission. Tellus B, 66, doi:10.3402/tellusb.v66.23616
- S. Basu, J. B. Miller, and S. Lehman. Separation of biospheric and fossil fuel fluxes of CO_2 by atmospheric inversion of CO_2 and $^{14}CO_2$ measurements: Observation system simulations. Atmos. Chem. Phys, 16(9):56655683, 2016.

5 Oceans module

The oceans play an important role in the Earth's carbon cycle. They are the largest long-term sink for carbon and have an enormous capacity to store and redistribute CO_2 within the Earth system. Oceanographers estimate that about 48% of the CO_2 from fossil fuel burning has been absorbed by the ocean (Sabine *et al.*, 2004). The dissolution of CO_2 in seawater shifts the balance of the ocean carbonate equilibrium towards a more acidic state with a lower pH. This effect is already measurable (Caldeira and Wickett, 2003), and is expected to become an acute challenge to shell-forming organisms over the coming decades and centuries. Although the oceans as a whole have been a relatively steady net carbon sink, CO_2 can also be released from oceans depending on local temperatures, biological activity, wind speeds, and ocean circulation. These processes are all considered in CarbonTracker, since they can have significant effects on the ocean sink. Improved estimates of the air-sea exchange of carbon in turn help us to understand variability of both the atmospheric burden of CO_2 and terrestrial carbon exchange.

The initial release of CarbonTracker (CT2007) used climatogical estimates of CO_2 partial pressure in surface waters (pCO_2) from Takahashi *et al.* (2002) to compute a first-guess air-sea flux. This air-sea pCO_2

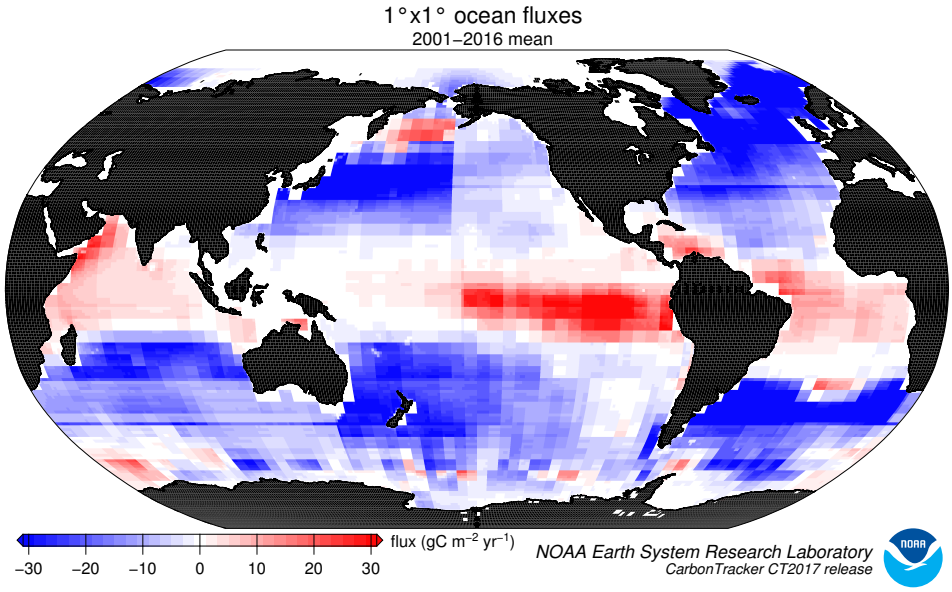

Figure 7: Posterior long-term mean ocean fluxes from CarbonTracker. The pattern of air-sea exchange of CO_2 averaged over the time period indicated, as estimated by CarbonTracker. Negative fluxes (blue colors) represent CO_2 uptake by the ocean, whereas positive fluxes (red colors) indicate regions in which the ocean is a net source of CO_2 to the atmosphere. Units are $\mathrm{gC\,m^{-2}\,yr^{-1}}$.

disequilibrium was modulated by a surface barometric pressure correction before being multiplied by a gas-transfer coefficient to yield a flux. Starting with CT2007B and continuing through the CT2011_oi release, the air-sea pCO_2 disequilibrium was imposed from analysis of ocean inversions ("OIF", *cf.* Jacobson *et al.*, 2007) results, with short-term flux variability derived from the atmospheric model wind speeds via the gas transfer coefficient. The barometric pressure correction was removed so that climatological high- and low-pressure cells did not bias the long-term means of the first guess fluxes.

In CT2017, two models are used to provide prior estimates of air-sea CO_2 flux. The OIF scheme provides one of these flux priors, and the other is an updated version of the Takahashi *et al.* pCO_2 climatology.

5.1 Air-sea gas exchange

Oceanic uptake of CO_2 in CarbonTracker is computed using air-sea differences in partial pressure of CO_2 inferred either from ocean inversions (called "OIF" henceforth), or from a compilation of direct measurements of seawater pCO_2 (called "pCO_2-clim" henceforth). These air-sea partial pressure differences are combined with a gas transfer velocity computed from wind speeds in the atmospheric transport model to compute fluxes of carbon dioxide across the sea surface.

In either method, the first-guess fluxes have no interannual variability (IAV) other than a smooth trend.

IAV in oceanic CO_2 flux is due to anomalies in surface pCO_2, such as those that occur in the tropical eastern Pacific during an El Niño, and to associated variability in winds, ocean circulation, and sea-surface properties. In CarbonTracker, only the surface winds (and hence gas transfer), manifest these interannual anomalies; the remaining IAV of flux must be inferred from atmospheric CO_2 signals.

In the following sections we describe the two ocean flux prior models. We then describe the air-sea gas transfer velocity parameterization and discuss detais of the inversion methodology specific to oceanic exchange of CO_2.

5.2 OIF: the Ocean Inversion Fluxes prior

For the OIF prior, long-term mean air-sea fluxes and the uncertainties associated with them are derived from the ocean interior inversions reported in Jacobson *et al*. (2007). These ocean inversion flux estimates are composed of separate preindustrial (natural) and anthropogenic flux inversions based on the methods described in Gloor *et al*. (2003) and biogeochemical interpretations of Gruber, Sarmiento, and Stocker (1996). The uptake of anthropogenic CO_2 by the ocean is assumed to increase in proportion to atmospheric CO_2 levels, consistent with estimates from ocean carbon models.

OIF contemporary pCO_2 fields were computed by summing the preindustrial and anthropogenic flux components from inversions using five different configurations of the Princeton/GFDL MOM3 ocean general circulation model (Pacanowski and Gnanadesikan, 1998), then dividing by a gas transfer velocity computed from the European Centre for Medium-Range Weather Forecasts (ECMWF) ERA40 reanalysis. There are two small differences in first-guess fluxes in this computation from those reported in Jacobson *et al*. (2007). First, the five OIF estimates all used Takahashi *et al*. (2002) pCO_2 estimates to provide high-resolution patterning of flux within inversion regions (the alternative "forward" model patterns were not used). To good approximation, this choice only affects the spatial and temporal distribution of flux within each of the 30 ocean inversion regions, not the magnitude of the estimated flux. Second, wind speed differences between the ERA40 product used in the offline analysis and the ECMWF operational model used in the online CarbonTracker analysis result in small deviations from the OIF estimates.

Other than the smooth trend in anthropogenic flux assumed by the OIF results, interannual variability (IAV) in the first guess ocean flux comes entirely from wind speed effects on the gas transfer velocity. This is because the ocean inversions retrieve only a long-term mean and smooth trend.

5.3 $p\mathrm{CO_2}$-Clim: Takahashi *et al*. (2009) climatology prior

The $p\mathrm{CO_2}$-Clim prior is derived from the Takahashi *et al*. (2009) climatology of seawater $p\mathrm{CO_2}$. This climatology was created from about 3 million direct observations of seawater $p\mathrm{CO_2}$ around the world between 1970 and 2007. With the exception of measurements in the Bering Sea, these observations were all linearly extrapolated to the corresponding month of the year 2000 by assuming a constant trend of 1.5 μatm yr^{-1}. This set of global monthly measurements corrected to the reference year 2000 was then interpolated onto a regular grid using a modeled surface current field.

The Takahashi *et al*. (2009) product goes beyond providing this estimate of surface water $p\mathrm{CO_2}$. They also compute climatological air-sea exchange of $\mathrm{CO_2}$ by using the GLOBALVIEW-$\mathrm{CO_2}$ atmospheric carbon dioxide product to compute air-sea $\Delta p\mathrm{CO_2}$, sea surface properties inferred from ocean climatologies, and winds from atmospheric reanalysis to estimate gas-transfer velocity. Unlike many other atmospheric analyses, we have chosen not to use the climatological fluxes as our prior, nor to use the climatological $\Delta p\mathrm{CO_2}$. Instead, we take only the seawater $p\mathrm{CO_2}$ distribution from the Takahashi *et al*. climatology–our atmospheric model provides both $p\mathrm{CO_2}$ in the air at the sea surface and the winds needed to estimate gas transfer. Seawater $p\mathrm{CO_2}$ is extrapolated from 2000 to the actual year of the CarbonTracker simulation using a presumed increase of 1.5 μatm yr^{-1} at every point in the global ocean. This is the same trend used in Takahashi *et al*. to normalize observations from many years to the reference year of the analysis (2000).

5.4 Gas-transfer velocity and ocean surface properties

Both priors use $\mathrm{CO_2}$ solubilities and Schmidt numbers computed from World Ocean Atlas 2009 (WOA09) climatological fields of sea surface temperature (Locarnini *et al*., 2010) and sea surface salinity (Antonov *et al*., 2010) fields. Gas transfer velocity in CarbonTracker is parameterized as a quadratic function of wind speed following Wanninkhof (1992), using the formulation for instantaneous winds. Gas exchange is computed every 3 hours using wind speeds from the ECMWF operational model as represented by the atmospheric transport model.

Air-sea transfer is inhibited by the presence of sea ice, and for this work fluxes are scaled by the daily sea ice fraction in each gridbox provided by the ECMWF forecast data.

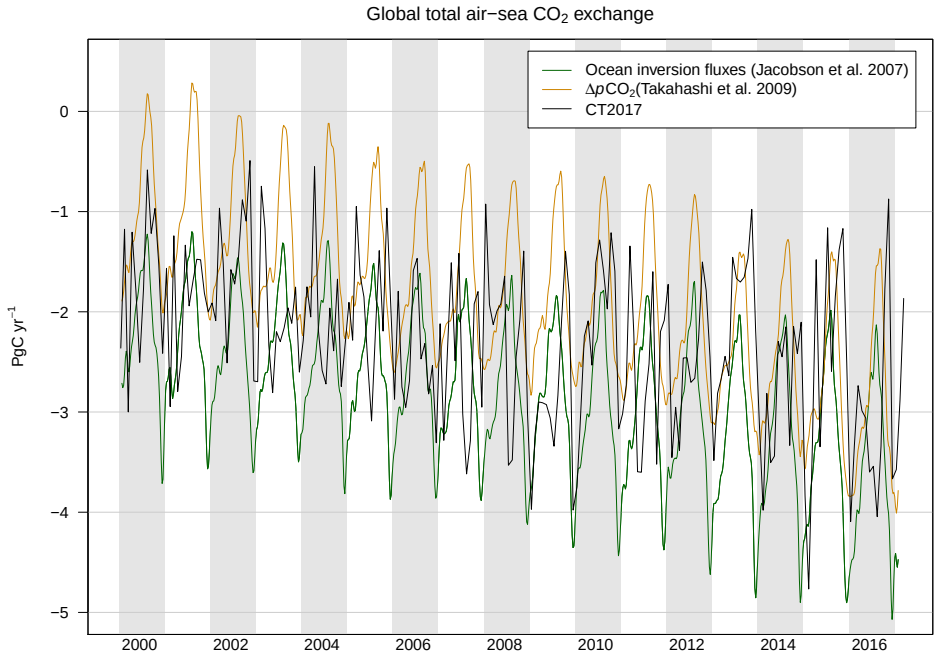

Figure 8: Comparison of air-sea flux priors and the CT2017 posterior. Global CO_2 uptake by the ocean, expressed in PgC yr^{-1}. Positive flux represents a gain of CO_2 to the atmosphere, and the negative numbers here indicate that the ocean is a sink of CO_2. While both priors manifest similar trends of increasing oceanic uptake of CO_2, the OIF prior (in green) has more oceanic uptake and a greater annual cycle than the pCO_2-clim prior (in tan). The CT2017 across-model posterior estimate is shown in black for comparison.

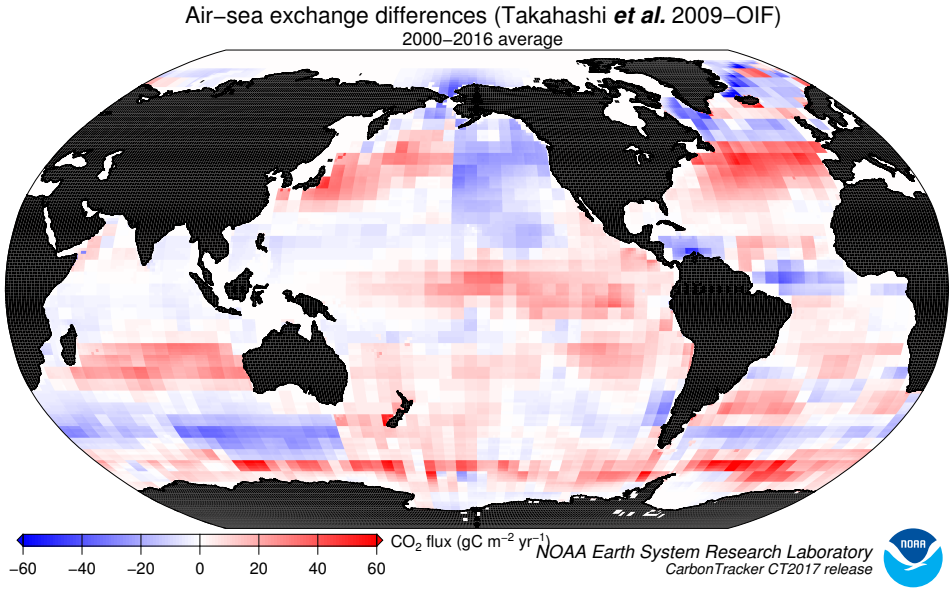

Figure 9: Differences in long-term mean ocean fluxes between the two priors. Red indicates areas where the pCO_2-clim prior has less oceanic uptake (or more outgassing to the atmosphere) than the OIF prior, and blue represents the opposite. Units are gC m-2 yr-1.

5.5 Specifics of the inversion methodology related to air-sea CO_2 fluxes

The first-guess fluxes described here are subject to scaling during the CarbonTracker optimization process, in which atmospheric CO_2 mole fraction observations are combined with transport simulated by the atmospheric model to infer flux signals. Prior air-sea fluxes are adjusted within each of of the 30 ocean inversion regions. In this process, signals of terrestrial flux in atmospheric CO_2 distribution can be erroneously interpreted as being caused by oceanic fluxes. This flux "aliasing" or "leakage" is evident in some regions as a change in the shape of the seasonal cycle of air-sea flux.

Prior uncertainties for the OIF and pCO_2-clim models are specified as uncertainties on scaling factors multiplying net CO_2 flux in each of the 30 ocean inversion regions. The pCO_2-clim prior has independent regional uncertainties (a diagonal prior covariance matrix), with the uncertainty standard deviation on each region set to 40%. The OIF prior uncertainty has a fully-covariate covariance matrix with off-diagonal elements representing the results of the ocean inversion of Jacobson *et al*. (2007). The pre-industrial flux uncertainty is time-independent, but the anthropogenic flux uncertainty grows in time as anthropogenic flux uptake increases. The latter is scaled to the simulation date, then added to the former. Total uncertainties are consistent with the Jacobson *et al*. (2007) results.

5.6 References

- NOAA Pacific Marine Environmental Laboratory
- Ocean Acidification
- Locarnini, R. A., A. V. Mishonov, J. I. Antonov, T. P. Boyer, H. E. Garcia, O. K. Baranova, M. M. Zweng, and D. R. Johnson, 2010. World Ocean Atlas 2009, Volume 1: Temperature. S. Levitus, Ed. NOAA Atlas NESDIS 68, U.S. Government Printing Office, Washington, D.C., 184 pp.
- Antonov, J. I., D. Seidov, T. P. Boyer, R. A. Locarnini, A. V. Mishonov, H. E. Garcia, O. K. Baranova, M. M. Zweng, and D. R. Johnson, 2010. World Ocean Atlas 2009, Volume 2: Salinity. S. Levitus, Ed. NOAA Atlas NESDIS 69, U.S. Government Printing Office, Washington, D.C., 184 pp.
- Caldeira, K., and M. E. Wickett (2003), Anthropogenic carbon and ocean pH, Nature, 425365-365, doi:10.1038/425365a
- GLOBALVIEW-CO2 Cooperative Atmospheric Data Integration Project - Carbon Dioxide. CD-ROM, NOAA ESRL, Boulder, Colorado (Also available on Internet via anonymous FTP to ftp.cmdl.noaa.gov,

Path: ccg/co2/GLOBALVIEW), 2011.

- Gloor, M., N. Gruber, J. Sarmiento, C. L. Sabine, R. A. Feely, and C. Rdenbeck (2003), A first estimate of present and preindustrial air-sea CO_2 flux patterns based on ocean interior carbon measurements and models, Geophysical Research Letters, 30, doi: 10.1029/2002GL015594.
- Gruber, N., J. L. Sarmiento, and T. F. Stocker (1996), An improved method for detecting anthropogenic CO2 in the oceans, Global Biogeochem. Cycles, 10(4), 809837, doi:10.1029/96GB01608.
- Jacobson, A. R., S. E. Mikaloff Fletcher, N. Gruber, J. L. Sarmiento, and M. Gloor (2007), A joint atmosphere-ocean inversion for surface fluxes of carbon dioxide: 1. Methods and global-scale fluxes, Global Biogeochem. Cycles, 21, GB1019, doi:10.1029/2005GB002556.
- Ronald C. Pacanowski and Anand Gnanadesikan, 1998: Transient Response in a Z-Level Ocean Model That Resolves Topography with Partial Cells. Mon. Wea. Rev., 126, 32483270. doi: http://dx.doi.org/10.1175/1 0493(1998)126¡3248:TRIAZL¿2.0.CO;2
- Sabine, C. L., R. A. Feely, N. Gruber, R. M. Key, K. Lee, J. L. Bullister, R. Wanninkhof, C. S. Wong, D. W. R. Wallace, B. Tilbrook, F. J. Millero, T. H. Peng, A. Kozyr, T. Ono, and A. F. Rios (2004), The oceanic sink for anthropogenic CO_2, Science, 305, 367-371, DOI: 10.1126/science.1097403
- Taro Takahashi, Stewart C. Sutherland, Colm Sweeney, Alain Poisson, Nicolas Metzl, Bronte Tilbrook, Nicolas Bates, Rik Wanninkhof, Richard A. Feely, Christopher Sabine, Jon Olafsson, Yukihiro Nojiri, Global seaair CO_2 flux based on climatological surface ocean pCO_2, and seasonal biological and temperature effects, Deep Sea Research Part II: Topical Studies in Oceanography, Volume 49, Issues 910, 2002, Pages 1601-1622, ISSN 0967-0645, http://dx.doi.org/10.1016/S0967-0645(02)00003-6.
- Taro Takahashi, Stewart C. Sutherland, Rik Wanninkhof, Colm Sweeney, Richard A. Feely, David W. Chipman, Burke Hales, Gernot Friederich, Francisco Chavez, Christopher Sabine, Andrew Watson, Dorothee C.E. Bakker, Ute Schuster, Nicolas Metzl, Hisayuki Yoshikawa-Inoue, Masao Ishii, Takashi Midorikawa, Yukihiro Nojiri, Arne Krtzinger, Tobias Steinhoff, Mario Hoppema, Jon Olafsson, Thorarinn S. Arnarson, Bronte Tilbrook, Truls Johannessen, Are Olsen, Richard Bellerby, C.S. Wong, Bruno Delille, N.R. Bates, Hein J.W. de Baar, Climatological mean and decadal change in surface ocean pCO_2, and net sea-air CO_2 flux over the global oceans, Deep Sea Research Part II: Topical Studies in Oceanography, Volume 56, Issues 810, April 2009, Pages 554-577, ISSN 0967-0645, http://dx.doi.org/10.1016/j.dsr2.2008.12.009.

- Wanninkhof, R. (1992), Relationship between wind speed and gas exchange over the ocean, J. Geophys. Res., 97(C5), 73737382, doi:10.1029/92JC00188.

6 Atmospheric transport

The link between observations of CO_2 in the atmosphere and the exchange of CO_2 at the Earth's surface is transport in the atmosphere: storm systems, cloud complexes, and weather of all sorts cause winds that transport CO_2 around the world. As a result, local surface CO_2 exchange events like fires, forest growth, and ocean upwelling can have impacts at remote locations. To simulate the winds and the weather, CarbonTracker uses sophisticated numerical models that are driven by the daily weather forecasts from the specialized meteorological centers of the world. Since CO_2 does not decay or react in the lower atmosphere, the influence of emissions and uptake in locations such as North America and Europe are ultimately seen in our measurements even at the South Pole. Getting the transport of CO_2 just right is an enormous challenge, and costs us almost all of the computer resources for CarbonTracker. To represent the atmospheric transport, we use the Transport Model 5 (TM5). This is a community-supported model whose development is shared among many scientific groups with different areas of expertise. TM5 is used for many applications other than CarbonTracker, including forecasting air-quality, studying the dispersion of aerosols in the tropics, tracking biomass burning plumes, and predicting pollution levels that future generations might have to deal with.

6.1 TM5 offline tracer transport model

TM5 is an offline global chemical transport model with two-way nested grids. In this global model, regions for which high-resolution simulations are desired can be nested in the coarser global grid. The advantage to this approach is that transport simulations can be performed with a regional focus without the need for boundary conditions. Further, this approach allows measurements outside the "zoom" domain to constrain regional fluxes in the data assimilation, and ensures that regional estimates are consistent with global constraints. TM5 is based on a predecessor model TM3, with improvements in the advection scheme, vertical diffusion parameterization, and meteorological preprocessing of the wind fields (Krol *et al.*, 2005).

The model is developed and maintained jointly by the Institute for Marine and Atmospheric Research Utrecht (IMAU, The Netherlands), the Joint Research Centre (JRC, Italy), the Royal Netherlands Meteo-

rological Institute (KNMI), the Netherlands Institude for Space Research (SRON), and the NOAA Earth System Research Laboratory (ESRL).

In CarbonTracker, TM5 separately simulates advection, deep and shallow convection, and vertical diffusion in both the planetary boundary layer and free troposphere. The carbon dioxide concentrations predicted by CarbonTracker do not feed back onto these predictions of winds.

Prior to use in TM5, ECMWF meteorological data are preprocessed into coarser grids, with attention to retrieving a flow that conserves tracer mass. Like most numerical weather prediction models, advection in the parent ECMWF model is not strictly mass-conserving, so this step is crucial. In CarbonTracker, TM5 is currently run at a global 3° longitude $\times$ 2° latitude resolution with a nested regional grid over North America at $1^\circ \times 1^\circ$ resolution (Figure 10). TM5 uses a dynamically-variable time step with a maximum length of 90 minutes. This overall timestep is dynamically reduced to maintain numerical stability, generally during times of high wind speeds. The timestep is divided in half and individual advection, diffusion, convection, and chemistry operators are applied symmetrically in each half step. Furthermore, transport operators in nested grids are modeled at shorter timesteps, so processes at the finest scales are conducted at an effective timestep of one-quarter the overall timestep. See Krol *et al*. (2005) for details.

The winds which drive TM5 come from the ERA-interim reanalysis implemented in the European Centre for Medium-Range Weather Forecasts (ECMWF) modeling system. The ERA-Interim reanalysis uses Cy31r2 version of the ECMWF Integrated Forecast System (IFS) model, which was used for the operational forecasts up until June 2007. That model uses a 30-minute time step and a a spectral T255 horizontal resolution, which corresponds to approximately 79 km spacing on a reduced Gaussian grid. This version of the IFS has 60 model layers in the vertical, of which TM5 uses a 25-layer subset. These levels are listed in Table 1.

6.2 Convective flux fix

Until recently, TM5 was known to have difficulties representing the global surface distribution of sulfur hexafluoride (SF_6, see Figure 11 and Peters *et al*., 2004). SF_6 is a nearly inert tracer in the atmosphere, with very small surface and atmospheric sinks and an atmospheric lifetime of about 1,000 years. Consequently, its global budget is very well known from observations alone. It is thought to be released mainly via leakage from electrical transformers. Since the electrical distribution system is closely tied to fossil fuel consumption, SF_6 is often considered an analog for fossil fuel CO_2 in the atmosphere. It is useful for understanding

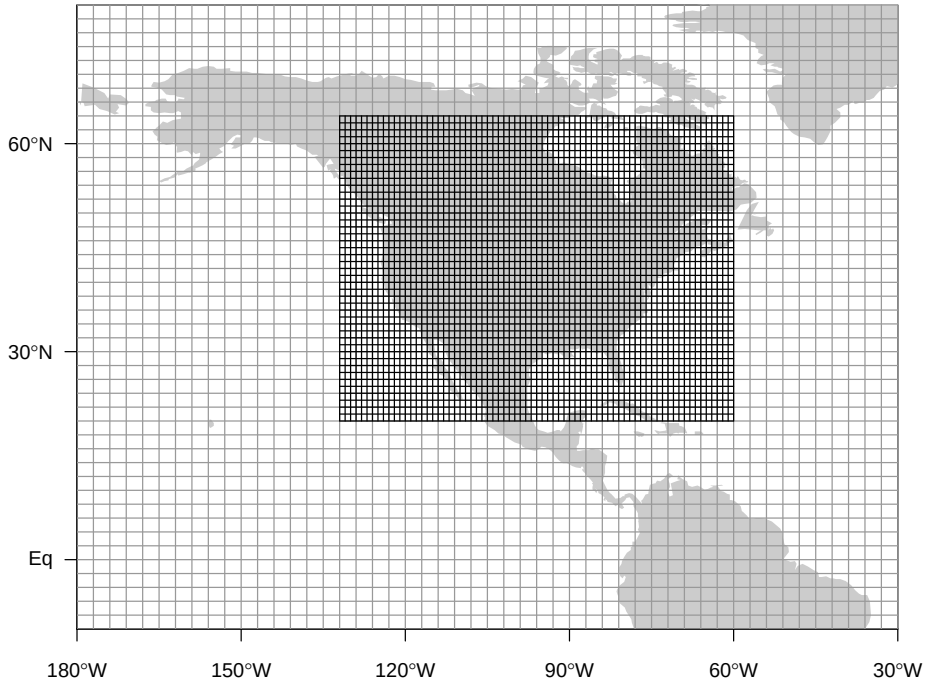

Figure 10: Nested grids used in CarbonTracker over North America. TM5 is a global model, but it employs nested grids to provide higher resolution over regions of interest. This figure shows the $1^\circ \times 1^\circ$ nested regional grid over North America and a portion of the global 3° longitude $\times$ 2° latitude grid.

Model Level	Mean Height (m)	Model Level	Mean Height (m)
1	25	14	9114
2	103	15	10588
3	247	16	12184
4	480	17	13928
5	814	18	15843
6	1259	19	17983
7	1822	20	20412
8	2508	21	24433
9	3317	22	30003
10	4248	23	35895
11	5300	24	43210
12	6467	25	123622
13	7741		

Table 1: Mean mid-level heights above ground in meters for the TM5 model using ERA-interim transport.

the rate at which Northern Hemisphere land surfaces are ventilated to the free troposphere, and the rate of interhemispheric exchange in models (Patra *et al*., 2011).

As a result of more than a decade's worth of work on understanding the apparently sluggish mixing in

TM5 as revealed by SF_6 simulations, a fault in one of the vertical mixing parameterizations of the model was discovered. When it was originally created, TM5 implemented the same planetary boundary layer (PBL) mixing and convection schemes as the parent ECMWF model. Recent comparisons between TM5, the ECMWF parent model, and radiosonde profile data show that the PBL scheme in TM5 performs similarly to that of the parent ECMWF model. The convective scheme, however, does not produce similar results in TM5 as compared to the ECMWF model.

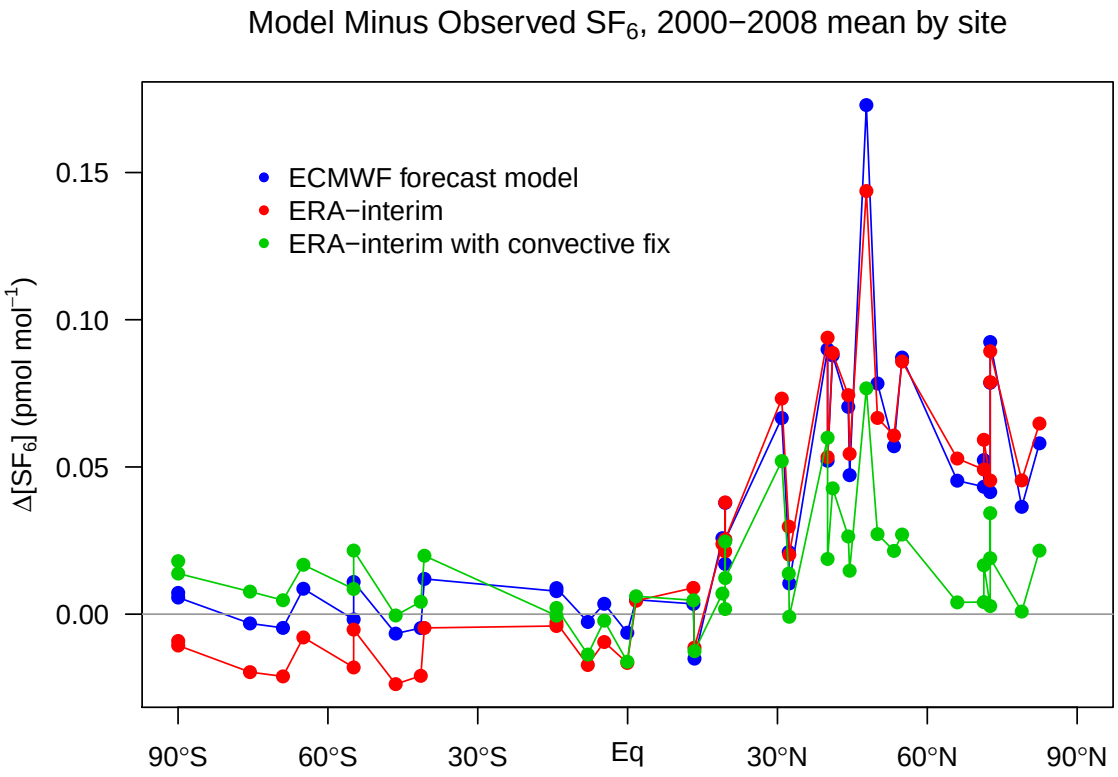

Figure 11: Long-term mean model residuals of SF_6 concentrations as a function of latitude. Residuals are defined as model-minus-observation, so a positive residual indicates the model has too much SF_6. Three different transport model simulations are shown. The ECMWF forecast (blue) and ERA-interim (red) transport simulations do not include the recent "convective flux fix". The ERA-interim with this convective flux fix is shown in green. Units are pmol mol^{-1}, or parts per trillion. CT2017 uses the ERA-interim transport with the convective flux fix.

In a previous configuration of TM5, the convective entrainment and detrainment mass fluxes of the parent ECMWF model were re-diagnosed within TM5 using other meteorological information. The ECMWF model is used to produce both operational forecasts and the ERA-interim reanalysis, but the convective fluxes are stored for the ERA-interim product only. Thus, using ERA-interim meteorology, a direct comparison is possible. This comparison revealed that the TM5 internal rediagnosis of convective fluxes was

faulty. TM5 was subsequently modified to use parent model ERA-interim convective fluxes directly. Using the parent model convective fluxes result in a significantly better SF_6 simulations. Simulations with these parent-model convective fluxes are said to use the "convective flux fix". Simulations with the convective flux fix show significantly improved agreement with SF_6 observations (see Figure 11).

Since the parent-model convective fluxes are only available for the ERA-interim product, CT2017 uses only ERA-interim transport with the convective flux fix. Previous releases of CarbonTracker also used the ECMWF operational model transport, for which parent-model convective fluxes are not available. We believe that TM5 simulations without the parent-model convective fluxes are faulty and should not be included in our product. When the convective flux fix was instituted in CT2013B, it resulted in the largest realignment of surface CO_2 fluxes in the history of the CarbonTracker program. This is a prominent example of the sensitive reliance of atmospheric inversions on accurate atmospheric transport.

6.3 References

- Krol, M., Houweling, S., Bregman, B., van den Broek, M., Segers, A., van Velthoven, P., Peters, W., Dentener, F., and Bergamaschi, P.: The two-way nested global chemistry-transport zoom model TM5: algorithm and applications, Atmos. Chem. Phys., 5, 417-432, doi:10.5194/acp-5-417-2005, 2005.

- Krol, M., Houweling, S., Bregman, B., van den Broek, M., Segers, A., van Velthoven, P., Peters, W., Dentener, F., and Bergamaschi, P.: The two-way nested global chemistry-transport zoom model TM5: algorithm and applications, Atmos. Chem. Phys., 5, 417-432, doi:10.5194/acp-5-417-2005, 2005.

- Denning, A. S., Holzer, Mark., Gurney, K. R., Heimann, M., Law, R. M., Rayner, P. J., Fung, I. Y., Fan, S.-M., Taguchi, S., Friedlingstein, P., Balkanski, Y., Taylor, J., Maiss, M. and Levin, I. (1999), Three-dimensional transport and concentration of SF_6. Tellus B, 51: 266297. doi: 10.1034/j.1600-0889.1999.00012.x
- Patra, P. K., Houweling, S., Krol, M., Bousquet, P., Belikov, D., Bergmann, D., Bian, H., Cameron-Smith, P., Chipperfield, M. P., Corbin, K., Fortems-Cheiney, A., Fraser, A., Gloor, E., Hess, P., Ito, A., Kawa, S. R., Law, R. M., Loh, Z., Maksyutov, S., Meng, L., Palmer, P. I., Prinn, R. G., Rigby, M., Saito, R., and Wilson, C.: TransCom model simulations of CH4 and related species: linking transport, surface flux and chemical loss with CH4 variability in the troposphere and lower stratosphere, Atmos. Chem. Phys., 11, 12813-12837, doi:10.5194/acp-11-12813-2011, 2011.

- Peters, W., M. C. Krol, E. J. Dlugokencky, F. J. Dentener, P. Bergamaschi, G. Dutton, P. v. Velthoven, J. B. Miller, L. Bruhwiler, and P. P. Tans (2004), Toward regional-scale modeling using the two-way nested global model TM5: Characterization of transport using SF_6, J. Geophys. Res., 109, D19314, doi:10.1029/2004JD005020

7 Observations

The observations of atmospheric CO_2 mole fraction made by NOAA ESRL and partner laboratories are at the heart of CarbonTracker. They inform us on changes in the carbon cycle, whether those changes are regular (such as the annual cycle of growth and decay of leaves and other plant matter), or irregular (such as the release of tons of carbon by a wildfire). The results in CarbonTracker depend directly on the quality, location, and frequency of avaiable observations. The level of detail at which we can retrieve information on the carbon cycle increases strongly with the density of the CO_2 observing network.

7.1 The CarbonTracker observational network

Observations simulated by CT2017 are suppplied by the GLOBALVIEW+ data product, available at the NOAA ESRL ObsPack web site. This study uses measurements of air samples collected at 254 sites around the world by 55 laboratories:

- Commonwealth Scientific and Industrial Research Organization, Oceans & Atmosphere Flagship - GASLAB (CSIRO)
- Instituto de Pesquisas Energeticas e Nucleares (IPEN)
- Environment and Climate Change Canada (ECCC)
- Finnish Meteorological Institute (FMI)
- Laboratoire des Sciences du Climat et de l'Environnement - UMR8212 CEA-CNRS-UVSQ (LSCE)
- University of Heidelberg, Institut für Umweltphysik (UHEI-IUP)
- Umweltbundesamt, Station Schauinsland (UBA-SCHAU)
- Hungarian Meteorological Service (HMS)
- Center for Atmospheric and Oceanic Studies, Tohoku University (TU)
- Meteorological Research Institute (MRI)
- Japan Meteorological Agency (JMA)
- National Institute for Environmental Studies (NIES)
- Comprehensive Observation Network for TRace gases by AirLiner (CONTRAIL)
- University of Groningen (RUG), Centre for Isotope Research (CIO) (RUG)
- Energy Research Centre of the Netherlands (ECN)
- National Institute of Water and Atmospheric Research (NIWA)
- University of Science and Technology (AGH)
- South African Weather Service (SAWS)

- Izana Atmospheric Research Center, Meteorological State Agency of Spain (AEMET)
- Swiss Federal Laboratories for Materials Science and Technology (EMPA)
- World Meteorological Organization/Global Atmosphere Watch (WMO/GAW)
- University of Bern, Physics Institute, Climate and Environmental Physics (KUP)
- University of East Anglia (UEA)
- NOAA Global Monitoring Division (NOAA)
- National Center For Atmospheric Research (NCAR)
- Scripps Institution of Oceanography (SIO)
- Harvard University (HU)
- Lawrence Berkeley National Laboratory and ARM Climate Research Facility (LBNL-ARM)
- HIAPER Pole-to-Pole Observations project (HIPPO)
- University of Wisconsin (UOFWI)
- Savannah River National Laboratory (SRNL)
- Lawrence Berkeley National Laboratory (LBNL)
- National Institute for Space Research (INPE)
- University of Helsinki (UHELS)
- Hohenpeissenberg Meteorological Observatory (HPB)
- Ricerca sul Sistema Energetico (RSE)
- Institut de Ciencia i Tecnologia Ambientals, Universitat Autonoma de Barcelona (ICTA-UAB)
- Lund University - Centre for Environmental and Climate Research (LUND-CEC)
- CarboCount-CH (CARBOCOUNT-CH)
- AVOCET Group @ NASA LaRC (NASA-LARC)
- Penn State University (PSU)
- Oregon State University (OSU)
- NOAA ESRL Halocarbons and Other Atmospheric Trace Species (NOAA-HATS)
- AmeriFlux Network (AMERIFLUX)
- University of Minnesota (UOFMN)
- NOAA Chemical Sciences Division (NOAA-CSD)
- California Institute of Technology, Division of Geological and Planetary Science (CALTECH)
- University of Virginia (UOFVA)
- Indianapolis Flux Experiment (INFLUX)
- Carbon in Arctic Reservoirs Vulnerability Experiment, NASA Earth Ventures (CARVE)
- Utah Atmospheric Trace gas & Air Quality (U-ATAQ)
- NASA Goddard Space Flight Center (NASA-GSFC)

The CO_2 measurement data assimilated in CT2017 are freely available for download from the ESRL ObsPack web portal or from partner websites. The bulk of assimilated measurements come from GLOBALVIEWplus v3.1 (2017) and from the NRT ObsPack v4.0 product. Additional observations were gathered from specialized ObsPack products as detailed in Table 2.

We also make available an ObsPack containing the simulated values of all measurement data considered by CT2017. This CT2017 ObsPack contains most, but not all, of the measured values. Measured values are only distributed directly when we have permission to do so.

Source	Online availability	Comment
GLOBALVIEW+ v3.1	ObsPack download	Main source of observations
NRT v4.0	ObsPack download	Measurements in 2017 & 2018 GLOBALVIEW+ 3.1
NIES shipboard observations	Available from NIES	No permission to redistribute
ORCAS campaign	ObsPack download	Also distributed in the GLOBALV (2017) ObsPack
CONTRAIL	Available upon request to Yousuke SAWA and Toshinobu MACHIDA; ask for access to CONTRAIL restricted ObsPack	No permission to redistribute
ASCENDS-GSFC aircraft campaigns	ObsPack download	Slated for inclusion in GLOBA (summer 2018)
NIES JR-STATION Siberia towers	Download from NIES website or Available upon request to Motoki Sasakawa; ask for access to JR-STATION restricted ObsPack	No permission to redistribute
Extended NOAA tower datasets with all levels and all hours of day	ObsPack download	Slated for inclusion in GV+ 4.0 (2
AirCore	Available upon request to Colm Sweeney; ask for access to AirCore restricted ObsPack	No permission to redistribute
INPE (Brazil) aircraft data	Available upon request to Luciana Gatti; ask for access to INPE restricted ObsPack	No permission to redistribute

Table 2: Sources of CO_2 observational data for CT2017

Users are encouraged to review the usage requirements for these data products, and to contact the measurement laboratories directly for details about the observations.

With the advent in 2015 of GLOBALVIEW+, data are now presented to CarbonTracker with a higher temporal frequency than in past observational products. At sites with quasi-continuous monitoring, CT2017 now assimilates hourly average CO_2 concentrations. In the past, a single daily assimilation value was constructed at these sites, generally a four-hour average during well-mixed background conditions. At continental sites, this four-hour period was generally from local noon to 4pm; at many mountain sites background conditions are met at nighttime when upslope winds are uncommon. With GLOBALVIEW+, CarbonTracker now assimilates each hourly average during these background conditions independently. For many sites, all available hourly averages throughout the day are assimilated. Details vary by dataset, but can be checked at the interactive data plotting page.

Note that all of these observations are calibrated against the same world CO_2 standard (WMO-X2007).

Starting with GLOBALVIEW+, we generally use the recommendations of data providers as to which observations are appropriate for assimilation. Such observations are identified by a variable in the Ob-

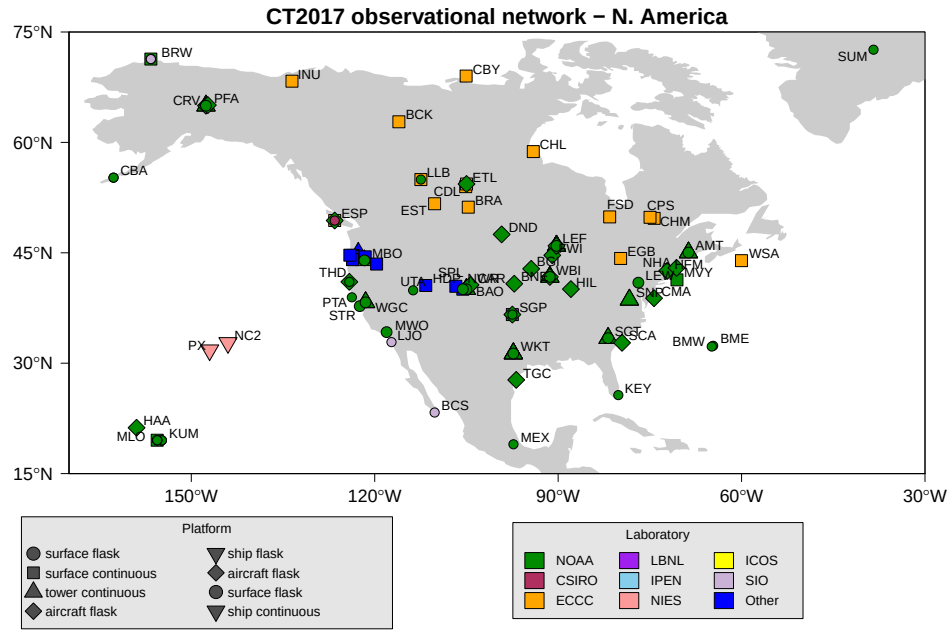

Figure 12: CarbonTracker observational network over North America. See the CarbonTracker interactive network map for more details.

sPack distribution, obs_flag. Only observations with obs_flag = 1 are identified for assimilation by data providers. We modify the designation of assimilation data for Environment and Climate Change Canada quasi-continuous sampling sites. For these data, obs_flag is set to 1 by the data provider for times when they represent the daily minimum CO_2 concentration. This is generally later in the day than our standard scheme of local noon-4pm used to represent times of well-mixed PBLs. For these datasets, we have changed obs_flag to indicate assimilation only for the local noon - 4pm time period. These selected observations are further filtered based on the CCG curve fitting routine of Thoning *et al.*(1989). This filter fits a smooth curve to the selected observations, and measurements more than 3 standard deviations away from this curve are excluded from assimilation.

At mountain-top sites (*e.g.* MLO, NWR, and SPL), it is usually nighttime hours that are selected for assimilation, as these tend to be the most stable time period. Nighttime hours also avoid periods of upslope flows that contain local vegetative and/or anthropogenic influence.

Data from the Sutro tower (STR) and the Boulder (Erie, Colorado) tower (BAO) are strongly influenced by local urban emissions, which CarbonTracker is unable to resolve. At these two sites, pollution events have been identified using co-located measurements of carbon monoxide. In this study, measurements thought to be affected by pollution events have been excluded. This technique is under active refinement.

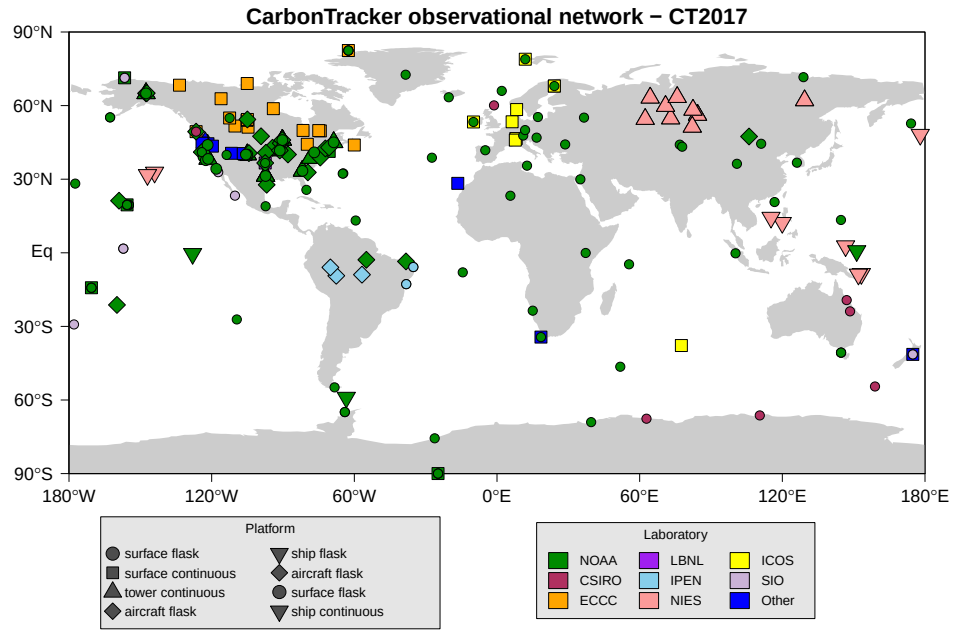

Figure 13: CarbonTracker global observational network. See the CarbonTracker interactive network map for more details.

With CT2017, we have begun to assimilate CO_2 measurements from NOAA light aircraft profiling time series, from intakes at multiple levels on NOAA tall towers, and from extensive shipboard and Siberian tower measurements collected by our partners at NIES. These datasets can be explored at the interactive data plotting page.

We apply a further selection criterion during the assimilation to exclude non-marine boundary layer (MBL) observations that are very poorly forecasted in our framework. We use the so-called model-data mismatch in this process, which is the random error ascribed to each observation to account for measurement errors as well as modeling errors of that observation. We interpret an observed-minus-forecasted mole fraction that exceeds 3 times the prescribed model-data mismatch as an indicator that our modeling framework fails. This can happen for instance when an air sample is representative of local exchange not captured well by our $1^\circ \times 1^\circ$ fluxes, when local meteorological conditions are not captured by our offline transport fields, but also when large-scale CO_2 exchange is suddenly changed (*e.g.* fires, pests, droughts) to an extent that can not be accommodated by our flux modules. This last situation would imply an important change in the carbon cycle and has to be recognized by the researchers when analyzing the results. In accordance with the 3-sigma rejection criterion, about 0.2% of the observations are discarded through this mechanism in our assimilations.

7.2 Adaptive model-data mismatch

The statistical optimization method we use to constrain surface CO_2 fluxes requires that each assimilation constraint is assigned a "model-data mismatch" (MDM) error value. This is meant to express the statistics of simulated-minus-observed CO_2 observations we could expect if CarbonTracker were using perfect surface fluxes. Such deviations arise from many sources, including random noise in the measurement system, *in situ* variability that we do not expect to resolve in our model, and faults with the atmospheric transport model. Generally, transport and inverse model faults are the dominant terms in MDM values. The MDM is one of two major "tuning knobs" used to adjust the performance of our ensemble Kalman filter. The other is also an error quantity, meant to represent the expected error on our first-guess fluxes. Discussion of this prior covariance error can be found in section 8.2.

Prior to CT2015, CarbonTracker used a single MDM value for each assimilation dataset. The NOAA continuous observations at the 396m level of the WLEF tower in northern Wisconsin, for example, were assigned a MDM of 3.0 ppm, meaning that the residuals between model-forecasted measurements and the actual observed concentrations are expected to be unbiased (*i.e.*, have a mean of zero) and have a standard deviation of 3 ppm. In practice, however, we have found that it is far easier to simulate wintertime observations than those during summer. This is mainly due to higher ambient variability of CO_2 in the summer.

Starting with CT2016, we began to use an empirical scheme to assign MDM values, exploiting statistics of model performance from indenpendently-configured preliminary inversions. The posterior residuals for each dataset are classified into relevant bins, and then statistics of model performance are analyzed within each of those bins. For every dataset, these bins include equally-spaced intervals of one-tenth of a year. For analyzers collecting data throughout the day, we also classify the measurements into 4-hour intervals of local time. For aircraft datasets, we further classify measurements into vertical levels of 1000m thickness (0-1000 m ASL, 1000-2000 m ASL, etc.). For each of these bins, bias and random error are combined to form total deviation from observed values as a root-mean square error (RMSE). The assigned MDM is set to a constant fraction of this total RMSE. This scaling is meant to force the assimilation scheme to extract as much information as possible from available observations. We use two different scaling factors to convert RMSE to MDM, depending on whether the preliminary inversions actually assimilated the measurements in the relevant bin, or merely simulated those measurements. For measurements assimilated by the preliminary inversions, the MDM is $0.95 * \text{RMSE}$; for measurements not assimilated in the preliminary inversions, the

MDM is 0.85 $*$ RMSE.

The adaptive MDM scheme performs well in terms of average χ^2, which in an optimally-tuned system should be close to 1.0 for each dataset (see Table 3). Notably, the seasonal variations of MDM successfully compensate for the higher ambient variability of CO_2 at continental sites during the growing season. It is, however, an iterative process, requiring that we conduct a previous inversion. For various reasons, this previous inversion performed before CT2017 differs in significant aspects from the actual CT2017 inversions. These differences have led to MDM values which are slightly too large and thus average χ^2 values which are generally smaller than the target of 1.0 (in some cases, as low as 0.2 or 0.3). The next iteration of CarbonTracker will be able to use the more recent CT2017 inversions to refine the adaptive MDM scheme.

Duplicate observations are identified as those within 50 minutes temporally, 10m vertically, and 0.05 degrees of latitude and longitude laterally (nominally, about 5km). The MDM for such observations is inflated by $\sqrt{n}$, where n is the number of duplicates.

7.3 Statistical performance of CT2017

Table 3 summarizes the datasets assimilated in CarbonTracker, and the performace of the assimilation scheme for each dataset. These diagnostics are useful for evaluating how well CarbonTracker does in simulating observed CO_2.

Dataset	Lab.	Location	Latitude	Longitude	Elev. (m)	Used	Rej.	R (ppm)	χ^2	Bias (ppm)	SE (ppm)
co2_abp_surface-flask_1_representative	NOAA	Arembepe, Bahia, Brazil	12.77°S	38.17°W	1	187	0	1.1 - 3.2	0.21	-0.57	1.09
co2_abp_surface-flask_26_marine	IPEN	Arembepe, Bahia, Brazil	12.77°S	38.17°W	1	196	0	0.9 - 6.4	0.37	-0.91	1.61
co2_acg_aircraft-pfp_1_allvalid_0-1000masl	NOAA	Alaska Coast Guard, United States			440	413	12	0.3 - 3.4	1.53	-0.33	2.63
co2_acg_aircraft-pfp_1_allvalid_1000 2000masl	NOAA	Alaska Coast Guard, United States			1490	233	3	0.3 - 3.4	1.05	0.20	1.80
co2_acg_aircraft-pfp_1_allvalid_2000-3000masl	NOAA	Alaska Coast Guard, United States			2533	146	1	0.6 - 3.4	0.94	0.19	1.53
co2_acg_aircraft-pfp_1_allvalid_3000 4000masl	NOAA	Alaska Coast Guard, United States			3530	131	2	0.7 - 3.4	0.85	0.30	1.45
co2_acg_aircraft-pfp_1_allvalid_4000-5000masl	NOAA	Alaska Coast Guard, United States			4424	119	0	0.3 - 3.4	0.94	0.02	1.40
co2_acg_aircraft-pfp_1_allvalid_5000 6000masl	NOAA	Alaska Coast Guard, United States			5494	126	1	0.3 - 3.4	0.80	0.18	1.39
co2_acg_aircraft-pfp_1_allvalid_6000-7000masl	NOAA	Alaska Coast Guard, United States			6443	130	2	0.3 - 3.4	0.84	0.22	1.46
co2_acg_aircraft-pfp_1_allvalid_7000 8000masl	NOAA	Alaska Coast Guard, United States			7495	136	5	0.3 - 3.4	0.61	0.08	1.43
co2_acg_aircraft-pfp_1_allvalid_8000-9000masl	NOAA	Alaska Coast Guard, United States			8342	18	0	0.9 - 2.2	0.90	0.73	0.65
co2_ah2_shipboard-insitu_20_allvalid	NIES	Alligator Hope (M/S Alligator Hope of Mitsui O.S.K. Lines, Ltd.), N/A	48.16°N	178.00°E	Surface	31243	566	1.0 - 34.5	0.87	-0.42	2.95

(table continued on next page)

Dataset	Lab.	Location	Latitude	Longitude	Elev. (m)	Used	Rej.	R (ppm)	χ^2	Bias (ppm)	SE (ppm)
co2_alf_aircraft-pfp_26_representative_0-1000masl	IPEN	Alta Floresta, Brazil	8.92°S	56.79°W	677	153	6	1.0 - 9.5	0.72	-0.82	4.76
co2_alf_aircraft-pfp_26_representati 2000masl	IPEN	Alta Floresta, Brazil	8.92°S	56.79°W	1526	167	6	0.7 - 4.7	1.09	-0.45	3.22
co2_alf_aircraft-pfp_26_representative_2000-3000masl	IPEN	Alta Floresta, Brazil	8.92°S	56.79°W	2379	102	4	0.7 - 3.1	1.00	-0.57	2.04
co2_alf_aircraft-pfp_26_representati 4000masl	IPEN	Alta Floresta, Brazil	8.92°S	56.79°W	3504	176	6	0.3 - 3.1	1.35	-0.33	1.61
co2_alf_aircraft-pfp_26_representative_4000-5000masl	IPEN	Alta Floresta, Brazil	8.92°S	56.79°W	4420	56	2	0.5 - 2.4	0.94	0.02	1.35
co2_alt_surface-flask_1_representati	NOAA	Alert, Nunavut, Canada	82.45°N	62.51°W	190	2557	4	0.3 - 9.4	0.39	-0.11	0.76
co2_alt_surface-flask_2_representative	CSIRO	Alert, Nunavut, Canada	82.45°N	62.51°W	190	902	13	0.1 - 3.2	1.03	-0.02	0.83
co2_alt_surface-flask_426_represent	SIO_CO2	Alert, Nunavut, Canada	82.45°N	62.51°W	190	583	2	0.2 - 111.9	0.33	-0.09	0.82
co2_alt_surface-flask_4_representative	SIO	Alert, Nunavut, Canada	82.45°N	62.51°W	190	376	2	0.3 - 5.1	0.80	0.07	0.75
co2_alt_surface-insitu_6_allvalid	EC	Alert, Nunavut, Canada	82.45°N	62.51°W	190	21161	246	0.5 - 5.4	1.28	-0.10	0.81
co2_ams_surface-insitu_11_representative	LSCE	Amsterdam Island, France	37.80°S	77.54°E	55	122509	4300	0.2 - 0.8	1.25	-0.09	0.57
co2_amt_surface-pfp_1_allvalid	NOAA	Argyle, Maine, United States	45.03°N	68.68°W	53	1615	0	1.6 - 21.6	0.23	0.34	3.79
co2_amt_tower-insitu_1_allvalid-107magl	NOAA	Argyle, Maine, United States	45.03°N	68.68°W	53	17438	129	2.0 - 11.9	0.63	0.24	3.88
co2_amt_tower-insitu_1_allvalid-12magl	NOAA	Argyle, Maine, United States	45.03°N	68.68°W	53	16221	173	1.7 - 6.7	0.88	0.51	4.20

(table continued on next page)

Dataset	Lab.	Location	Latitude	Longitude	Elev. (m)	Used	Rej.	R (ppm)	χ^2	Bias (ppm)	SE (ppm)
co2_amt_tower-insitu_1_allvalid-30magl	NOAA	Argyle, Maine, United States	45.03°N	68.68°W	53	10558	107	1.9 - 6.6	0.96	0.76	4.16
co2_ara_surface-flask_2_representati	CSIRO	Arcturus, Queensland, Australia	23.86°S	148.47°E	175	15	1	1.0 - 5.6	0.63	-0.83	3.21
co2_asc_surface-flask_1_representative	NOAA	Ascension Island, United Kingdom	7.97°S	14.40°W	85	2885	0	0.4 - 1.6	0.88	-0.02	0.67
co2_ask_surface-flask_1_representati	NOAA	Assekrem, Algeria	23.26°N	5.63°E	2710	1481	3	0.3 - 1.6	0.62	-0.20	0.61
co2_azr_surface-flask_1_representative	NOAA	Terceira Island, Azores, Portugal	38.77°N	27.38°W	19	908	0	0.3 - 3.7	0.57	0.22	1.41
co2_azv_tower-insitu_20_allvalid-29magl	NIES	Azovo, Russia	54.70°N	73.03°E	100	9817	28	2.5 - 8.0	0.50	-0.66	3.90
co2_azv_tower-insitu_20_allvalid-50magl	NIES	Azovo, Russia	54.70°N	73.03°E	100	9478	22	2.5 - 8.0	0.49	-0.49	3.84
co2_bal_surface-flask_1_representati	NOAA	Baltic Sea, Poland	55.35°N	17.22°E	3	1839	8	0.8 - 11.5	0.49	-1.48	5.40
co2_bao_surface-pfp_1_allvalid	NOAA	Boulder Atmospheric Observatory, Colorado, United States	40.05°N	105.00°W	1584	3135	2	1.2 - 64.2	0.26	-1.68	3.74
co2_bao_tower-insitu_1_allvalid-100magl	NOAA	Boulder Atmospheric Observatory, Colorado, United States	40.05°N	105.00°W	1584	10093	149	2.2 - 11.2	0.70	-2.59	5.14
co2_bao_tower-insitu_1_allvalid-22magl	NOAA	Boulder Atmospheric Observatory, Colorado, United States	40.05°N	105.00°W	1584	10205	161	2.3 - 14.4	0.71	-3.08	6.45
co2_bao_tower-insitu_1_allvalid-300magl	NOAA	Boulder Atmospheric Observatory, Colorado, United States	40.05°N	105.00°W	1584	65361	717	2.3 - 21.1	0.69	0.96	5.83
co2_bck_surface-insitu_6_allvalid	EC	Behchoko, Northwest Territories, Canada	62.80°N	116.05°W	179	7580	60	1.4 - 9.0	0.95	-0.11	3.91
co2_bcs_surface-flask_426_represent	SIO_CO2	Baja California Sur, Mexico	23.30°N	110.20°W	4	123	1	0.6 - 6.4	0.45	1.02	2.42

(table continued on next page)

Dataset	Lab.	Location	Latitude	Longitude	Elev. (m)	Used	Rej.	R (ppm)	χ^2	Bias (ppm)	SE (ppm)
co2_bgi_aircraft-pfp_1_allvalid_0-1000masl	NOAA	Bradgate, Iowa, United States	42.82°N	94.41°W	615	12	1	1.1 - 6.5	4.39	-0.36	6.73
co2_bgi_aircraft-pfp_1_allvalid_1000-2000masl	NOAA	Bradgate, Iowa, United States	42.82°N	94.41°W	1557	59	1	0.4 - 6.5	2.26	-0.65	3.55
co2_bgi_aircraft-pfp_1_allvalid_2000-3000masl	NOAA	Bradgate, Iowa, United States	42.82°N	94.41°W	2548	15	0	0.5 - 4.2	0.92	-0.35	1.37
co2_bgi_aircraft-pfp_1_allvalid_3000-4000masl	NOAA	Bradgate, Iowa, United States	42.82°N	94.41°W	3524	49	2	0.1 - 3.8	1.84	0.16	1.18
co2_bgi_aircraft-pfp_1_allvalid_4000-5000masl	NOAA	Bradgate, Iowa, United States	42.82°N	94.41°W	4569	25	0	0.2 - 1.1	1.11	0.10	0.81
co2_bgi_aircraft-pfp_1_allvalid_5000-6000masl	NOAA	Bradgate, Iowa, United States	42.82°N	94.41°W	5506	39	1	0.2 - 1.9	1.26	0.05	0.87
co2_bgi_aircraft-pfp_1_allvalid_6000-7000masl	NOAA	Bradgate, Iowa, United States	42.82°N	94.41°W	6474	37	0	0.3 - 3.4	1.26	0.14	0.98
co2_bgi_aircraft-pfp_1_allvalid_7000-8000masl	NOAA	Bradgate, Iowa, United States	42.82°N	94.41°W	7469	38	0	0.3 - 0.9	2.11	-0.02	0.64
co2_bgi_aircraft-pfp_1_allvalid_8000-9000masl	NOAA	Bradgate, Iowa, United States	42.82°N	94.41°W	8050	3	0	0.8 - 0.8	0.42	-0.14	0.98
co2_bhd_surface-flask_1_representati	NOAA	Baring Head Station, New Zealand	41.41°S	174.87°E	85	357	8	0.2 - 2.5	0.82	0.14	1.18
co2_bhd_surface-flask_426_representative	SIO_CO2	Baring Head Station, New Zealand	41.41°S	174.87°E	85	120	7	0.3 - 3.8	0.88	0.77	1.30
co2_bhd_surface-insitu_15_baseline	NIWA	Baring Head Station, New Zealand	41.41°S	174.87°E	85	492	32	0.3 - 3.5	1.24	0.40	1.15
co2_bir_surface-insitu_56_allvalid	NILU	Birkenes Observatory, Norway	58.39°N	8.25°E	219	1378	14	1.9 - 5.3	0.81	0.91	3.14

(table continued on next page)

Dataset	Lab.	Location	Latitude	Longitude	Elev. (m)	Used	Rej.	R (ppm)	χ^2	Bias (ppm)	SE (ppm)
co2_bkt_surface-flask_1_representati	NOAA	Bukit Kototabang, Indonesia	0.20°S	100.32°E	845	769	0	3.3 - 8.0	0.75	4.03	3.89
co2_bme_surface-flask_1_representative	NOAA	St. Davids Head, Bermuda, United Kingdom	32.37°N	64.65°W	12	454	1	0.9 - 3.9	0.60	0.48	1.53
co2_bmw_surface-flask_1_representati	NOAA	Tudor Hill, Bermuda, United Kingdom	32.26°N	64.88°W	30	1125	3	0.8 - 3.5	0.66	0.56	1.28
co2_bne_aircraft-pfp_1_allvalid_0-1000masl	NOAA	Beaver Crossing, Nebraska, United States	40.80°N	97.18°W	635	100	3	1.6 - 13.2	0.95	0.80	5.87
co2_bne_aircraft-pfp_1_allvalid_1000 2000masl	NOAA	Beaver Crossing, Nebraska, United States	40.80°N	97.18°W	1374	223	3	0.6 - 11.3	1.18	-0.13	3.49
co2_bne_aircraft-pfp_1_allvalid_2000-3000masl	NOAA	Beaver Crossing, Nebraska, United States	40.80°N	97.18°W	2293	117	0	0.3 - 13.0	0.91	-0.49	2.12
co2_bne_aircraft-pfp_1_allvalid_3000 4000masl	NOAA	Beaver Crossing, Nebraska, United States	40.80°N	97.18°W	3396	147	2	0.0 - 9.4	2.44	-0.21	1.80
co2_bne_aircraft-pfp_1_allvalid_4000-5000masl	NOAA	Beaver Crossing, Nebraska, United States	40.80°N	97.18°W	4278	84	0	0.5 - 12.0	1.02	-0.33	2.37
co2_bne_aircraft-pfp_1_allvalid_5000 6000masl	NOAA	Beaver Crossing, Nebraska, United States	40.80°N	97.18°W	5392	120	1	0.2 - 14.2	1.36	-0.19	2.25
co2_bne_aircraft-pfp_1_allvalid_6000-7000masl	NOAA	Beaver Crossing, Nebraska, United States	40.80°N	97.18°W	6362	113	0	0.3 - 14.8	1.21	-0.13	2.30
co2_bne_aircraft-pfp_1_allvalid_7000 8000masl	NOAA	Beaver Crossing, Nebraska, United States	40.80°N	97.18°W	7657	88	2	0.1 - 22.6	1.37	-0.14	3.75
co2_bne_aircraft-pfp_1_allvalid_8000-9000masl	NOAA	Beaver Crossing, Nebraska, United States	40.80°N	97.18°W	8072	27	1	0.5 - 1.2	1.05	-0.34	0.81
co2_bra_surface-insitu_6_allvalid	EC	Bratt's Lake Saskatchewan, Canada	51.20°N	104.70°W	595	8065	72	2.5 - 9.2	0.69	0.08	4.42

(table continued on next page)

Dataset	Lab.	Location	Latitude	Longitude	Elev. (m)	Used	Rej.	R (ppm)	χ^2	Bias (ppm)	SE (ppm)
co2_brw_surface-flask_1_representative	NOAA	Barrow, Alaska, United States	71.32°N	156.61°W	11	2796	16	0.4 - 9.7	0.53	-0.16	1.86
co2_brw_surface-flask_426_represent	SIO_CO2	Barrow, Alaska, United States	71.32°N	156.61°W	11	606	2	0.2 - 1552.5	0.46	0.03	1.92
co2_brw_surface-insitu_1_allvalid	NOAA	Barrow, Alaska, United States	71.32°N	156.61°W	11	15296	110	1.2 - 7.4	1.07	-0.08	1.93
co2_brz_aircraft-insitu_20_allvalid_01000masl	NIES	Berezorechka, Russia	56.15°N	84.33°E	626	33802	42	2.1 - 206.7	0.17	-0.65	3.43
co2_brz_aircraft-insitu_20_allvalid_1000-2000masl	NIES	Berezorechka, Russia	56.15°N	84.33°E	1501	44139	64	2.1 - 131.9	0.11	-0.68	2.85
co2_brz_aircraft-insitu_20_allvalid_23000masl	NIES	Berezorechka, Russia	56.15°N	84.33°E	2414	19697	38	2.1 - 141.8	0.08	-0.72	2.50
co2_brz_aircraft-insitu_20_allvalid_3000-4000masl	NIES	Berezorechka, Russia	56.15°N	84.33°E	3075	2477	0	2.3 - 93.7	0.07	-0.69	2.76
co2_brz_tower-insitu_20_allvalid-20magl	NIES	Berezorechka, Russia	56.15°N	84.33°E	150	12288	41	2.9 - 28.1	0.42	-0.30	3.96
co2_brz_tower-insitu_20_allvalid-40magl	NIES	Berezorechka, Russia	56.15°N	84.33°E	150	11866	41	2.9 - 27.8	0.42	-0.47	3.98
co2_brz_tower-insitu_20_allvalid-5magl	NIES	Berezorechka, Russia	56.15°N	84.33°E	150	12012	41	2.9 - 29.4	0.42	-0.41	3.96
co2_brz_tower-insitu_20_allvalid-80magl	NIES	Berezorechka, Russia	56.15°N	84.33°E	150	6838	29	2.3 - 27.5	0.51	-0.65	3.97
co2_bsc_surface-flask_1_representati	NOAA	Black Sea, Constanta, Romania	44.18°N	28.66°E	0	848	0	2.1 - 30.6	0.50	-5.28	8.47
co2_car_aircraft-pfp_1_allvalid_1000-2000masl	NOAA	Briggsdale, Colorado, United States	40.63°N	104.33°W	1798	21	3	1.2 - 3.4	1.15	-1.03	2.89

(table continued on next page)

Dataset	Lab.	Location	Latitude	Longitude	Elev. (m)	Used	Rej.	R (ppm)	χ^2	Bias (ppm)	SE (ppm)
co2_car_aircraft-pfp_1_allvalid_2000 3000masl	NOAA	Briggsdale, Colorado, United States	40.63°N	104.33°W	2436	855	15	0.2 - 7.4	0.82	0.41	2.43
co2_car_aircraft-pfp_1_allvalid_3000-4000masl	NOAA	Briggsdale, Colorado, United States	40.63°N	104.33°W	3456	1064	7	0.1 - 4.4	1.13	0.18	1.13
co2_car_aircraft-pfp_1_allvalid_4000 5000masl	NOAA	Briggsdale, Colorado, United States	40.63°N	104.33°W	4500	968	6	0.2 - 3.2	1.17	0.19	0.94
co2_car_aircraft-pfp_1_allvalid_5000-6000masl	NOAA	Briggsdale, Colorado, United States	40.63°N	104.33°W	5484	759	4	0.2 - 2.6	1.10	0.09	0.90
co2_car_aircraft-pfp_1_allvalid_6000 7000masl	NOAA	Briggsdale, Colorado, United States	40.63°N	104.33°W	6449	788	9	0.3 - 2.0	1.19	0.24	0.78
co2_car_aircraft-pfp_1_allvalid_7000-8000masl	NOAA	Briggsdale, Colorado, United States	40.63°N	104.33°W	7473	814	9	0.2 - 2.4	1.22	0.24	0.77
co2_car_aircraft-pfp_1_allvalid_8000 9000masl	NOAA	Briggsdale, Colorado, United States	40.63°N	104.33°W	8221	178	4	0.2 - 1.6	1.15	0.16	0.66
co2_car_aircraft-pfp_1_allvalid_9000-10000masl	NOAA	Briggsdale, Colorado, United States	40.63°N	104.33°W	9140	2	0	0.9 - 0.9	0.89	-0.51	0.85
co2_car_aircraft-pfp_1_allvalid_1100 12000masl	NOAA	Briggsdale, Colorado, United States	40.63°N	104.33°W	11869	4	0	0.3 - 0.5	1.59	-0.45	0.39
co2_cba_surface-flask_1_representative	NOAA	Cold Bay, Alaska, United States	55.21°N	162.72°W	21	2281	2	0.5 - 7.6	0.55	-0.78	1.74
co2_cba_surface-flask_4_representati	SIO	Cold Bay, Alaska, United States	55.21°N	162.72°W	21	333	5	0.3 - 7.4	1.04	-0.39	2.07
co2_cby_surface-insitu_6_allvalid	EC	Cambridge Bay, Nunavut Territory, Canada	69.01°N	105.05°W	35	5041	29	0.9 - 3.5	0.85	-0.12	1.96
co2_cdl_surface-insitu_6_allvalid	EC	Candle Lake, Saskatchewan, Canada	53.99°N	105.12°W	600	11049	50	1.7 - 7.1	0.76	-0.04	3.55

(table continued on next page)

Dataset	Lab.	Location	Latitude	Longitude	Elev. (m)	Used	Rej.	R (ppm)	χ^2	Bias (ppm)	SE (ppm)
co2_cfa_surface-flask_2_representative	CSIRO	Cape Ferguson, Queensland, Australia	19.28°S	147.06°E	2	587	6	0.1 - 3.1	0.51	-0.47	1.07
co2_cgo_surface-flask_1_representati	NOAA	Cape Grim, Tasmania, Australia	40.68°S	144.69°E	94	1063	0	0.3 - 3.4	0.58	0.04	0.75
co2_cgo_surface-flask_2_representative	CSIRO	Cape Grim, Tasmania, Australia	40.68°S	144.69°E	94	1191	10	0.2 - 5.0	0.53	-0.03	0.82
co2_cgo_surface-flask_4_representati	SIO	Cape Grim, Tasmania, Australia	40.68°S	144.69°E	94	325	14	0.2 - 2.6	1.15	0.26	0.96
co2_chl_surface-insitu_6_allvalid	EC	Churchill, Manitoba, Canada	58.75°N	94.07°W	29	5084	25	1.6 - 4.2	0.76	-0.19	3.04
co2_chm_surface-insitu_6_allvalid	EC	Chibougamau, Quebec, Canada	49.68°N	74.30°W	393	3985	35	2.4 - 4.5	0.87	0.05	3.19
co2_chr_surface-flask_1_representative	NOAA	Christmas Island, Republic of Kiribati	1.70°N	157.15°W	0	1023	0	0.3 - 2.3	0.66	-0.21	0.58
co2_chr_surface-flask_426_represent	SIO_CO2	Christmas Island, Republic of Kiribati	1.70°N	157.15°W	0	275	0	0.4 - 9.0	0.28	-0.37	0.79
co2_cib_surface-flask_1_representative	NOAA	Centro de Investigacion de la Baja Atmosfera (CIBA), Spain	41.81°N	4.93°W	845	663	2	2.2 - 10.0	0.51	0.16	3.43
co2_cma_aircraft-pfp_1_allvalid_0-1000masl	NOAA	Cape May, New Jersey, United States	38.83°N	74.32°W	613	527	16	0.2 - 8.4	0.95	-0.23	3.99
co2_cma_aircraft-pfp_1_allvalid_1000-2000masl	NOAA	Cape May, New Jersey, United States	38.83°N	74.32°W	1537	284	1	0.7 - 6.6	1.08	-0.59	2.56
co2_cma_aircraft-pfp_1_allvalid_2000 3000masl	NOAA	Cape May, New Jersey, United States	38.83°N	74.32°W	2295	319	15	0.4 - 5.9	1.15	-0.41	2.00
co2_cma_aircraft-pfp_1_allvalid_3000-4000masl	NOAA	Cape May, New Jersey, United States	38.83°N	74.32°W	3452	305	6	0.4 - 2.8	1.26	0.11	1.15
co2_cma_aircraft-pfp_1_allvalid_4000 5000masl	NOAA	Cape May, New Jersey, United States	38.83°N	74.32°W	4205	162	4	0.1 - 3.2	1.13	0.12	1.28

(table continued on next page)

Dataset	Lab.	Location	Latitude	Longitude	Elev. (m)	Used	Rej.	R (ppm)	χ^2	Bias (ppm)	SE (ppm)
co2_cma_aircraft-pfp_1_allvalid_5000-6000masl	NOAA	Cape May, New Jersey, United States	38.83°N	74.32°W	5350	289	12	0.2 - 1.8	1.43	0.18	0.97
co2_cma_aircraft-pfp_1_allvalid_6000 7000masl	NOAA	Cape May, New Jersey, United States	38.83°N	74.32°W	6266	234	8	0.1 - 1.6	1.31	0.05	0.94
co2_cma_aircraft-pfp_1_allvalid_7000-8000masl	NOAA	Cape May, New Jersey, United States	38.83°N	74.32°W	7719	229	10	0.2 - 2.1	1.30	0.31	0.91
co2_cma_aircraft-pfp_1_allvalid_8000 9000masl	NOAA	Cape May, New Jersey, United States	38.83°N	74.32°W	8046	24	1	0.4 - 1.8	1.02	0.55	0.83
co2_con_aircraft-flask_20_allvalid_3000-4000masl	NIES	-	34.48°N	140.35°E	3680	1	2	0.6 - 0.8	3.00	1.37	0.56
co2_con_aircraft-flask_20_allvalid_50 6000masl	NIES	-	34.48°N		5727	6	0	0.6 - 1.2	0.80	0.06	0.74
co2_con_aircraft-flask_20_allvalid_6000-7000masl	NIES	-			6478	4	1	0.6 - 1.4	0.64	0.78	1.51
co2_con_aircraft-flask_20_allvalid_70 8000masl	NIES	-			7940	2	0	0.5 - 0.6	0.08	0.08	0.08
co2_con_aircraft-flask_20_allvalid_8000-9000masl	NIES	-			8571	10	0	0.4 - 1.4	0.38	0.02	0.67
co2_con_aircraft-flask_20_allvalid_90 10000masl	NIES	-			9617	270	7	0.1 - 1.4	1.16	0.05	0.78
co2_con_aircraft-flask_20_allvalid_10000-11000masl	NIES	-			10702	1647	28	0.1 - 1.4	0.97	0.02	0.65
co2_con_aircraft-flask_20_allvalid_11 12000masl	NIES	-			11541	805	35	0.4 - 1.4	1.12	0.14	0.76

(table continued on next page)

Dataset	Lab.	Location	Latitude	Longitude	Elev. (m)	Used	Rej.	R (ppm)	χ^2	Bias (ppm)	SE (ppm)
co2_con_aircraft-flask_20_allvalid_12000-13000masl	NIES	-			12191	138	10	0.4 - 1.4	1.28	0.05	0.98
co2_cps_surface-insitu_6_allvalid	EC	Chapais,Quebec, Canada	49.82°N	74.98°W	381	7115	52	1.7 - 4.9	0.91	0.44	3.17
co2_cpt_surface-flask_1_representative	NOAA	Cape Point, South Africa	34.35°S	18.49°E	230	290	2	0.4 - 3.2	0.17	0.25	0.50
co2_cpt_surface-insitu_36_marine	SAWS	Cape Point, South Africa	34.35°S	18.49°E	230	112321	708	0.4 - 1.7	1.11	0.03	0.64
co2_crv_aircraft-pfp_1_allvalid_0-1000masl	NOAA	Carbon in Arctic Reservoirs Vulnerability Experiment (CARVE), United States	64.99°N	147.60°W	314	1395	32	0.8 - 26.8	0.94	-2.66	6.51
co2_crv_aircraft-pfp_1_allvalid_1000 2000masl	NOAA	Carbon in Arctic Reservoirs Vulnerability Experiment (CARVE), United States	64.99°N	147.60°W	1441	54	0	0.8 - 18.7	0.39	-0.52	3.03
co2_crv_aircraft-pfp_1_allvalid_2000-3000masl	NOAA	Carbon in Arctic Reservoirs Vulnerability Experiment (CARVE), United States	64.99°N	147.60°W	2665	59	0	0.5 - 23.6	0.28	0.15	1.57
co2_crv_aircraft-pfp_1_allvalid_3000 4000masl	NOAA	Carbon in Arctic Reservoirs Vulnerability Experiment (CARVE), United States	64.99°N	147.60°W	3387	58	0	1.2 - 23.6	0.12	0.42	1.30
co2_crv_aircraft-pfp_1_allvalid_4000-5000masl	NOAA	Carbon in Arctic Reservoirs Vulnerability Experiment (CARVE), United States	64.99°N	147.60°W	4527	35	0	0.5 - 23.6	0.31	0.58	1.26
co2_crv_aircraft-pfp_1_allvalid_5000 6000masl	NOAA	Carbon in Arctic Reservoirs Vulnerability Experiment (CARVE), United States	64.99°N	147.60°W	5264	292	0	0.8 - 23.6	0.13	0.35	1.38

(table continued on next page)

Dataset	Lab.	Location	Latitude	Longitude	Elev. (m)	Used	Rej.	R (ppm)	χ^2	Bias (ppm)	SE (ppm)
co2_crv_surface-pfp_1_allvalid	NOAA	Carbon in Arctic Reservoirs Vulnerability Experiment (CARVE), United States	64.99°N	147.60°W	611	904	3	2.0 - 12.9	0.53	-0.37	3.17
co2_crv_tower-insitu_1_allvalid-17magl	NOAA	Carbon in Arctic Reservoirs Vulnerability Experiment (CARVE), United States	64.99°N	147.60°W	611	6390	42	1.8 - 10.9	0.84	-0.04	4.41
co2_crv_tower-insitu_1_allvalid-32magl	NOAA	Carbon in Arctic Reservoirs Vulnerability Experiment (CARVE), United States	64.99°N	147.60°W	611	6791	25	1.7 - 23.0	0.77	-0.07	4.81
co2_crv_tower-insitu_1_allvalid-5magl	NOAA	Carbon in Arctic Reservoirs Vulnerability Experiment (CARVE), United States	64.99°N	147.60°W	611	6477	37	1.9 - 11.3	0.83	0.01	4.57
co2_crz_surface-flask_1_representative	NOAA	Crozet Island, France	46.43°S	51.85°E	197	1250	0	0.1 - 0.6	0.70	0.01	0.30
co2_cya_surface-flask_2_representati	CSIRO	Casey, Antarctica, Australia	66.28°S	110.52°E	47	548	0	0.1 - 0.8	0.91	-0.06	0.23
co2_dem_tower-insitu_20_allvalid-45magl	NIES	Demyanskoe, Russia	59.79°N	70.87°E	75	12693	31	2.5 - 11.6	0.43	-0.33	3.67
co2_dem_tower-insitu_20_allvalid-63magl	NIES	Demyanskoe, Russia	59.79°N	70.87°E	75	11998	23	2.6 - 11.6	0.44	-0.44	3.72
co2_dnd_aircraft-pfp_1_allvalid_0-1000masl	NOAA	Dahlen, North Dakota, United States	47.50°N	99.24°W	746	246	5	1.0 - 27.0	0.75	0.11	5.76
co2_dnd_aircraft-pfp_1_allvalid_1000 2000masl	NOAA	Dahlen, North Dakota, United States	47.50°N	99.24°W	1504	329	5	0.1 - 11.5	0.92	-0.39	3.26
co2_dnd_aircraft-pfp_1_allvalid_2000-3000masl	NOAA	Dahlen, North Dakota, United States	47.50°N	99.24°W	2470	365	1	0.3 - 5.4	0.86	-0.34	1.87

(table continued on next page)

Dataset	Lab.	Location	Latitude	Longitude	Elev. (m)	Used	Rej.	R (ppm)	χ^2	Bias (ppm)	SE (ppm)
co2_dnd_aircraft-pfp_1_allvalid_3000 4000masl	NOAA	Dahlen, North Dakota, United States	47.50°N	99.24°W	3530	273	3	0.3 - 3.6	1.25	-0.03	1.21
co2_dnd_aircraft-pfp_1_allvalid_4000-5000masl	NOAA	Dahlen, North Dakota, United States	47.50°N	99.24°W	4466	203	2	0.2 - 3.3	1.45	0.03	1.24
co2_dnd_aircraft-pfp_1_allvalid_5000 6000masl	NOAA	Dahlen, North Dakota, United States	47.50°N	99.24°W	5508	233	6	0.3 - 4.1	1.24	0.09	1.01
co2_dnd_aircraft-pfp_1_allvalid_6000-7000masl	NOAA	Dahlen, North Dakota, United States	47.50°N	99.24°W	6481	209	4	0.2 - 2.8	1.18	0.11	0.97
co2_dnd_aircraft-pfp_1_allvalid_7000 8000masl	NOAA	Dahlen, North Dakota, United States	47.50°N	99.24°W	7474	215	6	0.1 - 2.3	1.17	0.13	0.95
co2_dnd_aircraft-pfp_1_allvalid_8000-9000masl	NOAA	Dahlen, North Dakota, United States	47.50°N	99.24°W	8053	4	0	0.3 - 1.8	2.83	-1.16	0.98
co2_drp_shipboard-flask_1_representati	NOAA	Drake Passage, N/A	59.00°S	63.38°W	Surface	195	11	0.0 - 0.9	0.84	-0.01	0.33
co2_dsi_surface-flask_1_representative	NOAA	Dongsha Island, Taiwan	20.70°N	116.73°E	3	481	2	0.6 - 6.8	0.70	1.47	3.22
co2_egb_surface-insitu_6_allvalid	EC	Egbert, Ontario, Canada	44.23°N	79.78°W	251	15011	169	3.2 - 8.2	0.63	-0.78	5.07
co2_eic_surface-flask_1_representative	NOAA	Easter Island, Chile	27.16°S	109.43°W	47	1034	2	0.5 - 22.9	0.58	0.38	1.01
co2_esp_aircraft-pfp_1_allvalid_0-1000masl	NOAA	Estevan Point, British Columbia, Canada	49.38°N	126.54°W	521	611	10	0.2 - 8.9	0.76	-0.51	4.16
co2_esp_aircraft-pfp_1_allvalid_1000-2000masl	NOAA	Estevan Point, British Columbia, Canada	49.38°N	126.54°W	1520	834	11	0.4 - 3.4	1.00	-0.05	1.42
co2_esp_aircraft-pfp_1_allvalid_2000 3000masl	NOAA	Estevan Point, British Columbia, Canada	49.38°N	126.54°W	2547	665	9	0.3 - 2.5	1.17	0.03	1.27

(table continued on next page)

Dataset	Lab.	Location	Latitude	Longitude	Elev. (m)	Used	Rej.	R (ppm)	χ^2	Bias (ppm)	SE (ppm)
co2_esp_aircraft-pfp_1_allvalid_3000-4000masl	NOAA	Estevan Point, British Columbia, Canada	49.38°N	126.54°W	3547	651	9	0.2 - 2.8	1.27	0.15	1.15
co2_esp_aircraft-pfp_1_allvalid_4000 5000masl	NOAA	Estevan Point, British Columbia, Canada	49.38°N	126.54°W	4499	574	18	0.2 - 2.3	1.35	0.10	1.14
co2_esp_aircraft-pfp_1_allvalid_5000-6000masl	NOAA	Estevan Point, British Columbia, Canada	49.38°N	126.54°W	5394	364	13	0.3 - 2.6	1.23	-0.01	1.11
co2_esp_surface-flask_2_representati	CSIRO	Estevan Point, British Columbia, Canada	49.38°N	126.54°W	7	34	0	0.2 - 11.9	0.94	-1.10	2.18
co2_esp_surface-insitu_6_allvalid	EC	Estevan Point, British Columbia, Canada	49.38°N	126.54°W	7	10114	44	2.5 - 6.8	0.66	-0.25	4.49
co2_est_surface-insitu_6_allvalid	EC	Esther, Alberta, Canada	51.66°N	110.21°W	707	9649	64	2.2 - 5.9	0.67	0.38	3.62
co2_etl_aircraft-pfp_1_allvalid_0-1000masl	NOAA	East Trout Lake, Saskatchewan, Canada	54.35°N	104.98°W	909	195	1	0.8 - 5.1	1.25	-0.12	2.88
co2_etl_aircraft-pfp_1_allvalid_1000 2000masl	NOAA	East Trout Lake, Saskatchewan, Canada	54.35°N	104.98°W	1510	713	17	0.3 - 7.9	0.93	-0.25	2.24
co2_etl_aircraft-pfp_1_allvalid_2000-3000masl	NOAA	East Trout Lake, Saskatchewan, Canada	54.35°N	104.98°W	2482	763	9	0.2 - 8.7	1.03	-0.29	1.64
co2_etl_aircraft-pfp_1_allvalid_3000 4000masl	NOAA	East Trout Lake, Saskatchewan, Canada	54.35°N	104.98°W	3502	274	1	0.4 - 2.6	1.01	-0.02	1.41
co2_etl_aircraft-pfp_1_allvalid_4000-5000masl	NOAA	East Trout Lake, Saskatchewan, Canada	54.35°N	104.98°W	4590	270	4	0.5 - 5.5	1.10	0.10	1.46
co2_etl_aircraft-pfp_1_allvalid_5000 6000masl	NOAA	East Trout Lake, Saskatchewan, Canada	54.35°N	104.98°W	5643	246	4	0.5 - 2.4	1.03	0.18	1.23
co2_etl_aircraft-pfp_1_allvalid_6000-7000masl	NOAA	East Trout Lake, Saskatchewan, Canada	54.35°N	104.98°W	6746	131	5	0.4 - 2.0	1.14	0.46	0.99

(table continued on next page)

Dataset	Lab.	Location	Latitude	Longitude	Elev. (m)	Used	Rej.	R (ppm)	χ^2	Bias (ppm)	SE (ppm)
co2_etl_aircraft-pfp_1_allvalid_7000 8000masl	NOAA	East Trout Lake, Saskatchewan, Canada	54.35°N	104.98°W	7152	92	3	0.5 - 2.6	1.68	0.16	1.68
co2_etl_surface-insitu_6_allvalid	EC	East Trout Lake, Saskatchewan, Canada	54.35°N	104.98°W	492	15590	43	2.0 - 5.6	0.62	0.16	3.68
co2_fsd_surface-insitu_6_allvalid	EC	Fraserdale, Canada	49.88°N	81.57°W	210	21914	108	1.6 - 6.2	0.81	0.16	3.86
co2_ftl_aircraft-pfp_1_allvalid_0-1000masl	NOAA	Fortaleza, Brazil	3.52°S	38.28°W	539	42	0	1.3 - 3.5	0.73	-0.52	1.23
co2_ftl_aircraft-pfp_1_allvalid_1000 2000masl	NOAA	Fortaleza, Brazil	3.52°S	38.28°W	1579	36	0	0.5 - 1.7	1.41	0.11	0.94
co2_ftl_aircraft-pfp_1_allvalid_2000-3000masl	NOAA	Fortaleza, Brazil	3.52°S	38.28°W	2451	30	0	0.2 - 2.2	1.31	-0.33	1.16
co2_ftl_aircraft-pfp_1_allvalid_3000 4000masl	NOAA	Fortaleza, Brazil	3.52°S	38.28°W	3479	41	0	0.3 - 1.6	1.71	0.12	1.14
co2_ftl_aircraft-pfp_1_allvalid_4000-5000masl	NOAA	Fortaleza, Brazil	3.52°S	38.28°W	4267	8	0	0.3 - 1.9	2.71	0.48	1.37
co2_ftw_shipboard-insitu_20_allvalid	NIES	Fujitrans World (M/S Fujitrans World of Kagoshima Shipping Co., Ltd.), N/A	8.57°S	153.23°E	Surface	73859	1098	0.9 - 11.8	0.52	-0.22	1.60
co2_ftws_shipboard-insitu_20_allvalid	NIES	Fujitrans World - Southeast Asia Route (M/S Fujitrans World of Kagoshima Shipping Co., Ltd.), N/A	12.26°N	119.97°E	Surface	211007	1164	3.2 - 40.8	0.36	-0.81	2.98
co2_fwi_aircraft-pfp_1_allvalid_0-1000masl	NOAA	Fairchild, Wisconsin, United States	44.66°N	90.96°W	624	12	0	2.2 - 12.8	0.39	-3.01	6.76
co2_fwi_aircraft-pfp_1_allvalid_1000-2000masl	NOAA	Fairchild, Wisconsin, United States	44.66°N	90.96°W	1549	58	3	0.5 - 6.5	1.81	-0.65	2.97

(table continued on next page)

Dataset	Lab.	Location	Latitude	Longitude	Elev. (m)	Used	Rej.	R (ppm)	χ^2	Bias (ppm)	SE (ppm)
co2_fwi_aircraft-pfp_1_allvalid_2000 3000masl	NOAA	Fairchild, Wisconsin, United States	44.66°N	90.96°W	2535	17	1	0.4 - 2.8	2.04	-0.66	2.39
co2_fwi_aircraft-pfp_1_allvalid_3000-4000masl	NOAA	Fairchild, Wisconsin, United States	44.66°N	90.96°W	3518	57	2	0.3 - 5.2	1.08	-0.32	1.45
co2_fwi_aircraft-pfp_1_allvalid_4000 5000masl	NOAA	Fairchild, Wisconsin, United States	44.66°N	90.96°W	4570	30	1	0.1 - 1.9	1.84	0.18	0.94
co2_fwi_aircraft-pfp_1_allvalid_5000-6000masl	NOAA	Fairchild, Wisconsin, United States	44.66°N	90.96°W	5523	43	1	0.2 - 6.1	1.28	0.71	2.43
co2_fwi_aircraft-pfp_1_allvalid_6000 7000masl	NOAA	Fairchild, Wisconsin, United States	44.66°N	90.96°W	6504	35	3	0.1 - 1.6	1.88	0.26	1.01
co2_fwi_aircraft-pfp_1_allvalid_7000-8000masl	NOAA	Fairchild, Wisconsin, United States	44.66°N	90.96°W	7484	39	2	0.5 - 1.3	1.21	0.10	1.14
co2_gmi_surface-flask_1_representati	NOAA	Mariana Islands, Guam	13.39°N	144.66°E	0	1889	10	0.4 - 1.8	0.65	0.07	0.78
co2_gw_shipboard-insitu_20_allvalid	NIES	Golden Wattle (M/S Alligator Hope of Mitsui O.S.K. Lines, Ltd.), N/A	2.74°N	146.60°E	Surface	14139	326	0.4 - 33.6	0.55	-0.03	1.61
co2_haa_aircraft-pfp_1_allvalid_0-1000masl	NOAA	Molokai Island, Hawaii, United States	21.23°N	158.95°W	624	213	3	0.5 - 2.2	1.15	0.61	0.73
co2_haa_aircraft-pfp_1_allvalid_1000-2000masl	NOAA	Molokai Island, Hawaii, United States	21.23°N	158.95°W	1559	252	4	0.2 - 1.1	1.35	0.21	0.70
co2_haa_aircraft-pfp_1_allvalid_2000 3000masl	NOAA	Molokai Island, Hawaii, United States	21.23°N	158.95°W	2524	213	6	0.1 - 1.1	1.65	0.07	0.67
co2_haa_aircraft-pfp_1_allvalid_3000-4000masl	NOAA	Molokai Island, Hawaii, United States	21.23°N	158.95°W	3488	225	7	0.2 - 1.0	1.49	0.07	0.69

(table continued on next page)

Dataset	Lab.	Location	Latitude	Longitude	Elev. (m)	Used	Rej.	R (ppm)	χ^2	Bias (ppm)	SE (ppm)
co2_haa_aircraft-pfp_1_allvalid_4000 5000masl	NOAA	Molokai Island, Hawaii, United States	21.23°N	158.95°W	4532	262	7	0.1 - 1.0	1.34	0.11	0.75
co2_haa_aircraft-pfp_1_allvalid_5000-6000masl	NOAA	Molokai Island, Hawaii, United States	21.23°N	158.95°W	5440	200	5	0.3 - 0.9	1.44	0.16	0.71
co2_haa_aircraft-pfp_1_allvalid_6000 7000masl	NOAA	Molokai Island, Hawaii, United States	21.23°N	158.95°W	6490	211	5	0.2 - 1.3	1.29	0.26	0.92
co2_haa_aircraft-pfp_1_allvalid_7000-8000masl	NOAA	Molokai Island, Hawaii, United States	21.23°N	158.95°W	7471	115	7	0.3 - 1.8	0.85	0.36	1.22
co2_haa_aircraft-pfp_1_allvalid_8000 9000masl	NOAA	Molokai Island, Hawaii, United States	21.23°N	158.95°W	8041	63	0	0.3 - 2.7	0.83	-0.02	0.85
co2_hba_surface-flask_1_representative	NOAA	Halley Station, Antarctica, United Kingdom	75.61°S	26.21°W	30	1443	0	0.0 - 0.4	0.70	0.04	0.19
co2_hdp_surface-insitu_3_nonlocal	NCAR	Hidden Peak (Snowbird), Utah, United States	40.56°N	111.65°W	3351	59876	386	0.8 - 3.2	0.75	-0.37	1.25
co2_hfm_aircraft-pfp_1_allvalid_0-1000masl	NOAA	Harvard Forest, Massachusetts, United States	42.54°N	72.17°W	761	189	1	1.4 - 11.6	1.03	0.11	4.08
co2_hfm_aircraft-pfp_1_allvalid_1000 2000masl	NOAA	Harvard Forest, Massachusetts, United States	42.54°N	72.17°W	1527	288	6	0.9 - 8.4	1.09	-0.04	3.27
co2_hfm_aircraft-pfp_1_allvalid_2000-3000masl	NOAA	Harvard Forest, Massachusetts, United States	42.54°N	72.17°W	2452	192	3	0.4 - 7.5	1.39	-0.27	2.03
co2_hfm_aircraft-pfp_1_allvalid_3000 4000masl	NOAA	Harvard Forest, Massachusetts, United States	42.54°N	72.17°W	3432	162	5	0.4 - 6.9	1.51	0.19	1.27
co2_hfm_aircraft-pfp_1_allvalid_4000-5000masl	NOAA	Harvard Forest, Massachusetts, United States	42.54°N	72.17°W	4563	195	2	0.4 - 2.8	1.50	0.20	1.18

(table continued on next page)

Dataset	Lab.	Location	Latitude	Longitude	Elev. (m)	Used	Rej.	R (ppm)	χ^2	Bias (ppm)	SE (ppm)
co2_hfm_aircraft-pfp_1_allvalid_5000 6000masl	NOAA	Harvard Forest, Massachusetts, United States	42.54°N	72.17°W	5483	212	2	0.2 - 1.6	1.56	0.26	0.99
co2_hfm_aircraft-pfp_1_allvalid_6000-7000masl	NOAA	Harvard Forest, Massachusetts, United States	42.54°N	72.17°W	6426	156	0	0.3 - 2.1	1.67	0.42	1.00
co2_hfm_aircraft-pfp_1_allvalid_7000 8000masl	NOAA	Harvard Forest, Massachusetts, United States	42.54°N	72.17°W	7388	179	4	0.0 - 5.9	1.31	0.33	2.35
co2_hfm_aircraft-pfp_1_allvalid_8000-9000masl	NOAA	Harvard Forest, Massachusetts, United States	42.54°N	72.17°W	8031	2	0	1.3 - 1.3	1.76	-0.75	2.21
co2_hil_aircraft-pfp_1_allvalid_0-1000masl	NOAA	Homer, Illinois, United States	40.07°N	87.91°W	621	170	4	0.2 - 10.6	1.30	-0.02	4.54
co2_hil_aircraft-pfp_1_allvalid_1000-2000masl	NOAA	Homer, Illinois, United States	40.07°N	87.91°W	1539	362	5	0.7 - 6.4	1.15	-0.92	3.42
co2_hil_aircraft-pfp_1_allvalid_2000 3000masl	NOAA	Homer, Illinois, United States	40.07°N	87.91°W	2540	199	1	0.1 - 5.7	1.09	-0.77	1.99
co2_hil_aircraft-pfp_1_allvalid_3000-4000masl	NOAA	Homer, Illinois, United States	40.07°N	87.91°W	3502	347	2	0.3 - 4.5	1.20	-0.37	1.59
co2_hil_aircraft-pfp_1_allvalid_4000 5000masl	NOAA	Homer, Illinois, United States	40.07°N	87.91°W	4545	223	2	0.2 - 4.3	1.11	-0.25	1.32
co2_hil_aircraft-pfp_1_allvalid_5000-6000masl	NOAA	Homer, Illinois, United States	40.07°N	87.91°W	5516	289	5	0.1 - 4.2	0.96	-0.20	1.17
co2_hil_aircraft-pfp_1_allvalid_6000 7000masl	NOAA	Homer, Illinois, United States	40.07°N	87.91°W	6521	254	2	0.2 - 3.3	1.12	-0.10	1.19
co2_hil_aircraft-pfp_1_allvalid_7000-8000masl	NOAA	Homer, Illinois, United States	40.07°N	87.91°W	7485	269	3	0.3 - 2.7	1.03	-0.12	1.14

(table continued on next page)

Dataset	Lab.	Location	Latitude	Longitude	Elev. (m)	Used	Rej.	R (ppm)	χ^2	Bias (ppm)	SE (ppm)
co2_hil_aircraft-pfp_1_allvalid_8000 9000masl	NOAA	Homer, Illinois, United States	40.07°N	87.91°W	8040	24	0	0.5 - 4.0	1.35	-0.96	1.77
co2_hpb_surface-flask_1_representative	NOAA	Hohenpeissenberg, Germany	47.80°N	11.02°E	936	945	0	4.2 - 11.5	0.56	1.37	5.68
co2_hun_surface-flask_1_representati	NOAA	Hegyhatsal, Hungary	46.95°N	16.65°E	248	1591	4	2.3 - 15.4	0.36	-1.93	6.45
co2_ice_surface-flask_1_representative	NOAA	Storhofdi, Vestmannaeyjar, Iceland	63.40°N	20.29°W	118	851	12	0.3 - 2.5	0.77	-0.37	1.08
co2_igr_tower-insitu_20_allvalid-24magl	NIES	Igrim, Russia	63.19°N	64.42°E	25	11418	69	3.6 - 11.2	0.49	-1.80	4.79
co2_igr_tower-insitu_20_allvalid-47magl	NIES	Igrim, Russia	63.19°N	64.42°E	25	11199	144	4.3 - 11.5	0.41	-1.68	6.18
co2_inu_surface-insitu_6_allvalid	EC	Inuvik,Northwest Territories, Canada	68.32°N	133.53°W	113	7065	31	2.5 - 5.0	0.80	0.15	3.66
co2_inx_aircraft-pfp_1_allvalid_0-1000masl	NOAA	INFLUX (Indianapolis Flux Experiment), United States			679	226	2	1.9 - 12.7	2.02	-0.71	5.58
co2_inx_aircraft-pfp_1_allvalid_1000 2000masl	NOAA	INFLUX (Indianapolis Flux Experiment), United States			1332	67	0	1.9 - 6.7	1.02	0.11	4.22
co2_inx_aircraft-pfp_1_allvalid_2000-3000masl	NOAA	INFLUX (Indianapolis Flux Experiment), United States			2501	23	0	1.9 - 4.6	0.47	0.51	1.24
co2_inx_aircraft-pfp_1_allvalid_3000 4000masl	NOAA	INFLUX (Indianapolis Flux Experiment), United States			3226	12	0	1.9 - 10.9	0.10	0.14	0.88
co2_inx_surface-pfp_1_allvalid	NOAA	INFLUX (Indianapolis Flux Experiment), United States			356	1757	23	0.9 - 134.9	1.01	-1.08	6.41
co2_izo_surface-insitu_27_allvalid	AEMET	Izana, Tenerife, Canary Islands, Spain	28.31°N	16.50°W	2373	63999	1387	0.5 - 0.9	1.20	0.03	0.73
co2_jfj_surface-insitu_49_allvalid	KUP	Jungfraujoch, Switzerland	46.55°N	7.99°E	3570	14362	265	1.4 - 3.9	0.72	-0.07	2.02

(table continued on next page)

Dataset	Lab.	Location	Latitude	Longitude	Elev. (m)	Used	Rej.	R (ppm)	χ^2	Bias (ppm)	SE (ppm)
co2_jfj_surface-insitu_5_allvalid	EMPA	Jungfraujoch, Switzerland	46.55°N	7.99°E	3570	7865	92	1.4 - 3.8	0.58	0.08	1.91
co2_key_surface-flask_1_representative	NOAA	Key Biscayne, Florida, United States	25.67°N	80.16°W	1	1129	9	1.6 - 5.6	0.33	0.28	2.43
co2_krs_tower-insitu_20_allvalid-35magl	NIES	Karasevoe, Russia	58.25°N	82.42°E	50	12745	9	2.4 - 10.6	0.41	-0.17	3.96
co2_krs_tower-insitu_20_allvalid-67magl	NIES	Karasevoe, Russia	58.25°N	82.42°E	50	12046	9	2.4 - 10.7	0.41	-0.29	3.92
co2_kum_surface-flask_1_representati	NOAA	Cape Kumukahi, Hawaii, United States	19.52°N	154.82°W	3	3686	2	0.4 - 6.5	0.24	-0.22	0.98
co2_kum_surface-flask_426_representative	SIO_CO2	Cape Kumukahi, Hawaii, United States	19.52°N	154.82°W	3	663	1	0.2 - 16.6	0.49	-0.08	0.94
co2_kum_surface-flask_4_representati	SIO	Cape Kumukahi, Hawaii, United States	19.52°N	154.82°W	3	555	4	0.2 - 7.4	0.32	-0.12	1.04
co2_kzd_surface-flask_1_representative	NOAA	Sary Taukum, Kazakhstan	44.08°N	76.87°E	595	856	2	0.9 - 9.2	0.52	-1.40	4.15
co2_kzm_surface-flask_1_representati	NOAA	Plateau Assy, Kazakhstan	43.25°N	77.88°E	2519	766	0	1.4 - 6.9	0.62	-0.29	2.61
co2_lef_aircraft-pfp_1_allvalid_0-1000masl	NOAA	Park Falls, Wisconsin, United States	45.95°N	90.27°W	771	634	2	0.4 - 7.8	1.18	-0.14	4.31
co2_lef_aircraft-pfp_1_allvalid_1000 2000masl	NOAA	Park Falls, Wisconsin, United States	45.95°N	90.27°W	1514	1068	13	0.4 - 5.6	1.07	-0.26	3.29
co2_lef_aircraft-pfp_1_allvalid_2000-3000masl	NOAA	Park Falls, Wisconsin, United States	45.95°N	90.27°W	2465	784	12	0.4 - 4.5	0.90	-0.35	2.25
co2_lef_aircraft-pfp_1_allvalid_3000 4000masl	NOAA	Park Falls, Wisconsin, United States	45.95°N	90.27°W	3500	890	12	0.2 - 3.5	1.02	-0.10	1.59
co2_lef_aircraft-pfp_1_allvalid_4000-5000masl	NOAA	Park Falls, Wisconsin, United States	45.95°N	90.27°W	4010	3	0	2.3 - 2.3	0.51	-0.76	2.08

(table continued on next page)

Dataset	Lab.	Location	Latitude	Longitude	Elev. (m)	Used	Rej.	R (ppm)	χ^2	Bias (ppm)	SE (ppm)
co2_lef_surface-pfp_1_allvalid	NOAA	Park Falls, Wisconsin, United States	45.95°N	90.27°W	472	3551	5	1.6 - 25.3	0.36	-0.33	3.84
co2_lef_tower-insitu_1_allvalid-11magl	NOAA	Park Falls, Wisconsin, United States	45.95°N	90.27°W	472	11342	61	2.1 - 7.5	0.94	0.20	3.96
co2_lef_tower-insitu_1_allvalid-122magl	NOAA	Park Falls, Wisconsin, United States	45.95°N	90.27°W	472	22045	147	2.0 - 6.8	0.98	0.08	3.95
co2_lef_tower-insitu_1_allvalid-244magl	NOAA	Park Falls, Wisconsin, United States	45.95°N	90.27°W	472	67861	528	1.8 - 15.4	0.88	-0.13	4.03
co2_lef_tower-insitu_1_allvalid-30magl	NOAA	Park Falls, Wisconsin, United States	45.95°N	90.27°W	472	21966	149	2.1 - 7.4	0.96	0.19	4.20
co2_lef_tower-insitu_1_allvalid-396magl	NOAA	Park Falls, Wisconsin, United States	45.95°N	90.27°W	472	131715	1314	1.9 - 11.5	0.94	-0.08	3.74
co2_lef_tower-insitu_1_allvalid-76magl	NOAA	Park Falls, Wisconsin, United States	45.95°N	90.27°W	472	11285	54	1.9 - 7.4	1.01	-0.05	3.88
co2_lew_surface-pfp_1_allvalid	NOAA	Lewisburg, Pennsylvania, United States	40.94°N	76.88°W	161	354	13	2.6 - 16.5	0.92	-1.50	6.79
co2_ljo_surface-flask_426_represent	SIO_CO2	La Jolla, California, United States	32.87°N	117.26°W	10	381	17	1.0 - 10.6	0.97	2.74	3.30
co2_llb_surface-flask_1_representative	NOAA	Lac La Biche, Alberta, Canada	54.95°N	112.45°W	540	301	0	3.7 - 29.4	0.27	-0.35	4.67
co2_llb_surface-insitu_6_allvalid	EC	Lac La Biche, Alberta, Canada	54.95°N	112.45°W	540	12153	78	2.7 - 14.0	0.60	-0.01	4.79
co2_lmp_surface-flask_1_representative	NOAA	Lampedusa, Italy	35.52°N	12.62°E	45	847	1	0.9 - 4.2	0.53	-0.13	1.84
co2_lut_surface-insitu_44_allvalid	RUG	Lutjewad, Netherlands	53.40°N	6.35°E	1	11234	267	4.2 - 13.8	0.69	-1.18	6.12
co2_maa_surface-flask_2_representative	CSIRO	Mawson Station, Antarctica, Australia	67.62°S	62.87°E	32	615	0	0.1 - 1.2	0.72	-0.06	0.23
co2_mbo_surface-pfp_1_allvalid	NOAA	Mt. Bachelor Observatory, United States	43.98°N	121.69°W	2731	843	19	0.5 - 9.0	1.02	-0.36	1.62

(table continued on next page)

Dataset	Lab.	Location	Latitude	Longitude	Elev. (m)	Used	Rej.	R (ppm)	χ^2	Bias (ppm)	SE (ppm)
co2_mbo_tower-insitu_1_allvalid-11magl	NOAA	Mt. Bachelor Observatory, United States	43.98°N	121.69°W	2731	3619	45	0.9 - 10.3	1.06	0.60	3.41
co2_mex_surface-flask_1_representati	NOAA	High Altitude Global Climate Observation Center, Mexico	18.98°N	97.31°W	4464	595	2	0.7 - 4.2	0.64	0.76	1.47
co2_mhd_surface-flask_1_representative	NOAA	Mace Head, County Galway, Ireland	53.33°N	9.90°W	5	1334	4	0.5 - 8.4	0.38	-0.19	1.19
co2_mhd_surface-insitu_11_representa	LSCE	Mace Head, County Galway, Ireland	53.33°N	9.90°W	5	35180	355	0.6 - 3.3	1.06	0.04	0.91
co2_mid_surface-flask_1_representative	NOAA	Sand Island, Midway, United States	28.21°N	177.38°W	11	1451	2	0.4 - 2.7	0.64	0.39	1.00
co2_mkn_surface-flask_1_representati	NOAA	Mt. Kenya, Kenya	0.06°S	37.30°E	3644	266	0	0.9 - 4.9	0.55	1.65	2.00
co2_mlo_surface-flask_1_representative	NOAA	Mauna Loa, Hawaii, United States	19.54°N	155.58°W	3397	3384	5	0.4 - 2.5	0.70	0.06	0.52
co2_mlo_surface-flask_2_representati	CSIRO	Mauna Loa, Hawaii, United States	19.54°N	155.58°W	3397	806	0	0.4 - 3.4	0.56	0.11	0.56
co2_mlo_surface-flask_426_representative	SIO_CO2	Mauna Loa, Hawaii, United States	19.54°N	155.58°W	3397	820	16	0.3 - 1.8	1.43	0.14	0.53
co2_mlo_surface-flask_4_representati	SIO	Mauna Loa, Hawaii, United States	19.54°N	155.58°W	3397	592	15	0.1 - 44.5	0.73	0.20	0.57
co2_mlo_surface-insitu_1_allvalid	NOAA	Mauna Loa, Hawaii, United States	19.54°N	155.58°W	3397	17223	0	0.3 - 0.6	2.00	0.09	0.49
co2_mqa_surface-flask_2_representati	CSIRO	Macquarie Island, Australia	54.48°S	158.97°E	6	693	0	0.1 - 0.9	0.70	-0.00	0.38
co2_mvy_surface-insitu_1_allvalid	NOAA	Marthas Vineyard, Massachusetts, United States	41.33°N	70.57°W	0	63987	0	2.7 - 9.1	1.03	-0.17	4.61
co2_mwo_surface-pfp_1_allvalid	NOAA	Mt. Wilson Observatory, United States	34.22°N	118.06°W	1728	2519	79	0.7 - 14.6	0.74	-2.77	5.21
co2_nat_surface-flask_1_representative	NOAA	Farol De Mae Luiza Lighthouse, Brazil	5.80°S	35.19°W	50	471	2	1.0 - 2.4	0.57	-0.73	1.00
co2_nat_surface-flask_26_marine	IPEN	Farol De Mae Luiza Lighthouse, Brazil	5.80°S	35.19°W	50	396	2	1.1 - 2.6	0.62	-0.73	1.24

(table continued on next page)

Dataset	Lab.	Location	Latitude	Longitude	Elev. (m)	Used	Rej.	R (ppm)	χ^2	Bias (ppm)	SE (ppm)
co2_nc2_shipboard-insitu_20_allvalid	NIES	M/S New Century 2 (M/S New Century 2 of Kagoshima Shipping Co., Ltd.), N/A	32.76°N	144.00°W	Surface	50878	594	0.7 - 20.0	0.60	0.06	2.27
co2_nha_aircraft-pfp_1_allvalid_0-1000masl	NOAA	Worcester, Massachusetts, United States	42.95°N	70.63°W	604	724	5	1.2 - 7.0	1.09	0.22	3.14
co2_nha_aircraft-pfp_1_allvalid_1000-2000masl	NOAA	Worcester, Massachusetts, United States	42.95°N	70.63°W	1485	553	9	0.7 - 6.4	1.19	-0.23	2.41
co2_nha_aircraft-pfp_1_allvalid_2000 3000masl	NOAA	Worcester, Massachusetts, United States	42.95°N	70.63°W	2415	499	18	0.4 - 6.0	1.13	-0.33	2.10
co2_nha_aircraft-pfp_1_allvalid_3000-4000masl	NOAA	Worcester, Massachusetts, United States	42.95°N	70.63°W	3479	423	9	0.3 - 3.4	1.30	0.01	1.47
co2_nha_aircraft-pfp_1_allvalid_4000 5000masl	NOAA	Worcester, Massachusetts, United States	42.95°N	70.63°W	4432	260	5	0.3 - 2.4	1.40	0.04	1.10
co2_nha_aircraft-pfp_1_allvalid_5000-6000masl	NOAA	Worcester, Massachusetts, United States	42.95°N	70.63°W	5380	296	8	0.4 - 3.0	1.23	-0.07	1.34
co2_nha_aircraft-pfp_1_allvalid_6000 7000masl	NOAA	Worcester, Massachusetts, United States	42.95°N	70.63°W	6327	210	3	0.4 - 3.5	1.25	-0.06	1.57
co2_nha_aircraft-pfp_1_allvalid_7000-8000masl	NOAA	Worcester, Massachusetts, United States	42.95°N	70.63°W	7657	227	5	0.4 - 2.0	1.40	0.22	1.06
co2_nha_aircraft-pfp_1_allvalid_8000 9000masl	NOAA	Worcester, Massachusetts, United States	42.95°N	70.63°W	8043	3	1	0.1 - 1.1	0.01	-0.03	0.64
co2_nmb_surface-flask_1_representative	NOAA	Gobabeb, Namibia	23.58°S	15.03°E	456	688	2	0.4 - 2.5	0.54	-0.15	1.03
co2_noy_tower-insitu_20_allvalid-21magl	NIES	Noyabrsk, Russia	63.43°N	75.78°E	100	8443	11	2.2 - 14.4	0.37	-0.29	3.90

(table continued on next page)

Dataset	Lab.	Location	Latitude	Longitude	Elev. (m)	Used	Rej.	R (ppm)	χ^2	Bias (ppm)	SE (ppm)
co2_noy_tower-insitu_20_allvalid-43magl	NIES	Noyabrsk, Russia	63.43°N	75.78°E	100	8818	11	2.2 - 14.5	0.39	-0.38	3.87
co2_nwr_surface-flask_1_representati	NOAA	Niwot Ridge, Colorado, United States	40.05°N	105.59°W	3523	2046	0	0.3 - 21.5	0.27	0.30	1.34
co2_nwr_surface-insitu_3_nonlocal	NCAR	Niwot Ridge, Colorado, United States	40.05°N	105.59°W	3523	67692	783	0.9 - 6.0	0.76	-0.05	1.46
co2_nwr_surface-pfp_1_allvalid	NOAA	Niwot Ridge, Colorado, United States	40.05°N	105.59°W	3523	2345	25	0.4 - 18.1	0.55	0.33	1.81
co2_obn_surface-flask_1_representative	NOAA	Obninsk, Russia	55.11°N	36.60°E	183	228	2	1.7 - 13.1	0.62	-1.07	6.34
co2_ofr_surface-insitu_68_allhours	OSU	Fir, Oregon, United States	44.65°N	123.55°W	263	58180	13	4.7 - 74.5	0.17	-0.59	8.43
co2_omp_surface-insitu_68_allhours	OSU	Marys Peak, Oregon, United States	44.50°N	123.55°W	1249	88430	462	1.1 - 19.9	0.54	0.81	3.06
co2_omt_surface-insitu_68_allhours	OSU	Metolius, Oregon, United States	44.45°N	121.56°W	1255	78782	291	2.6 - 19.3	0.41	-0.10	4.05
co2_ong_surface-insitu_68_allhours	OSU	Burns, Oregon, United States	43.47°N	119.69°W	1398	80211	56	1.7 - 42.5	0.26	0.01	4.00
co2_osi_tower-insitu_68_allhours	OSU	Silverton, Oregon, United States	45.00°N	122.69°W	351	28781	130	4.2 - 18.4	0.70	0.70	7.02
co2_owa_surface-insitu_68_allhours	OSU	Walton, Oregon, United States	44.07°N	123.63°W	715	31083	212	2.1 - 7.8	0.94	-1.17	3.71
co2_oxk_surface-flask_1_representati	NOAA	Ochsenkopf, Germany	50.03°N	11.81°E	1022	788	0	2.7 - 9.7	0.53	-1.02	4.08
co2_oyq_surface-insitu_68_allhours	OSU	Yaquina Head, Oregon, United States	44.67°N	124.07°W	116	35230	19	1.6 - 34.4	0.23	-1.20	4.77
co2_pal_surface-flask_1_representati	NOAA	Pallas-Sammaltunturi, GAW Station, Finland	67.97°N	24.12°E	565	1254	2	1.3 - 28.7	0.31	-0.34	2.86
co2_pal_surface-insitu_30_marine	FMI	Pallas-Sammaltunturi, GAW Station, Finland	67.97°N	24.12°E	565	23660	27	1.0 - 5.1	0.53	-0.05	1.35
co2_pal_surface-insitu_30_nonlocal	FMI	Pallas-Sammaltunturi, GAW Station, Finland	67.97°N	24.12°E	565	95742	178	1.9 - 12.0	0.49	-0.14	2.40
co2_pfa_aircraft-pfp_1_allvalid_0-1000masl	NOAA	Poker Flat, Alaska, United States	65.07°N	147.29°W	549	364	2	1.1 - 10.2	1.26	-0.65	3.79

(table continued on next page)

Dataset	Lab.	Location	Latitude	Longitude	Elev. (m)	Used	Rej.	R (ppm)	χ^2	Bias (ppm)	SE (ppm)
co2_pfa_aircraft-pfp_1_allvalid_1000 2000masl	NOAA	Poker Flat, Alaska, United States	65.07°N	147.29°W	1502	476	2	0.8 - 6.6	0.76	-0.32	1.85
co2_pfa_aircraft-pfp_1_allvalid_2000-3000masl	NOAA	Poker Flat, Alaska, United States	65.07°N	147.29°W	2505	592	1	0.7 - 3.7	0.93	-0.35	1.31
co2_pfa_aircraft-pfp_1_allvalid_3000 4000masl	NOAA	Poker Flat, Alaska, United States	65.07°N	147.29°W	3476	598	5	0.6 - 2.7	0.95	-0.09	1.20
co2_pfa_aircraft-pfp_1_allvalid_4000-5000masl	NOAA	Poker Flat, Alaska, United States	65.07°N	147.29°W	4511	558	8	0.3 - 3.1	1.07	0.03	1.02
co2_pfa_aircraft-pfp_1_allvalid_5000 6000masl	NOAA	Poker Flat, Alaska, United States	65.07°N	147.29°W	5446	480	11	0.2 - 3.2	1.14	0.02	1.13
co2_pfa_aircraft-pfp_1_allvalid_6000-7000masl	NOAA	Poker Flat, Alaska, United States	65.07°N	147.29°W	6452	455	8	0.4 - 3.1	1.09	0.16	1.22
co2_pfa_aircraft-pfp_1_allvalid_7000 8000masl	NOAA	Poker Flat, Alaska, United States	65.07°N	147.29°W	7203	180	6	0.2 - 2.7	1.14	0.09	1.48
co2_poc_shipboard-flask_1_representative	NOAA	Pacific Ocean, N/A	0.41°S	128.00°W	Surface	2400	68	0.4 - 1.4	0.82	-0.06	0.76
co2_prs_surface-insitu_21_allvalid	RSE	Plateau Rosa Station, Italy	45.93°N	7.70°E	3480	10326	254	1.2 - 2.2	1.02	0.02	1.60
co2_psa_surface-flask_1_representative	NOAA	Palmer Station, Antarctica, United States	64.92°S	64.00°W	10	1576	0	0.1 - 1.1	0.52	-0.08	0.27
co2_psa_surface-flask_4_representati	SIO	Palmer Station, Antarctica, United States	64.92°S	64.00°W	10	352	19	0.1 - 0.9	0.90	0.08	0.27
co2_pta_surface-flask_1_representative	NOAA	Point Arena, California, United States	38.95°N	123.74°W	17	767	6	0.7 - 15.5	0.44	-1.60	5.67
co2_px_shipboard-insitu_20_allvalid	NIES	Pyxis (M/S Pyxis of Toyofuji Shipping Co., Ltd.), N/A	31.77°N	147.00°W	Surface	349456	3864	1.1 - 31.9	0.57	0.02	1.51

(table continued on next page)

Dataset	Lab.	Location	Latitude	Longitude	Elev. (m)	Used	Rej.	R (ppm)	χ^2	Bias (ppm)	SE (ppm)
co2_rba-b_aircraft-pfp_26_representative_0-1000masl	IPEN	Rio Branco, Brazil	9.36°S	67.60°W	616	155	0	3.4 - 13.5	0.95	-0.76	6.96
co2_rba-b_aircraft-pfp_26_representati 2000masl	IPEN	Rio Branco, Brazil	9.36°S	67.60°W	1524	176	1	1.0 - 7.2	0.73	-0.73	3.68
co2_rba-b_aircraft-pfp_26_representative_2000-3000masl	IPEN	Rio Branco, Brazil	9.36°S	67.60°W	2368	108	1	0.3 - 4.1	0.77	-0.51	2.23
co2_rba-b_aircraft-pfp_26_representati 4000masl	IPEN	Rio Branco, Brazil	9.36°S	67.60°W	3501	169	3	0.5 - 2.1	1.08	-0.39	1.21
co2_rba-b_aircraft-pfp_26_representative_4000-5000masl	IPEN	Rio Branco, Brazil	9.36°S	67.60°W	4420	52	1	0.6 - 3.4	0.85	-0.41	0.99
co2_rk1_surface-flask_426_represent	SIO_CO2	Kermadec Island, Raoul Island	29.20°S	177.90°W	2	84	0	0.1 - 1.5	0.76	-0.17	0.69
co2_rpb_surface-flask_1_representative	NOAA	Ragged Point, Barbados	13.16°N	59.43°W	15	1575	6	0.3 - 1.7	0.67	0.01	0.61
co2_rta_aircraft-pfp_1_allvalid_0-1000masl	NOAA	Rarotonga, Cook Islands	21.25°S	159.83°W	612	441	9	0.1 - 1.4	1.26	0.44	0.64
co2_rta_aircraft-pfp_1_allvalid_1000-2000masl	NOAA	Rarotonga, Cook Islands	21.25°S	159.83°W	1591	412	7	0.1 - 0.8	1.33	0.04	0.50
co2_rta_aircraft-pfp_1_allvalid_2000 3000masl	NOAA	Rarotonga, Cook Islands	21.25°S	159.83°W	2546	315	3	0.2 - 0.9	1.11	-0.10	0.48
co2_rta_aircraft-pfp_1_allvalid_3000-4000masl	NOAA	Rarotonga, Cook Islands	21.25°S	159.83°W	3487	379	6	0.1 - 1.1	1.20	-0.14	0.55

(table continued on next page)

Dataset	Lab.	Location	Latitude	Longitude	Elev. (m)	Used	Rej.	R (ppm)	χ^2	Bias (ppm)	SE (ppm)
co2_rta_aircraft-pfp_1_allvalid_4000 5000masl	NOAA	Rarotonga, Cook Islands	21.25°S	159.83°W	4556	310	5	0.2 - 1.2	1.19	0.03	0.52
co2_rta_aircraft-pfp_1_allvalid_5000-6000masl	NOAA	Rarotonga, Cook Islands	21.25°S	159.83°W	5488	286	4	0.1 - 1.1	1.22	-0.03	0.54
co2_rta_aircraft-pfp_1_allvalid_6000 7000masl	NOAA	Rarotonga, Cook Islands	21.25°S	159.83°W	6234	294	2	0.1 - 2.2	0.67	0.12	0.63
co2_san_aircraft-pfp_1_allvalid_0-1000masl	NOAA	Santarem, Brazil	2.85°S	54.95°W	576	95	1	1.6 - 20.8	0.61	0.58	4.61
co2_san_aircraft-pfp_1_allvalid_1000 2000masl	NOAA	Santarem, Brazil	2.85°S	54.95°W	1541	90	0	0.9 - 13.6	0.68	-0.00	2.08
co2_san_aircraft-pfp_1_allvalid_2000-3000masl	NOAA	Santarem, Brazil	2.85°S	54.95°W	2488	65	0	0.6 - 5.5	0.85	0.03	1.40
co2_san_aircraft-pfp_1_allvalid_3000 4000masl	NOAA	Santarem, Brazil	2.85°S	54.95°W	3436	81	0	0.5 - 2.9	1.24	0.13	1.10
co2_san_aircraft-pfp_1_allvalid_4000-5000masl	NOAA	Santarem, Brazil	2.85°S	54.95°W	4600	6	0	1.2 - 1.4	0.43	-0.26	0.92
co2_sca_aircraft-pfp_1_allvalid_0-1000masl	NOAA	Charleston, South Carolina, United States	32.77°N	79.55°W	616	415	7	1.1 - 6.8	0.92	-0.20	3.28
co2_sca_aircraft-pfp_1_allvalid_1000-2000masl	NOAA	Charleston, South Carolina, United States	32.77°N	79.55°W	1544	232	4	0.4 - 4.2	1.29	0.29	1.94
co2_sca_aircraft-pfp_1_allvalid_2000 3000masl	NOAA	Charleston, South Carolina, United States	32.77°N	79.55°W	2491	434	4	0.2 - 3.8	1.22	0.04	1.36
co2_sca_aircraft-pfp_1_allvalid_3000-4000masl	NOAA	Charleston, South Carolina, United States	32.77°N	79.55°W	3516	276	4	0.2 - 3.1	1.24	0.18	1.02

(table continued on next page)

Dataset	Lab.	Location	Latitude	Longitude	Elev. (m)	Used	Rej.	R (ppm)	χ^2	Bias (ppm)	SE (ppm)
co2_sca_aircraft-pfp_1_allvalid_4000-5000masl	NOAA	Charleston, South Carolina, United States	32.77°N	79.55°W	4456	372	10	0.2 - 2.2	1.26	0.09	1.03
co2_sca_aircraft-pfp_1_allvalid_5000-6000masl	NOAA	Charleston, South Carolina, United States	32.77°N	79.55°W	5489	234	4	0.3 - 2.0	1.17	0.12	0.83
co2_sca_aircraft-pfp_1_allvalid_6000-7000masl	NOAA	Charleston, South Carolina, United States	32.77°N	79.55°W	6412	268	4	0.3 - 1.6	1.39	0.16	0.84
co2_sca_aircraft-pfp_1_allvalid_7000-8000masl	NOAA	Charleston, South Carolina, United States	32.77°N	79.55°W	7452	339	9	0.3 - 1.6	1.35	0.13	0.78
co2_sca_aircraft-pfp_1_allvalid_8000-9000masl	NOAA	Charleston, South Carolina, United States	32.77°N	79.55°W	8125	76	6	0.3 - 1.8	0.74	0.27	1.31
co2_sca_aircraft-pfp_1_allvalid_9000-10000masl	NOAA	Charleston, South Carolina, United States	32.77°N	79.55°W	9362	17	0	0.2 - 4.9	1.94	-0.21	2.23
co2_sca_aircraft-pfp_1_allvalid_10000-11000masl	NOAA	Charleston, South Carolina, United States	32.77°N	79.55°W	10432	18	1	0.1 - 5.2	1.84	-0.26	1.86
co2_sca_aircraft-pfp_1_allvalid_11000-12000masl	NOAA	Charleston, South Carolina, United States	32.77°N	79.55°W	11160	7	0	0.7 - 5.6	0.83	-1.16	3.19
co2_sca_aircraft-pfp_1_allvalid_12000-13000masl	NOAA	Charleston, South Carolina, United States	32.77°N	79.55°W	12636	16	0	0.3 - 1.6	1.51	0.52	0.89
co2_sca_aircraft-pfp_1_allvalid_13000-14000masl	NOAA	Charleston, South Carolina, United States	32.77°N	79.55°W	13145	4	0	0.7 - 0.9	0.97	0.11	0.97
co2_sct_surface-pfp_1_allvalid	NOAA	Beech Island, South Carolina, United States	33.41°N	81.83°W	115	2302	2	3.3 - 41.7	0.25	-1.08	4.14
co2_sct_tower-insitu_1_allvalid-305magl	NOAA	Beech Island, South Carolina, United States	33.41°N	81.83°W	115	66619	479	3.4 - 16.3	0.68	-0.15	4.76

(table continued on next page)

Dataset	Lab.	Location	Latitude	Longitude	Elev. (m)	Used	Rej.	R (ppm)	χ^2	Bias (ppm)	SE (ppm)
co2_sct_tower-insitu_1_allvalid-31magl	NOAA	Beech Island, South Carolina, United States	33.41°N	81.83°W	115	11424	131	3.3 - 6.8	0.75	-0.57	4.76
co2_sct_tower-insitu_1_allvalid-61magl	NOAA	Beech Island, South Carolina, United States	33.41°N	81.83°W	115	11513	117	3.3 - 5.4	0.77	-0.69	4.45
co2_sey_surface-flask_1_representati	NOAA	Mahe Island, Seychelles	4.68°S	55.53°E	2	1398	0	0.4 - 1.4	0.63	-0.06	0.74
co2_sgp_aircraft-pfp_1_allvalid_0-1000masl	NOAA	Southern Great Plains, Oklahoma, United States	36.61°N	97.49°W	683	1518	21	1.1 - 14.5	0.91	-0.16	3.88
co2_sgp_aircraft-pfp_1_allvalid_1000 2000masl	NOAA	Southern Great Plains, Oklahoma, United States	36.61°N	97.49°W	1558	1609	18	0.8 - 6.0	0.97	0.00	2.51
co2_sgp_aircraft-pfp_1_allvalid_2000-3000masl	NOAA	Southern Great Plains, Oklahoma, United States	36.61°N	97.49°W	2452	1195	10	0.6 - 3.2	1.03	-0.23	1.55
co2_sgp_aircraft-pfp_1_allvalid_3000 4000masl	NOAA	Southern Great Plains, Oklahoma, United States	36.61°N	97.49°W	3459	988	9	0.6 - 3.1	1.02	-0.17	1.10
co2_sgp_aircraft-pfp_1_allvalid_4000-5000masl	NOAA	Southern Great Plains, Oklahoma, United States	36.61°N	97.49°W	4688	519	6	0.4 - 1.9	1.11	-0.16	0.94
co2_sgp_aircraft-pfp_1_allvalid_5000 6000masl	NOAA	Southern Great Plains, Oklahoma, United States	36.61°N	97.49°W	5395	257	4	0.4 - 3.0	1.08	0.01	1.20
co2_sgp_aircraft-pfp_1_allvalid_6000-7000masl	NOAA	Southern Great Plains, Oklahoma, United States	36.61°N	97.49°W	6464	8	0	1.0 - 1.0	0.30	0.15	0.83
co2_sgp_aircraft-pfp_1_allvalid_8000 9000masl	NOAA	Southern Great Plains, Oklahoma, United States	36.61°N	97.49°W	8062	1	1	0.6 - 0.6	2.62	0.13	1.22
co2_sgp_aircraft-pfp_1_allvalid_9000-10000masl	NOAA	Southern Great Plains, Oklahoma, United States	36.61°N	97.49°W	9686	8	0	0.6 - 0.6	1.51	0.01	0.64

(table continued on next page)

Dataset	Lab.	Location	Latitude	Longitude	Elev. (m)	Used	Rej.	R (ppm)	χ^2	Bias (ppm)	SE (ppm)
co2_sgp_aircraft-pfp_1_allvalid_1100 12000masl	NOAA	Southern Great Plains, Oklahoma, United States	36.61°N	97.49°W	11321	2	0	0.4 - 0.4	2.92	0.02	0.66
co2_sgp_aircraft-pfp_1_allvalid_12000-13000masl	NOAA	Southern Great Plains, Oklahoma, United States	36.61°N	97.49°W	12858	4	0	0.3 - 0.3	2.05	-0.04	0.51
co2_sgp_surface-flask_1_representati	NOAA	Southern Great Plains, Oklahoma, United States	36.61°N	97.49°W	314	1332	2	2.4 - 18.0	0.39	-0.93	4.06
co2_sgp_surface-insitu_64_allvalid-60magl	LBNL-ARM	Southern Great Plains, Oklahoma, United States	36.61°N	97.49°W	314	12397	148	2.8 - 10.9	0.74	-0.32	4.42
co2_shm_surface-flask_1_representati	NOAA	Shemya Island, Alaska, United States	52.71°N	174.13°E	23	912	1	0.7 - 10.9	0.55	-0.47	1.90
co2_sis_surface-flask_2_representative	CSIRO	Shetland Islands, Scotland	60.09°N	1.25°W	30	89	4	0.0 - 2.0	1.72	0.45	1.10
co2_smo_surface-flask_1_representati	NOAA	Tutuila, American Samoa	14.25°S	170.56°W	42	2683	2	0.1 - 2.9	0.55	-0.10	0.42
co2_smo_surface-flask_426_representative	SIO_CO2	Tutuila, American Samoa	14.25°S	170.56°W	42	598	3	0.2 - 143.9	0.80	-0.09	0.48
co2_smo_surface-flask_4_representati	SIO	Tutuila, American Samoa	14.25°S	170.56°W	42	389	5	0.1 - 5.4	0.54	-0.08	0.67
co2_smo_surface-insitu_1_allvalid	NOAA	Tutuila, American Samoa	14.25°S	170.56°W	42	18131	0	0.2 - 2.4	1.34	-0.03	0.33
co2_snp_tower-insitu_1_allvalid-10magl	NOAA	Shenandoah National Park, United States	38.62°N	78.35°W	1008	10904	21	3.2 - 14.0	0.45	0.87	5.83
co2_snp_tower-insitu_1_allvalid-17magl	NOAA	Shenandoah National Park, United States	38.62°N	78.35°W	1008	11054	16	3.6 - 14.8	0.39	0.74	5.56
co2_snp_tower-insitu_1_allvalid-5magl	NOAA	Shenandoah National Park, United States	38.62°N	78.35°W	1008	10763	21	3.1 - 13.1	0.47	0.17	5.47
co2_spl_surface-insitu_3_nonlocal	NCAR	Storm Peak Laboratory (Desert Research Institute), United States	40.45°N	106.73°W	3210	67863	498	1.1 - 3.2	0.83	-0.57	1.65

(table continued on next page)

Dataset	Lab.	Location	Latitude	Longitude	Elev. (m)	Used	Rej.	R (ppm)	χ^2	Bias (ppm)	SE (ppm)
co2_spo_surface-flask_1_representati	NOAA	South Pole, Antarctica, United States	89.98°S	24.80°W	2810	2324	1	0.1 - 1.5	0.33	0.09	0.16
co2_spo_surface-flask_426_representative	SIO_CO2	South Pole, Antarctica, United States	89.98°S	24.80°W	2810	371	2	0.1 - 33.0	0.45	0.11	0.22
co2_spo_surface-flask_4_representati	SIO	South Pole, Antarctica, United States	89.98°S	24.80°W	2810	383	0	0.1 - 1.7	0.45	0.12	0.16
co2_spo_surface-insitu_1_allvalid	NOAA	South Pole, Antarctica, United States	89.98°S	24.80°W	2810	23165	2	0.1 - 0.7	1.35	0.01	0.09
co2_stm_surface-flask_1_representati	NOAA	Ocean Station M, Norway	66.00°N	2.00°E	0	1663	8	0.4 - 2.5	0.56	-0.13	1.35
co2_str_surface-pfp_1_allvalid	NOAA	Sutro Tower, San Francisco, California, United States	37.76°N	122.45°W	254	4107	57	1.1 - 13.7	0.78	-1.08	2.93
co2_sum_surface-flask_1_representati	NOAA	Summit, Greenland	72.60°N	38.42°W	3210	1411	4	0.4 - 1.9	0.61	-0.01	0.80
co2_svv_tower-insitu_20_allvalid-27magl	NIES	Savvushka, Russia	51.33°N	82.13°E	400	8216	16	2.2 - 8.6	0.41	-0.50	3.88
co2_svv_tower-insitu_20_allvalid-52magl	NIES	Savvushka, Russia	51.33°N	82.13°E	400	7785	16	2.2 - 8.4	0.42	-0.37	3.83
co2_syo_surface-flask_1_representative	NOAA	Syowa Station, Antarctica, Japan	69.01°S	39.59°E	14	738	0	0.1 - 0.5	0.68	-0.05	0.17
co2_tab_aircraft-pfp_26_representati 1000masl	IPEN	Tabatinga, Brazil	5.95°S	70.07°W	681	103	0	1.6 - 17.2	0.73	-1.12	9.04
co2_tab_aircraft-pfp_26_representative_1000-2000masl	IPEN	Tabatinga, Brazil	5.95°S	70.07°W	1519	124	0	1.2 - 9.4	0.79	-0.16	4.36
co2_tab_aircraft-pfp_26_representati 3000masl	IPEN	Tabatinga, Brazil	5.95°S	70.07°W	2394	69	3	0.5 - 4.4	0.98	-0.03	2.66
co2_tab_aircraft-pfp_26_representative_3000-4000masl	IPEN	Tabatinga, Brazil	5.95°S	70.07°W	3499	120	1	0.3 - 2.8	0.72	-0.17	1.22

(table continued on next page)

Dataset	Lab.	Location	Latitude	Longitude	Elev. (m)	Used	Rej.	R (ppm)	χ^2	Bias (ppm)	SE (ppm)
co2_tab_aircraft-pfp_26_representati 5000masl	IPEN	Tabatinga, Brazil	5.95°S	70.07°W	4420	37	0	0.3 - 3.0	1.03	0.08	1.22
co2_tap_surface-flask_1_representative	NOAA	Tae-ahn Peninsula, Republic of Korea	36.74°N	126.13°E	16	1925	15	0.5 - 15.4	0.45	-0.78	5.52
co2_tf1_shipboard-insitu_20_allvalid	NIES	Trans Future 1 (M/S Trans Future 1 of the Toyofuji Shipping Co., Ltd), N/A	14.36°N	115.24°E	Surface	80315	220	3.5 - 54.3	0.25	-0.86	3.47
co2_tf5_shipboard-insitu_20_allvalid	NIES	Trans Future 5 (M/S Trans Future 5 of Toyofuji Shipping Co., Ltd.), N/A	8.80°S	152.00°E	Surface	272835	3520	1.3 - 36.4	0.35	-0.03	1.94
co2_tgc_aircraft-pfp_1_allvalid_0-1000masl	NOAA	Sinton, Texas, United States	27.73°N	96.86°W	619	347	12	0.6 - 4.8	1.11	-0.25	2.75
co2_tgc_aircraft-pfp_1_allvalid_1000-2000masl	NOAA	Sinton, Texas, United States	27.73°N	96.86°W	1555	198	4	0.4 - 2.8	1.01	0.14	1.64
co2_tgc_aircraft-pfp_1_allvalid_2000 3000masl	NOAA	Sinton, Texas, United States	27.73°N	96.86°W	2518	369	4	0.2 - 2.4	0.96	-0.07	1.21
co2_tgc_aircraft-pfp_1_allvalid_3000-4000masl	NOAA	Sinton, Texas, United States	27.73°N	96.86°W	3489	216	4	0.1 - 1.6	1.21	-0.01	0.81
co2_tgc_aircraft-pfp_1_allvalid_4000 5000masl	NOAA	Sinton, Texas, United States	27.73°N	96.86°W	4461	362	4	0.2 - 1.5	1.13	-0.01	0.78
co2_tgc_aircraft-pfp_1_allvalid_5000-6000masl	NOAA	Sinton, Texas, United States	27.73°N	96.86°W	5547	190	3	0.2 - 1.1	1.25	0.10	0.69
co2_tgc_aircraft-pfp_1_allvalid_6000 7000masl	NOAA	Sinton, Texas, United States	27.73°N	96.86°W	6414	214	3	0.3 - 1.0	1.40	0.16	0.67
co2_tgc_aircraft-pfp_1_allvalid_7000-8000masl	NOAA	Sinton, Texas, United States	27.73°N	96.86°W	7437	283	12	0.0 - 1.2	1.49	0.12	0.66

(table continued on next page)

Dataset	Lab.	Location	Latitude	Longitude	Elev. (m)	Used	Rej.	R (ppm)	χ^2	Bias (ppm)	SE (ppm)
co2_tgc_aircraft-pfp_1_allvalid_8000 9000masl	NOAA	Sinton, Texas, United States	27.73°N	96.86°W	8056	61	7	0.3 - 1.1	1.34	0.33	0.73
co2_thd_aircraft-pfp_1_allvalid_0-1000masl	NOAA	Trinidad Head, California, United States	41.05°N	124.15°W	627	290	12	0.9 - 17.1	0.67	-0.74	5.64
co2_thd_aircraft-pfp_1_allvalid_1000 2000masl	NOAA	Trinidad Head, California, United States	41.05°N	124.15°W	1534	168	2	0.3 - 2.9	1.25	0.19	1.25
co2_thd_aircraft-pfp_1_allvalid_2000-3000masl	NOAA	Trinidad Head, California, United States	41.05°N	124.15°W	2475	304	8	0.1 - 3.0	1.11	0.06	1.29
co2_thd_aircraft-pfp_1_allvalid_3000 4000masl	NOAA	Trinidad Head, California, United States	41.05°N	124.15°W	3516	210	8	0.4 - 3.4	1.32	0.20	1.43
co2_thd_aircraft-pfp_1_allvalid_4000-5000masl	NOAA	Trinidad Head, California, United States	41.05°N	124.15°W	4441	243	9	0.2 - 3.1	1.33	0.19	1.44
co2_thd_aircraft-pfp_1_allvalid_5000 6000masl	NOAA	Trinidad Head, California, United States	41.05°N	124.15°W	5479	173	2	0.1 - 2.5	1.21	0.10	1.20
co2_thd_aircraft-pfp_1_allvalid_6000-7000masl	NOAA	Trinidad Head, California, United States	41.05°N	124.15°W	6458	215	7	0.2 - 1.8	1.45	0.08	0.99
co2_thd_aircraft-pfp_1_allvalid_7000 8000masl	NOAA	Trinidad Head, California, United States	41.05°N	124.15°W	7472	219	6	0.3 - 1.9	1.20	0.09	1.05
co2_thd_aircraft-pfp_1_allvalid_8000-9000masl	NOAA	Trinidad Head, California, United States	41.05°N	124.15°W	8035	11	2	0.7 - 2.5	1.10	0.24	1.54
co2_thd_surface-flask_1_representati	NOAA	Trinidad Head, California, United States	41.05°N	124.15°W	107	1262	18	1.0 - 34.3	0.54	-2.24	7.43
co2_tik_surface-flask_1_representative	NOAA	Hydrometeorological Observatory of Tiksi, Russia	71.60°N	128.89°E	19	471	4	1.2 - 17.1	0.25	-0.62	4.27

(table continued on next page)

Dataset	Lab.	Location	Latitude	Longitude	Elev. (m)	Used	Rej.	R (ppm)	χ^2	Bias (ppm)	SE (ppm)
co2_ulb_aircraft-pfp_1_allvalid_1000 2000masl	NOAA	Ulaanbaatar, Mongolia	47.40°N	106.00°E	1648	165	4	0.4 - 5.5	0.70	-0.04	1.59
co2_ulb_aircraft-pfp_1_allvalid_2000-3000masl	NOAA	Ulaanbaatar, Mongolia	47.40°N	106.00°E	2469	148	6	0.1 - 3.8	1.91	-0.06	1.26
co2_ulb_aircraft-pfp_1_allvalid_3000 4000masl	NOAA	Ulaanbaatar, Mongolia	47.40°N	106.00°E	3478	158	3	0.3 - 3.5	1.84	-0.35	1.42
co2_ulb_aircraft-pfp_1_allvalid_4000-5000masl	NOAA	Ulaanbaatar, Mongolia	47.40°N	106.00°E	4209	60	0	0.1 - 1.8	2.40	-0.30	1.13
co2_ulb_aircraft-pfp_1_allvalid_5000 6000masl	NOAA	Ulaanbaatar, Mongolia	47.40°N	106.00°E	5718	2	0	0.7 - 0.7	0.24	0.34	0.16
co2_ush_surface-flask_1_representative	NOAA	Ushuaia, Argentina	54.85°S	68.31°W	12	462	2	0.3 - 1.6	0.26	-0.27	0.74
co2_uta_surface-flask_1_representati	NOAA	Wendover, Utah, United States	39.90°N	113.72°W	1327	1416	6	0.9 - 8.3	0.49	0.69	2.86
co2_uum_surface-flask_1_representative	NOAA	Ulaan Uul, Mongolia	44.45°N	111.10°E	1007	1547	0	2.0 - 7.4	0.58	-0.29	3.43
co2_vgn_tower-insitu_20_allvalid-42magl	NIES	Vaganovo, Russia	54.50°N	62.32°E	200	8988	21	2.7 - 6.8	0.53	0.01	3.69
co2_vgn_tower-insitu_20_allvalid-85magl	NIES	Vaganovo, Russia	54.50°N	62.32°E	200	8685	14	2.8 - 6.8	0.54	-0.14	3.85
co2_wbi_aircraft-pfp_1_allvalid_0-1000masl	NOAA	West Branch, Iowa, United States	41.72°N	91.35°W	628	142	3	1.5 - 13.9	1.28	0.14	6.16
co2_wbi_aircraft-pfp_1_allvalid_1000-2000masl	NOAA	West Branch, Iowa, United States	41.72°N	91.35°W	1546	300	14	0.4 - 7.4	1.34	-0.59	3.52
co2_wbi_aircraft-pfp_1_allvalid_2000 3000masl	NOAA	West Branch, Iowa, United States	41.72°N	91.35°W	2552	170	1	0.5 - 8.1	1.18	-0.52	1.68

(table continued on next page)

Dataset	Lab.	Location	Latitude	Longitude	Elev. (m)	Used	Rej.	R (ppm)	χ^2	Bias (ppm)	SE (ppm)
co2_wbi_aircraft-pfp_1_allvalid_3000-4000masl	NOAA	West Branch, Iowa, United States	41.72°N	91.35°W	3515	304	1	0.5 - 3.3	1.00	-0.04	1.38
co2_wbi_aircraft-pfp_1_allvalid_4000 5000masl	NOAA	West Branch, Iowa, United States	41.72°N	91.35°W	4549	196	2	0.4 - 2.8	1.03	-0.04	1.17
co2_wbi_aircraft-pfp_1_allvalid_5000-6000masl	NOAA	West Branch, Iowa, United States	41.72°N	91.35°W	5511	256	1	0.3 - 2.8	1.23	0.08	1.15
co2_wbi_aircraft-pfp_1_allvalid_6000 7000masl	NOAA	West Branch, Iowa, United States	41.72°N	91.35°W	6496	233	0	0.2 - 1.9	1.28	-0.08	1.13
co2_wbi_aircraft-pfp_1_allvalid_7000-8000masl	NOAA	West Branch, Iowa, United States	41.72°N	91.35°W	7484	237	6	0.1 - 2.1	1.23	0.04	1.03
co2_wbi_aircraft-pfp_1_allvalid_8000 9000masl	NOAA	West Branch, Iowa, United States	41.72°N	91.35°W	8047	26	2	0.3 - 1.7	1.13	-0.04	1.16
co2_wbi_surface-pfp_1_allvalid	NOAA	West Branch, Iowa, United States	41.72°N	91.35°W	242	3118	6	1.1 - 38.0	0.34	-0.99	5.18
co2_wbi_tower-insitu_1_allvalid-31magl	NOAA	West Branch, Iowa, United States	41.72°N	91.35°W	242	12259	119	3.7 - 11.1	0.82	-0.39	5.76
co2_wbi_tower-insitu_1_allvalid-379magl	NOAA	West Branch, Iowa, United States	41.72°N	91.35°W	242	73938	899	2.9 - 18.0	0.89	-0.43	4.77
co2_wbi_tower-insitu_1_allvalid-99magl	NOAA	West Branch, Iowa, United States	41.72°N	91.35°W	242	12460	103	3.0 - 11.0	0.83	-0.45	5.60
co2_wgc_surface-pfp_1_allvalid	NOAA	Walnut Grove, California, United States	38.27°N	121.49°W	0	2488	8	3.6 - 126.2	0.38	-2.01	8.17
co2_wgc_tower-insitu_1_allvalid-30magl	NOAA	Walnut Grove, California, United States	38.27°N	121.49°W	0	12082	142	3.3 - 13.7	0.83	-1.84	7.20

(table continued on next page)

Dataset	Lab.	Location	Latitude	Longitude	Elev. (m)	Used	Rej.	R (ppm)	χ^2	Bias (ppm)	SE (ppm)
co2_wgc_tower-insitu_1_allvalid-483magl	NOAA	Walnut Grove, California, United States	38.27°N	121.49°W	0	73919	647	2.9 - 20.5	0.69	1.42	6.08
co2_wgc_tower-insitu_1_allvalid-91magl	NOAA	Walnut Grove, California, United States	38.27°N	121.49°W	0	12490	137	3.2 - 23.2	0.75	-2.09	6.93
co2_wis_surface-flask_1_representative	NOAA	Weizmann Institute of Science at the Arava Institute, Ketura, Israel	29.96°N	35.06°E	151	1606	4	0.6 - 7.2	0.64	-0.69	2.23
co2_wkt_surface-pfp_1_allvalid	NOAA	Moody, Texas, United States	31.31°N	97.33°W	251	2776	6	0.5 - 41.3	0.31	-0.69	3.47
co2_wkt_tower-insitu_1_allvalid-122magl	NOAA	Moody, Texas, United States	31.31°N	97.33°W	251	17336	292	2.5 - 7.6	0.79	-0.53	3.58
co2_wkt_tower-insitu_1_allvalid-244magl	NOAA	Moody, Texas, United States	31.31°N	97.33°W	251	15893	139	2.0 - 8.4	0.92	-0.98	4.03
co2_wkt_tower-insitu_1_allvalid-30magl	NOAA	Moody, Texas, United States	31.31°N	97.33°W	251	17805	297	2.5 - 4.7	0.79	-0.32	3.80
co2_wkt_tower-insitu_1_allvalid-457magl	NOAA	Moody, Texas, United States	31.31°N	97.33°W	251	110656	1354	2.4 - 42.3	0.79	-0.47	3.12
co2_wkt_tower-insitu_1_allvalid-62magl	NOAA	Moody, Texas, United States	31.31°N	97.33°W	251	2628	33	2.2 - 5.7	0.94	-0.85	3.85
co2_wkt_tower-insitu_1_allvalid-9magl	NOAA	Moody, Texas, United States	31.31°N	97.33°W	251	3038	43	2.6 - 6.3	0.98	-0.75	4.56
co2_wlg_surface-flask_1_representative	NOAA	Mt. Waliguan, Peoples Republic of China	36.29°N	100.90°E	3810	1355	2	1.1 - 5.2	0.54	-0.27	2.59
co2_wpc_shipboard-flask_1_representati	NOAA	Western Pacific Cruise, N/A	0.75°N	151.28°E	Surface	253	1	0.3 - 7.8	0.50	-0.10	0.71
co2_wsa_surface-insitu_6_allvalid	EC	Sable Island, Nova Scotia, Canada	43.93°N	60.02°W	5	14516	303	1.6 - 3.8	0.81	-0.11	2.63

(table continued on next page)

Dataset	Lab.	Location	Latitude	Longitude	Elev. (m)	Used	Rej.	R (ppm)	χ^2	Bias (ppm)	SE (ppm)
co2_yak_tower-insitu_20_allvalid-11magl	NIES	Yakutsk, Russia	62.09°N	129.36°E	210	5315	9	3.0 - 12.5	0.42	-0.75	6.12
co2_yak_tower-insitu_20_allvalid-77magl	NIES	Yakutsk, Russia	62.09°N	129.36°E	210	5427	10	3.1 - 12.3	0.44	-0.11	5.90
co2_zep_surface-flask_1_representati	NOAA	Ny-Alesund, Svalbard, Norway and Sweden	78.91°N	11.89°E	474	1687	10	0.4 - 2.3	0.68	0.00	1.03
co2_zep_surface-insitu_56_allvalid	NILU	Ny-Alesund, Svalbard, Norway and Sweden	78.91°N	11.89°E	474	1310	12	0.3 - 3.5	1.11	0.36	0.96

Table 3: Summary of Observational Sites Used in CarbonTracker. The site location is specified by latitude, longitude and elevation in meters above sea level. The number of observations actually assimilated for each dataset is listed in the column "Used", and the number rejected due to inability to fit the observations is listed in the column "Rej.". Model-data-mismatch (R) is a value assigned to a given site that is meant to quantify our expected ability to simulate observations there. In this table we report the range of R values assigned to dataset observations by our "adaptive" model-data mismatch scheme (Sec. 7.2). These values are principally determined from the limitations of the atmospheric transport model. It is part of the standard deviation used to interpret the difference between a simulation first guess (Hx) of an observation and the actual measured value (z). The other component, HPH^{T}, is a measure of the ability of the ensemble Kalman filter to improve its simulated value for this observation by adjusting fluxes. These elements together form the innovation χ statistic for the site: $\chi = (z - Hx)/\sqrt{(HPH^{\mathrm{T}} + R^2)}$. The innovation χ^2 reported above is the mean of all squared χ values for a given site. An average χ^2 below 1.0 indicates that the $HPH^{\mathrm{T}} + R^2$ values are too large. Conversely, values above 1.0 mean that this standard deviation is underestimated. The bias and SE columns are statistics of the posterior residuals (final modeled values - measured values). The bias is the mean of these residuals; the SE is the standard error of those residuals.

7.4 References

- ESRL Carbon Cycle Program
- WMO/GAW Report No. 168, 2006
- Thoning, K. W., P. P. Tans, and W. D. Komhyr (1989), Atmospheric carbon dioxide at Mauna Loa Observatory: 2. Analysis of the NOAA GMCC data, 19741985, J. Geophys. Res., 94(D6), 85498565, doi:10.1029/JD094iD06p08549.

8 Ensemble data assimilation

Data assimilation is the process by which a model simulation is adjusted to agree with observations. Model simulations may drift off from reality for a number of reasons. Some models are highly nonlinear, and depend sensitively on knowing the system state with high accuracy. Weather models fall into this category, and as a result reliable forecast systems depend on having a constant stream of meteorological data to correct their simulations. In contrast, models like CarbonTracker need data assimilation not because the controlling dynamics are nonlinear, but because those dynamics are not well known. CarbonTracker uses approximate or estimated rules about the evolution of surface CO_2 fluxes, then corrects these approximate projections using observational constraints. The resulting optimal surface flux estimates can then be used to better understand the functioning of the carbon cycle.

Data assimilation is usually a cyclical process, in which estimates get refined over time as more observations become available. Mathematically, data assimilation can be performed using a wide variety of techniques, including variational and ensemble methods. Assimilation systems involving simulations of the global atmosphere are often implemented on highly parallel supercomputers in order to distribute the workload among many computational cores. CarbonTracker is an exmaple of such a model because it relies heavily on estimates of global atmospheric transport.

CarbonTracker model predictions are mainly limited by the relatively simple representations of CO_2 surface exchange used to predict land biosphere and ocean fluxes and emissions from fossil fuel combustion and wildfires. As described in the following section, we use data assimilation techniques to modify these surface fluxes so that the resulting atmospheric distribution of CO_2 agrees optimally with measurements. We do this by estimating a set of spatially- and temporally-varying scaling factors that multiply first-guess predictions from prior flux models. Data assimilation allows us to determine optimal values for these scaling

factors.

8.1 Parameterization of unknowns

CO_2 fluxes $F(x, y, t)$ in CarbonTracker are parameterized according to

$$F(x, y, t) = \lambda(x, y, t)\Big(F_{\text{land}}(x, y, t) + F_{\text{ocean}}(x, y, t)\Big) + F_{\text{FF}}(x, y, t) + F_{\text{fire}}(x, y, t), \tag{11}$$

where F_{land}, F_{ocean}, F_{FF}, and F_{bio} are prior flux model predictions for land biosphere, ocean, fossil fuel and wildfire emissions respectively, and λ represents a set of unknown multiplicative scaling factors applied to the fluxes, to be estimated in the assimilation. These scaling factors are the final product of our assimilation and together with the prior flux models determine CarbonTracker optimized fluxes. Note that no scaling factors are applied to the fossil fuel and fire modules. The fossil fuel and wildfire fluxes are relatively well-known from prior flux models compared to highly-uncertain land biosphere and ocean fluxes, and as a result we impose those emissions without modification in our model.

8.1.1 Optimization regions

The scaling factors λ are estimated independently for each week and optimization region. They are assumed to be constant over this time period and spatial domain. Each scaling factor is associated with a particular region of the globe, as in the TransCom inversion study (*e.g.* Gurney *et al.*, 2002). Currently the geographic distribution of these optimization regions is fixed. The choice of regions is a strong *a priori* design decision determining the reliability of the resulting fluxes. In particular, the scale of optimization regions is chosen to minimize "aggregation errors" (Kaminski *et al.*, 2001), while limiting the set of unknown parameters to a manageable number. Following Jacobson *et al.* (2007), we have divide the global ocean into 30 basins encompassing large-scale ocean circulation and biogeochemical features. The terrestrial biosphere is divided up according to ecosystem type and geographical domain. Specifically, each of the 11 TransCom land regions is subdivided into a maximum of 19 "ecoregions" according to its Olson (1992) vegetation classification. The set of ecoregions over North America is summarized in Table 4 and Figure 17. Note that there is currently no requirement for ecoregions to be contiguous, and a single scaling factor can be applied to the same vegetation type on both sides of a continent. Further details on ecoregions can be found in Section 9

Theoretically, this approach leads to a total number of 11*19+30=239 optimizable scaling factors for

category	Olson V 1.3	Percentage area
1	Conifer Forest	19.0%
2	Broadleaf Forest	1.3%
3	Mixed Forest	7.5%
4	Grass/Shrub	12.6%
5	Tropical Forest	0.3%
6	Scrub/Woods	2.1%
7	Semitundra	19.4%
8	Fields/Woods/Savanna	4.9%
9	Northern Taiga	8.1%
10	Forest/Field	6.3%
11	Wetland	1.7%
12	Deserts	0.1%
13	Shrub/Tree/Suc	0.1%
14	Crops	9.7%
15	Conifer Snowy/Coastal	0.4%
16	Wooded tundra	1.7%
17	Mangrove	0.0%
18	Non-optimized areas (ice, polar desert, inland seas)	0.0%
19	Water	4.9%

Table 4: Ecosystem types over North America

each week, but the actual number of optimization regions is only 156 since some ecosystem types are not represented in every TransCom region. It should be noted also that we have chosen to not optimize scaling factors for ice-covered regions, inland water bodies, and deserts, since the CO_2 flux from these regions is negligible.

It is important to note that even though only one parameter is available to scale, for instance, the flux from coniferous forests in Boreal North America, each $1^\circ \times 1^\circ$ grid box predominantly covered by coniferous forests will have a different optimized flux $\lambda F_{\text{land}}(x, y, t)$ depending on local temperature, radiation, and emissions as simulated by the prior flux model.

Ecosystem types are based on the vegetation classification of Olson, (1992). Note that we have adjusted the original 29 categories into only 19 regions. This was done mainly to fill the unused categories 16, 17, and 18, and to group the similar categories 23-26+29. Table 4 shows each vegetation category considered. Percentages indicate the relative area in North America associated with each category.

Each $1^\circ \times 1^\circ$ pixel of our domain was assigned one of the categories above based on the Olson category that was most prevalent in the $0.5^\circ \times 0.5^\circ$ underlying area.

8.1.2 Assimilation window

Measured CO_2 mole fractions are the result of upstream surface fluxes and atmospheric transport, which includes both advective movement and diffusive mixing. Near-field surface fluxes can cause significant changes in CO_2 mole fractions, whereas flux signals from further upstream become spread out and diluted. Generally speaking, the longer in the past a flux event occurred, the smaller its impact will be on a given sample of air (although it will be spread out through a larger volume of the atmosphere). Thus we choose an "assimilation window" that represents how far back in time we expect to be able to pinpoint a given flux signal from available measurements. A good discussion of this topic can be found in Bruhwiler *et al*. (2005).

In previous versions of CarbonTracker, the assimilation window was chosen to be five weeks long, meaning that a measurement could cause revisions in surface fluxes only over the 5 weeks leading up to that measurement. In CT2017, we have extended the assimilation window length to 12 weeks. This helps to resolve fluxes in regions of the world with less dense observational coverage (the tropics, Southern Hemisphere, and parts of Asia).

This assimilation window is moved forward on each cycle of our estimation system, so that new weeks are introduced at the "head" of the filter, and the weeks that fall out the "tail" of the filter are finalized. Prior to CT2017, the 5-week assimilation window was moved forward one week at a time. In CT2017, the 12-week assimilation window is moved forward two weeks at a time. Scaling factors λ retain their weekly resolution. Each cycle of the inversion system requires running the atmospheric model for a length of time equal to the assimilation window length plus the window step size. For previous CarbonTracker releases, this was 6 weeks per cycle; for CT2017 it is 14 weeks per cycle. The extra computing time required by the longer assimilation window is balanced somewhat by the two-week stepping, and we have found that CT2017 required only about 15% more computing time per than previous releases.

8.1.3 Ensemble size and localization

The ensemble system used to solve for the scalar multiplication factors is similar to that in Peters *et al*. (2005) and based on the square root ensemble Kalman filter of Whitaker and Hamill (2002). Ensemble statistics are created from 150 randomly-chosen members, each with its own background CO_2 concentration field to represent the time history of that member's surface fluxes. The ensemble Kalman filter looks for correlations between these random flux perturbations and resulting changes in simulated CO_2 measurements. We

might expect that the entire ensemble would agree that increasing the CO_2 flux in a given region results in greater simulated CO_2 at a nearby downwind site. However, because we approximate the flux covariance matrix with a random sample of 150 members, sometimes spurious correlations appear. It is unphysical, for instance, that a measurement at Summit, Greenland could be strongly influenced by surface exchange in the southern Indian Ocean, within the time span of our assimilation window. Any such correlation between the flux ensemble and the measurement in question might be spurious. Localization is a technique developed for numerical weather prediction in which unphysical correlations are diagnosed and systematically ignored (Houtekamer and Mitchell, 1998). We only perform localization for certain datasets. Notably, it is not used for datasets judged to represent hemisphere-scale signals, such as those from marine boundary layer sites in remote locations.

Our localization technique is based on the linear correlation coefficient between the 150 parameter deviations and 150 observation deviations for each parameter/observation pair. If the relationship between a parameter deviation and its modeled observational impact is statistically significant, then that relationship is retained. Otherwise, the relationship is assumed to be spurious noise due to the numerical approximation of the covariance matrix by the limited ensemble. We accept relationships that reach 95% significance in a Student's T-test with a two-tailed probability distribution.

8.1.4 Dynamical model

In CarbonTracker, the dynamical model is applied to the ensemble-mean parameter values λ as:

$$\lambda^-[t] = (\lambda_0^- + \lambda^+[t-1] + \lambda^+[t-2])/3 \tag{12}$$

Where $\lambda^-[t]$ is the prior value of the scaling factors for timestep t, λ_0^- is the initial prior vector with all elements set to 1.0, and $\lambda^+[t-1]$ and $\lambda^+[t-2]$ are the posterior ("analyzed") scaling factors for timesteps $t-1$ and $t-2$ repsectively. This model describes that parameter values λ for a new time step are chosen as a combination of optimized values from the two previous time steps and a fixed overall prior value of 1.0. This operation is similar to the simple persistence forecast used in Peters *et al.* (2005), but represents a smoothing over three time steps, which attenuates variations in the forecast of λ in time. The inclusion of the prior term λ_0^- acts as a regularization (Baker *et al.*, 2006) and ensures that the parameters in our system will eventually revert back to predetermined prior values when there is no information coming from observations. Note that

our dynamical model equation does not include an error term on the dynamical model, for the simple reason that we don't know the error of this model. This is reflected in the treatment of covariance, which is always set to a fixed prior covariance structure and not forecast with our dynamical model.

8.2 Covariance structure

The prior covariance structure P_0^- describes the magnitude of the uncertainty on each parameter, plus their correlation in space. The latter is applied such that correlations between the same ecosystem types in different TransCom regions decrease exponentially with distance (L=2000km), and thus assumes a coupling *between* the behavior of the same ecosystems in close proximity to one another (such as coniferous forests in Boreal and Temperate North America). Furthermore, all ecosystems *within* tropical TransCom regions are coupled decreasing exponentially with distance since we do not believe the current observing network can constrain tropical fluxes on sub-continental scales, and want to prevent spurious compensating source/sink pairs ("dipoles") to occur in the tropics.

In our standard assimilation, the chosen standard deviation is 80% on land parameters. All parameters have the same variance within the land or ocean domain. Because the parameters multiply the net flux though, ecosystems with larger weekly mean net fluxes have a larger variance in absolute flux magnitude.

8.3 Multiple prior models

In Bayesian estimation systems like CarbonTracker, there is a potential for bias from a flux prior to propagate through the inversion system to the final result. It is difficult to quantify this effect, and as a result it is generally considered a requirement that flux priors be unbiased. We cannot guarantee this for any of our prior fluxes, be they the prior estimates for terrestrial or oceanic exchange, or the presumed wildfire and fossil fuel emissions. In order to explicitly quantify the impact of prior bias on our solution, in CT2017 we present the average of two inversions using different priors. We have used two terrestrial flux priors (including two wildfire emissions estimates), two air-sea CO_2 exchange priors, and two estimates of imposed fossil fuel emissions in a factorial design experiment. Whereas previous releases conducted 8 independent inversions exploring each unique combination of priors in a factorial design, we have determined that interactions between priors are negligible. Thus, the quantification of uncertainty due to prior selection can be explored using just two inversions, each using a different set of priors. We present as a final result the mean flux

between these two inversions and the atmospheric CO_2 distribution resulting from applying these mean fluxes to our atmospheric transport model. Each of the priors is described in detail in its corresponding documentation section.

8.3.1 Posterior uncertainties in CarbonTracker

The formal "internal" error estimates produced by CarbonTracker are unrealistically large. This is largely a result of the dynamical model that introduces a fresh prior covariance matrix with every new week entering the assimilation window. Uncertainties using the new 12-week assimilation window are smaller that those from previous CarbonTracker releases that used a much shorter five-week assimilation window.

Uncertainties in CarbonTracker tend to increase as larger regions are considered; regional errors mostly just add in quadrature without any cancellation from dipole anticorrelation. Whereas many inversions yield smaller errors as the spatial extent of the region being considered increases, CarbonTracker acts in the opposite fashion. This is perhaps most obvious in the estimate of CarbonTracker's global annual surface flux of carbon dioxide. While CT2017 estimates a one-sigma error of more than 5 PgC yr^{-1} on its global flux, this quantity is in actuality much more well-constrained. This is evident from CarbonTracker's excellent agreement with observational estimates of atmospheric growth rate.

In CT2017, error estimates are about a factor of two larger than in previous releases, mainly due to the retuning of the land prior covariance discussed above. However, uncertainties presented for CT2017 take into account not only the "internal" flux uncertainty generated by a single inversion, but also the across-model "external" uncertainty representing the spread of the inversion models due to the choice of prior flux.

8.4 References

- L. M. P. Bruhwiler, A. M. Michalak, W. Peters, D. F. Baker, and P. Tans. An improved Kalman smoother for atmospheric inversions. Atmospheric Chemistry and Physics, 5:26912702, 2005. doi: 10. 5194/acp-5-2691-2005.
- Kaminski, T., P. J. Rayner, M. Heimann, and I. G. Enting (2001), On aggregation errors in atmospheric transport inversions, J. Geophys. Res., 106(D5), 47034715, doi:10.1029/2000JD900581.
- Peters, W., M. C. Krol, E. J. Dlugokencky, F. J. Dentener, P. Bergamaschi, G. Dutton, P. v. Velthoven,

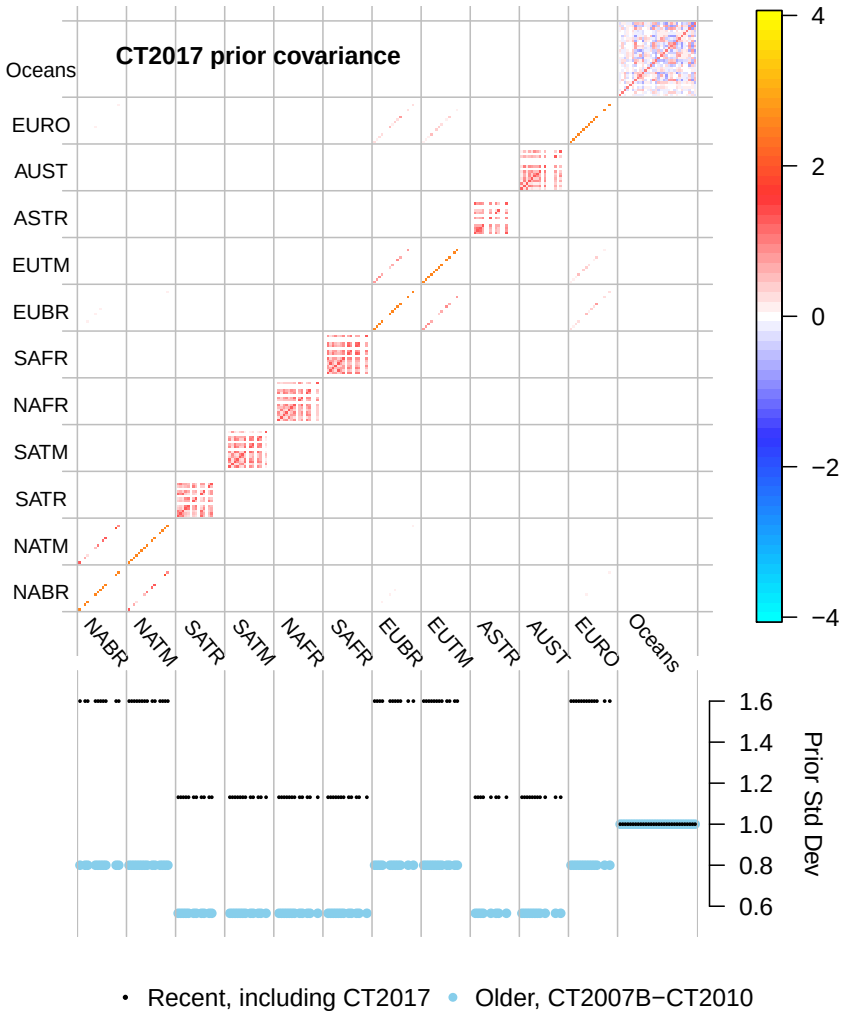

Figure 14: CT2017 prior covariance structure. The prior covariance matrix (top panel) and the square root of diagonal members of this matrix (bottom panel). Covariance matrix quantities are dimensionless squared scaling factors, and the bottom panel is the square root of this. TransCom land regions form the first 11 large divisions on the axes here. As described above, each of those regions contains 19 potential ecosystems. Correlations between similar ecosystems in proximate TransCom regions are visible in North America (*e.g.* NABR and NATM, the boreal and temperate North American regions) and Eurasia. Within tropical TransCom regions, however, differing ecosystems are assigned a non-zero prior covariance, which is visible here as red block-like structures on the diagonal within, for example, the South America Tropical (SATR) TransCom region. Ocean regions have a more complicated covariance structure that depends on which prior is used; the structure shown here is that of the ocean inversion flux prior. The lower panel of this diagram compares the on-diagonal elements of the prior covariance matrix by plotting their square roots. The resulting standard deviations are directly comparable to the percentages discussed in section 3 above; 0.8 is equivalent to 80%. The retuning of the covariance matrix for CT2017's multiple-prior simulation is made evident by also showing these values from previous CarbonTracker releases in light blue.

J. B. Miller, L. Bruhwiler, and P. P. Tans (2004), Toward regional-scale modeling using the two-way nested global model TM5: Characterization of transport using SF_6, J. Geophys. Res., 109, D19314, doi:10.1029/2004JD005020

- Jeffrey S. Whitaker and Thomas M. Hamill, 2002: Ensemble Data Assimilation without Perturbed Observations. Mon. Wea. Rev., 130, 19131924.
  doi: http://dx.doi.org/10.1175/1520-0493(2002)130¡1913:EDAWPO¿2.0.CO;2
- Olson ecosystem types

9 Ecoregions in CarbonTracker

9.1 What are ecoregions?

Ecoregions are the actual scale on which CarbonTracker performs its optimization over land. Ecoregions are meant to represent large expanses of land within a given continent having similar ecosystem types, and are used to divide continent-scale regions into smaller domains for analysis. The ecosystem types use in CarbonTracker are derived from the Olson (1992) vegetation classification (Table 5, Figure 15).

We define an ecoregion as an ecosystem type within a given TransCom land region. There are 11 such TransCom land regions (Figure 16), so there are 11*19 = 209 possible ecoregions. However, not all ecosystem types are present in all TransCom regions, and the actual number of land ecoregions ends up being 126.

Note on "Semitundra": this is a potentially misleading shorthand abbreviation for a collection of ecosystems comprising semi-desert, shrubs, steppe, and polar+alpine tundra. The "Semitundra" zones appearing in northern Africa where one expects to find the Sahara desert are not, of course, tundra environments. They are instead semi-desert zones.

9.2 Why use ecoregions?

A fundamental challenge to atmospheric inversions like CarbonTracker is that there are not enough observations to directly constrain fluxes at all times and in all places. It is therefore necessary to find a way to reduce the number of unknowns being estimated. Strategies to reduce the number of unknowns in problems like this one generally impose information from external sources. In CarbonTracker, we reduce the problem

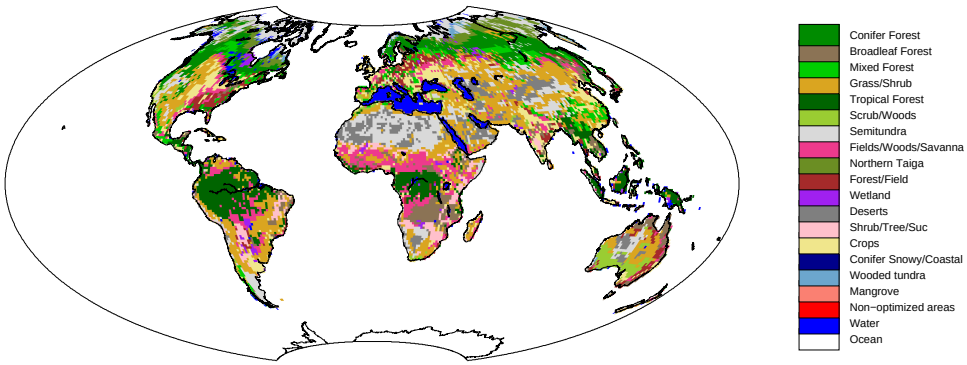

Figure 15: Global distribution of Olson ecosystem types.

Ecosystem Type	North American Boreal		North American Temperate	
	Area (km^2)	Percentage	Area (km^2)	Percentage
Conifer Forest	2315376	22.9%	1607291	14.0%
Broadleaf Forest	-	-	269838	2.4%
Mixed Forest	592291	5.9%	930813	8.1%
Grass/Shrub	53082	0.5%	2515582	21.9%
Tropical Forest	-	-	58401	0.5%
Scrub/Woods	-	-	416520	3.6%
Semitundra	3396292	33.6%	866468	7.6%
Fields/Woods/Savanna	29243	0.3%	1020939	8.9%
Northern Taiga	1658773	16.4%	-	-
Forest/Field	61882	0.6%	1243174	10.8%
Wetland	322485	3.2%	66968	0.6%
Deserts	-	-	21934	0.2%
Shrub/Tree/Suc	-	-	11339	0.1%
Crops	-	-	1969912	17.2%
Conifer Snowy/Coastal	41440	0.4%	73437	0.6%
Wooded tundra	360388	3.6%	6643	0.1%
Mangrove	-	-	-	-
Non-optimized areas	-	-	-	-
Water	1269485	12.6%	384728	3.4%
Total	10100736	100.0%	11463986	100.0%

Table 5: Ecosystem areas over the two TransCom regions covering North America.

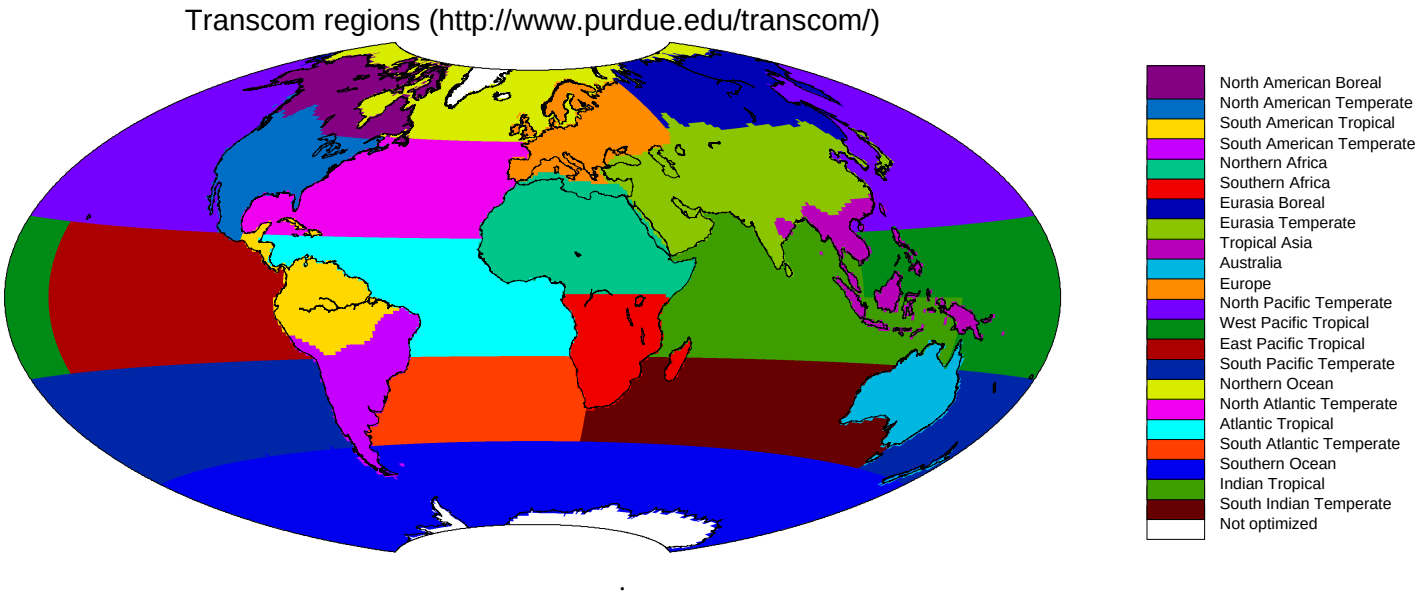

Figure 16: The 11 land regions and 11 ocean regions of the TransCom project

size both by estimating fluxes at the ecoregion scale, and by using a terrestrial biological model to give a first guess flux from the ecoregion. The model is also used to give the spatial and temporal distribution of CO_2 flux within a region and week.

9.3 Ecosystems within TransCom regions

Each TransCom land region (Figure 16) can contain up to 19 ecoregions.

9.4 References

- Olson ecosystem types

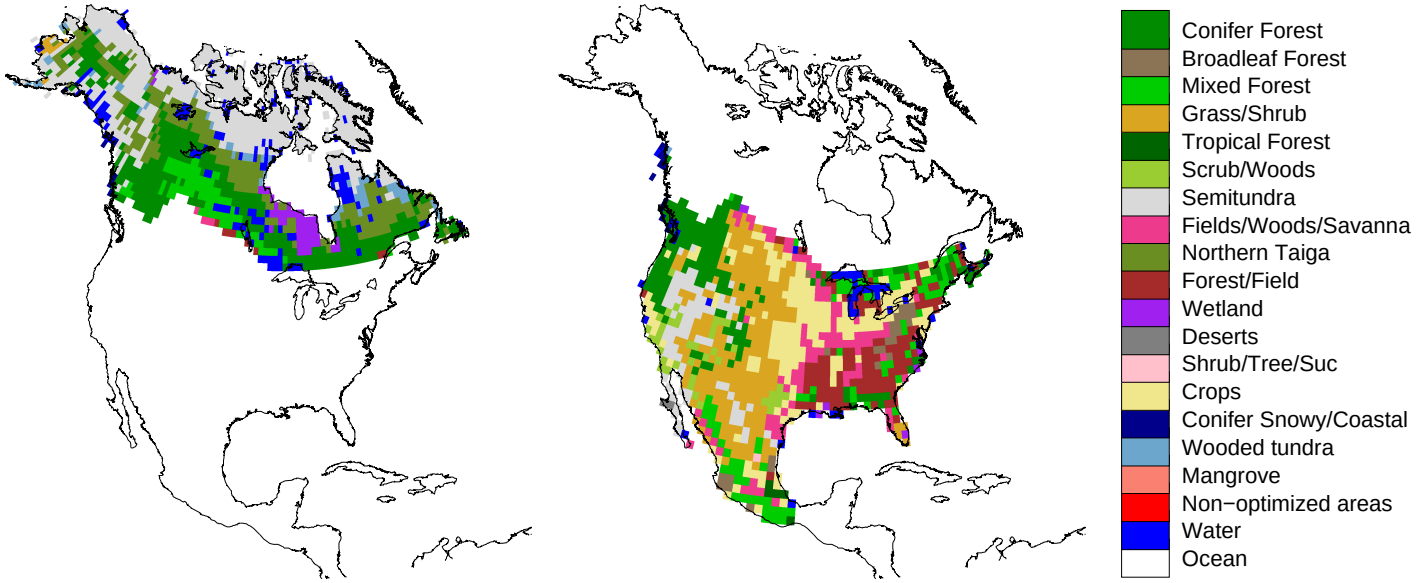

Figure 17: Ecoregions within the North American Boreal (left) and North American Temperate (right) TransCom regions.

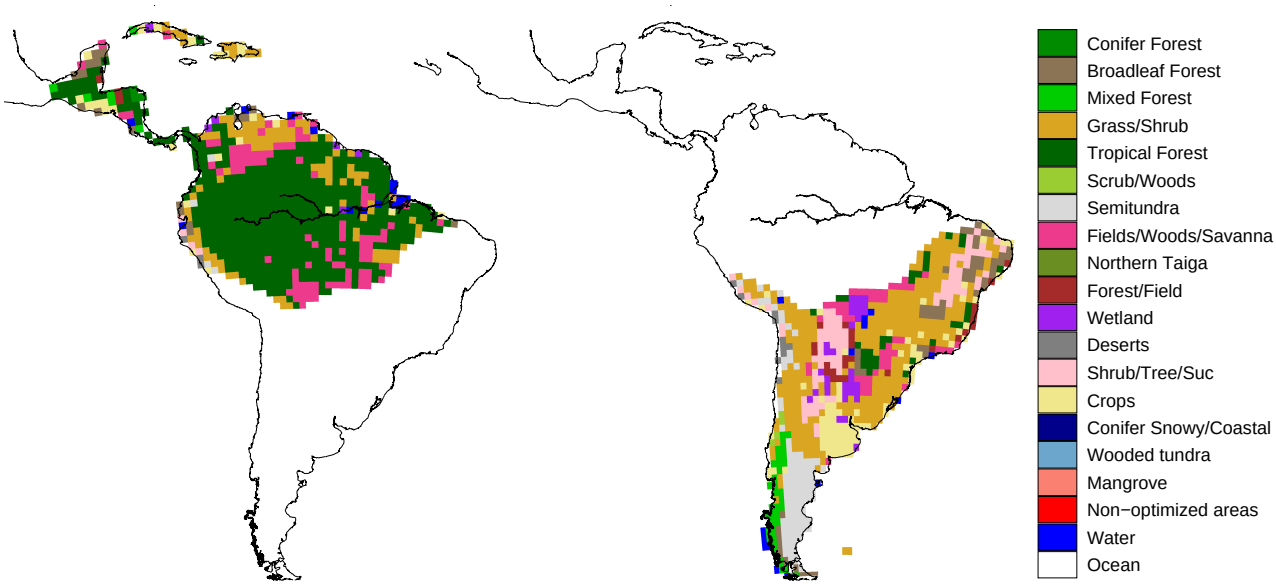

Figure 18: Ecoregions within the South American Tropical (left) and South American Temperate (right) TransCom regions.

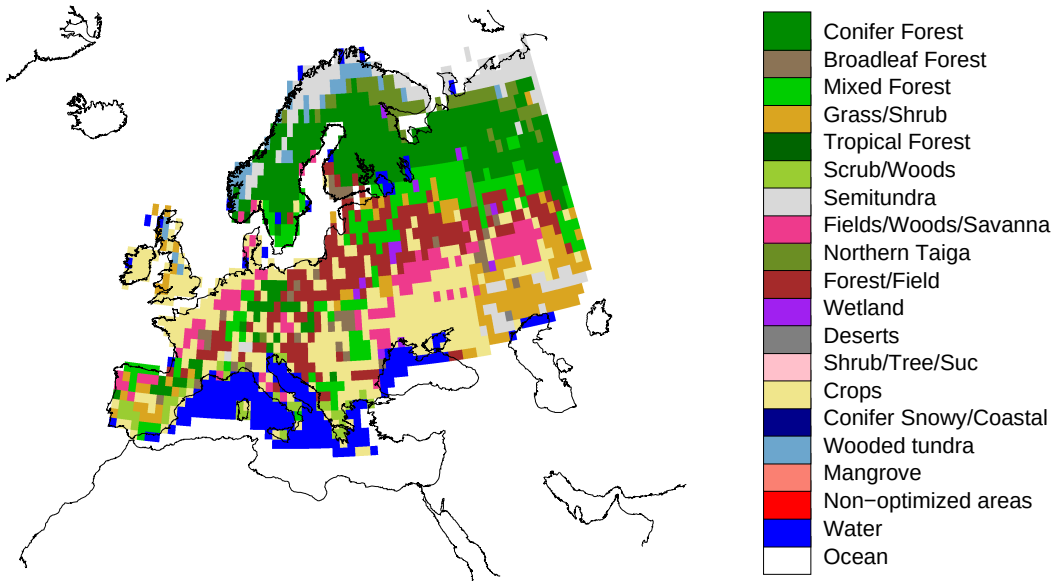

Figure 19: Ecoregions within the Europe TransCom region.

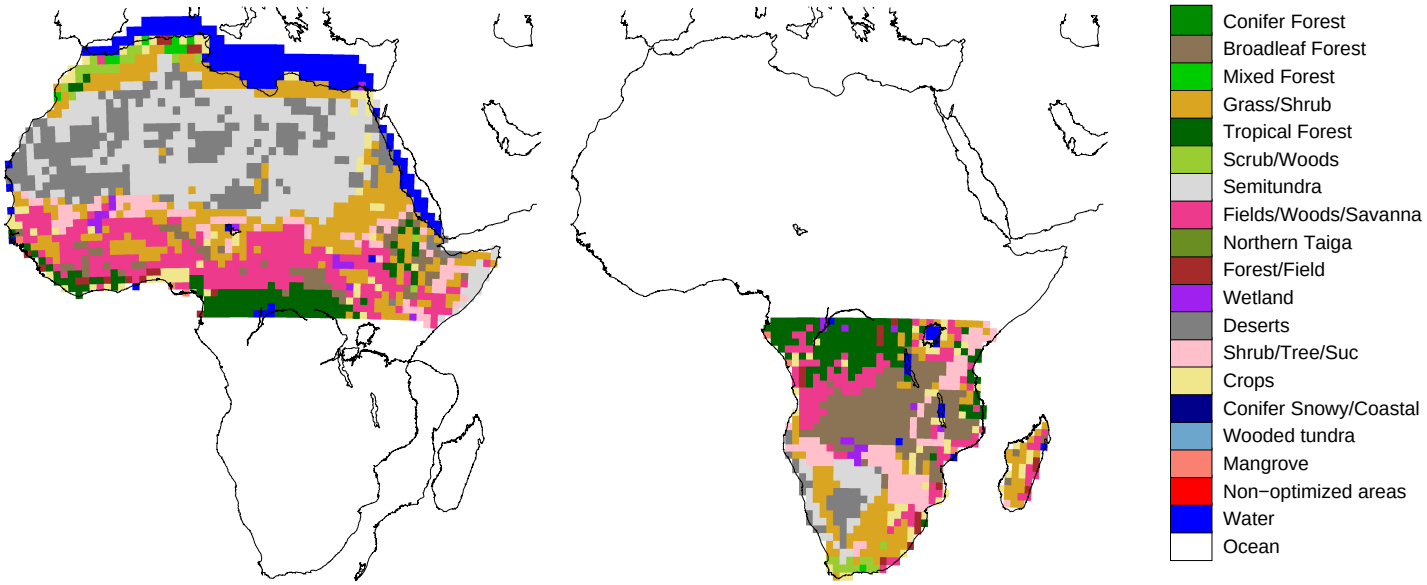

Figure 20: Ecoregions within the Northern Africa (left) and Southern Africa (right) TransCom regions.